First-Principles Calculations of the Thermodynamic, Structural, Electronic, and Optical Properties of Compositionally Disordered Semiconductor Materials

by

Logan Williams

A dissertation submitted in partial fulfillment
of the requirements for the degree of
Doctor of Philosophy
(Materials Science and Engineering)
in the University of Michigan
2019

Doctoral Committee:

Associate Professor Emmanouil Kioupakis, Chair
Professor Zetian Mi
Associate Professor Pierre Ferdinand P. Poudeu
Assistant Professor Liang Qi

Logan D. Williams

ldwillia@umich.edu

ORCID iD: 0000-0002-9062-8293

To Willow Wan

Acknowledgements

First and foremost, I would like to thank Manos Kioupakis for all of his amazing guidance as an advisor and mentor over the course of my PhD. Working for and learning from him has been a blessing.

I'd also like to thank all the wonderful people I have had the fortune to work alongside both in my group and as collaborators. You all made work much better through your good nature, cheer, and eagerness to help.

To my friends, thank you for staying in touch, even when life gets busy.

Finally, I am endlessly grateful to my parents, Doug and Laraine Williams, who have been the best parents I could have asked for.

Table of Contents

Dedication ii

Acknowledgements iii

List of Tables viii

List of Figures x

Abstract xxi

Chapter 1 Introduction 23

1.1 The many-body problem 23

1.1.1 Approximations for the nuclei 24

1.2 Solving the electronic many-body problem 25

1.3 Density Functional Theory (DFT) 25

1.3.1 The Hohenberg-Kohn theorem 25

1.3.2 The Kohn-Sham equation 26

1.3.3 The Local Density Approximation (LDA) 27

1.3.4 The Generalized Gradient Approximation (GGA) 29

1.3.5 The band gap problem 29

1.3.6 Hartree-Fock and hybrid Functionals 30

1.4 Modeling Alloys 32

1.4.1 Random Supercells 33

1.4.2 Virtual Crystal Approximation (VCA) & Coherent Potential Approximation (CPA) 33

1.4.3 Special Quasi-Random Structures 34

1.4.4 Small Sets of Ordered Structures (SSOS) 35

1.4.5 Cluster Expansion 36

Chapter 2 Electronic Properties of $Li_7La_3Zr_2O_{12}$ (LLZO) 38

2.1 Introduction 38
2.2 Methodology 40
2.3 Results and Discussion 41
2.4 Supplemental Information 48
2.5 Additional Work 51
Chapter 3 Defect Mediated Magnetic Coupling in $FeSb_2Se_4$ 53
3.1 Introduction 53
3.2 Methodology 55
3.3 Results and Discussion 55
Chapter 4 Electronic Properties of Cu_4TiSe_4 58
4.1 Introduction 58
4.2 Methodology 59
4.2.1 Electronic Band Structure and Optical absorption calculations 59
4.2.2 Ellipsometry Measurement of Reflective Index (n) and Extinction Coefficient (k) 60
4.2.3 Determination of absorption coefficient and optical band gap 61
4.2.4 Estimated Photovoltaic conversion efficiency (EPCE) 61
4.2.5 Electronic Transport Measurement 62
4.3 Results and Discussion 63
4.3.1 Structure 63
4.3.2 Electronic Structure 65
4.3.3 Optical and electronic properties 66
4.4 Concluding Remarks 70
4.5 Author Contributions 71
4.6 Acknowledgements 71
4.7 Additional Tables and Figures 72
4.8 Additional work after the paper 76
4.8.1 Seebeck Coefficient 76
4.8.2 Spectroscopic Limited Maximum Efficiency 78
4.8.3 Properties of the cubic and tetragonal phases of Cu_4TiSe_4 and Cu_4TiS_4 80
Chapter 5 Electronic Properties of $SrHfSe_3$ 82
5.1 Introduction 82
5.2 Methodology 83

5.2.1 First-Principles Calculations 83
5.2.2 Optical Band Gap Measurements 83
5.3 Results and Discussion 84
Chapter 6 System Energy Modeling of (Ge, Sn, Pb)(S, Se, Te) 89
6.1 Introduction 89
6.2 Results and Discussion 90
Chapter 7 Compositional-Structural relationships in (MgCoNiCuZn)O alloys 93
7.1 Introduction 93
7.2 Tuning of Structural Disorder 95
7.3 Conclusion 99
Chapter 8 Wurtzite $(B_2In_3)_xGa_{1-x}N$ alloys 100
8.1 Introduction 100
8.2 Methodology 103
8.3 Results and Discussion 104
8.4 Summary 111
8.5 Acknowledgements 111
8.6 Supplemental Information 112
Chapter 9 $B_xIn_yGa_{1-x-y}N$ in the Wurtzite and Zincblende phases 114
9.1 Introduction 114
9.2 Methodology 116
9.3 Results 118
9.3.1 Thermodynamic Properties 118
9.3.2 Structural Parameters 121
9.3.3 Band Gaps 123
9.3.4 Lattice-Matched Compositions 125
9.3.5 Discussion 127
9.4 Conclusion 128
9.5 Acknowledgements 129
Chapter 10 Properties of BAlGaN Alloys Lattice-Matched to AlN 130
10.1 Introduction 130
10.2 Methodology 132

10.3 Results and Discussion 133
10.3.1 Thermodynamics 133
10.3.2 Band Gap 135
10.3.3 Lattice Parameters 136
10.3.4 Light polarization and u Parameter 137
10.3.5 Piezoelectric Coefficients and Spontaneous Polarization Constants 141
Chapter 11 Machine Learning using Local Descriptors for Scintillator Prediction 143
11.1 Introduction 143
11.2 Methodology 146
11.3 Results and Discussion 147
11.4 Conclusions and Future Work 150
11.5 Acknowledgements 150
Bibliography 151

List of Tables

Table 2.1. Band Gap, Electronic Conductivity, and Peak Potential for LLZO as a Function of Composition[a] 43

Table 3.1. Energy of different magnetic configurations of $FeSb_2Se_4$, under the assumption of ferromagnetic alignment within the Fe atom chains and unity occupation of the sites by their most common occupant. Antiferromagnetic arrangements of the chains are the most energetically favorable. The configurations correspond to the atoms labeling scheme shown in Figure 3.2. 56

Table 3.2. Energy of different magnetic configurations of $FeSb_2Se_4$, under the assumption of ferromagnetic alignment within the Fe atom chains and unity occupation of the sites by their most common occupant, except for the inclusion of one Fe_{Sb} antisite defect, as shown in Figure 3.3. The Fe_{Sb} defect stabilizes partially ferromagnetic arrangements of the Fe chains in the structure. 57

Table 4.1. Selected crystallographic data for Cu_4TiSe_4 at 300K. 72

Table 4.2. Atomic coordinates, Wyckoff positions (W. P.), site occupancy factors, and equivalent isotropic displacement parameters (U_{eq} in $Å^2$) for all atoms in Cu_4TiSe_4. 73

Table 4.3. Selected inter-atomic distances (Å) in Cu_4TiSe_4. 73

Table 4.4. Indirect band gaps, direct band gaps, and formation energy differences for the cubic and tetragonal phases of Cu_4TiSe_4 and Cu_4TiS_4 using the HSE06 functional. Calculations used a 4 x 4 x 4 gamma-centered k-points grid for the cubic phases and a 4 x 4 x 2 gamma-

centered k-points grid for the tetragonal phases. In both compounds, the tetragonal phase is predicted to be thermodynamically more stable. 81

Table 6.1. Enthalpy of mixing for each ternary in the (Ge, Sn, Pb)(S, Se, Te) system calculated using either the lowest energy structures for each composition or only the rocksalt structures. The largest enthalpies of mixing exist when mixing Te and S in the same compound. 91

Table 9.1. Fitting parameters for the enthalpy of mixing, band gap, and lattice constant of wurtzite BInGaN alloys as a function of composition. 126

Table 9.2. Fitting parameters for the enthalpy of mixing, band gap, and lattice constant of zincblende BInGaN alloys as a function of composition 126

Table 10.1. u parameter and the energy difference between the heavy hole (HH) and crystal field split-off (CH) band energies at the Γ point for the group III nitrides. 137

Table 10.2. Spontaneous polarization (P_S), and piezoelectric coefficients for AlN, GaN, and BN calculated in this work using PBE with vdW relaxed structures and the hexagonal reference structure. Compared to previous literature values by Cyrus Dreyer's 2014 paper on BN[193], with sign error on P_S corrected, and Dreyer's 2016 paper on GaN and AlN.[194] Close agreement is achieved for the spontaneous polarization values, and rough agreement for the piezoelectric coefficients. Values predicted are smaller for GaN and larger for BN than those predicted by Dreyer. Note: the shown piezoelectric constants are the "proper" constants. 142

Table 10.3. Spontaneous polarization (P_S), and piezoelectric coefficients for BAlGaN alloys. 142

List of Figures

Figure 1.1. Comparison of the calculated formation energies using SSOSs and SQSs both without (left) and with (right) atomic relaxation. Adapted from the original paper.[19] 36

Figure 2.1. Tauc plot of the optical absorption measurement for Al-doped LLZP with an optical band gap of 5.46 eV indicated by the intercept of the two fitted lines 42

Figure 2.2. (a) Ionic transference number determined from DC galvanostatic polarization and EIS measurements. (b) Calculated partial density of states for the Ta = 0.75 LLZO composition, illustrating the orbital character of the band edges. The PDOS is scaled to match the band edge positions calculated used HSE+G_0W_0. The abscissa in both panels is aligned to facilitate comparisons between the transference number and the DOS. 45

Figure 2.3. Partial density of states for the Ta = 0.5 LLZO composition. 49

Figure 2.4. Partial density of states for the Ta = 0.75 LLZO composition. 49

Figure 2.5. Partial density of states for the Ta = 1.5 LLZO composition. 50

Figure 2.6. Partial density of states for the Al = 0.25 LLZO composition. 50

Figure 2.7. Band structure of the bottom three conduction bands and top 7 valence bands of $Li_{6.5}La_3Ta_{0.5}Zr_{1.5}O_{12}$ as calculated by PBE. The gap is indirect by ~5meV. 51

Figure 2.8. Charge density iso-surface of the valence band edge of $Li_{6.5}La_3Ta_{0.5}Zr_{1.5}O_{12}$. Charge (displayed in yellow) is in the shape of O 2p orbitals. 52

Figure 2.9. Charge density iso-surface of the conduction band edge of $Li_{6.5}La_3Ta_{0.5}Zr_{1.5}O_{12}$. Charge (displayed in yellow) is primarily located at the overlap of La 5d orbitals between neighboring La atoms. 52

Figure 3.1. Structures of $FeBi_2Se_4$ and $FeSb_2Se_4$ showing the partial occupancy of sites in the structure..... 55

Figure 3.2. Schematic representation showing the $FeSb_2Se_4$ unit cell with only the Fe atoms shown. The labels correspond to the ordering of the configuration labels in Table 3.1..... 56

Figure 3.3. Schematic representation showing the $FeSb_2Se_4$ unit cell including one Fe_{Sb} antisite defect with only the Fe atoms shown. The labels correspond to the ordering of the configuration labels in Table 3.2. The antisite defect causes ferromagnetic coupling of the two chains located above it in the z direction. 57

Figure 4.1. Crystal structure of CTSe project along [001]. (a) A ball-and-stick representation showing the 3D connectivity between metal tetrahedra, MSe_4; (b) an alternate polyhedral representation highlighting octahedral building blocks of $[Cu_4Se_4]^{4-}$ anionic clusters. The $[Cu_4Se_4]^{4-}$ anionic clusters form two interpenetrated face centered cubic (fcc) lattices (yellow and purple denote the two sublattices) to generate a 3D structure that is topologically similar to a double perovskite, with Ti^{4+} ions located at tetrahedral sites within the channels; (c) $[Cu_4Se_4]^{4-}$ anionic clusters consisting of a Cu-centered hexanuclear octahedral $[Cu]_6$ cluster capped by Se atoms on four of the eight triangular faces; (d) $TiSe_4$ tetrahedron shares only corners with $Cu(1)Se_4$ tetrahedra; (e) environment of Cu(1) and Cu(2) and their connectivity within the $[Cu_4Se_4]^{4-}$ anionic cluster. $Cu(2)Se_4$ tetrahedron share all edges with $Cu(1)Se_4$ tetrahedra, $Cu(1)Se_4$ tetrahedra exclusively share corners with

each other and $Cu(2)Se_4$ tetrahedra are isolated from each other; (f) $TiSe_4$ tetrahedron shares only corners with $Cu(2)Se_4$ tetrahedra and $TiSe_4$ tetrahedra are isolated from each other... 64

Figure 4.2. Electronic band structure of CTSe. (a) Calculated band structure highlighting the relatively flat valence (VB) and conduction (CB) bands, and the presence of both indirect (1.22 eV) and direct (1.46 eV) band gaps with similar values. (b) Projected density of states (DOS) highlighting the major orbital contributions; (c) band alignment of CTSe relative to vacuum and other photovoltaic materials. 65

Figure 4.3. Theoretical and experimental absorption coefficients of CTSe compared to leading solar absorber materials such as CdTe,[105] GaAs,[106] CIGS,[107] and CZTS,[108] and $CH_3NH_3PbI_3$.[109] CTSe outperforms all established solar-absorber materials in the 1.1–2.8 eV range. 66

Figure 4.4. Estimated photovoltaic conversion efficiency (EPCE) as a function of thickness for CTSe compared to CdTe[105] and GaAs.[106] CTSe reaches an efficiency of 30% for a thickness of 200 nm, approximately one order of magnitude thinner than typical CdTe or GaAs devices (1.5–5 mm)..... 70

Figure 4.5. Index of refraction (n) and the extinction coefficient (k) as a function of wavelength extracted from ellipsometry data. 74

Figure 4.6. Tauc analysis for the determination of optical band gap. a) allowed indirect transition and b) allowed direct transition..... 74

Figure 4.7. (a) Diffuse reflectance data on bulk CTSe powder. (b) Tauc fitting for allowed direct transition using diffuse reflectance data indicating an optical band gap of ~1.31 eV. 75

Figure 4.8. Urbach tail analysis of the optical absorbance of CTSe. The Urbach energy is calculated using the empirical formula $\ln\alpha = \ln\alpha o + (h\nu/E\_U)$ and fitting the linear region of

lnα vs hv. Urbach absorption tails typically arise from thermal fluctuation at the band edges or the presence of defects. Three linear regions are present giving Urbach energy (E_U) of 135 meV, 297 meV, and 429 meV within CTSe band gap. The large values obtained for the Urbach energy point to large concentrations of defects existing within the band gap. 75

Figure 4.9. Temperature dependence of the thermopower (S) and electrical conductivity (s) of CTSe. The positive values of the thermopower indicate holes as the majority carriers and the gradual increase of the electrical conductivity with rising temperature is consistent with the intrinsic semiconducting behavior of the compound. 76

Figure 4.10. Fitting of the electrical conductivity of CTSe using Arrhenius equation for thermal activation conductivity, Ln (σ) = Ln (σ_0) – Ea/KT. (a) low temperature transition (400 to 600 K) with activation energy of ~140 meV; (b) high temperature transition (700 to 800 K) with activation energy of ~296 meV. 76

Figure 4.11. Calculated Seebeck coefficient for p-type Cu_4TiSe_4 as a function of carrier concentration and temperature. 77

Figure 4.12. Seebeck coefficient for CTSe as calculated using p = $1x10^{21}$ cm^{-3} and from two experimental samples, showing rough agreement in order of magnitude. 78

Figure 4.13. Spectroscopic Limited Maximum Efficiency (SLME) for CTSe, GaAs, CdTe, and CZTS as function of thickness. CTSe is predicted to have poorer photovoltaic performance at large thickness due to losses attributable to its indirect band gap, but higher photovoltaic efficiency at low thickness due to its superior absorption properties. 80

Figure 5.1. Band structure of $SrHfSe_3$ calculated using the HSE06 functional. Energies are referenced to the valence band maximum. The compound is a direct gap material with a calculated gap of 0.88 eV..... 85

Figure 5.2. Optical band gaps of $Sr_{1-x}Sb_xHfSe_3$ showing increasing band gap with increasing Sb content. 86

Figure 5.3. Calculated partial density of states (PDOS) of $SrHfSe_3$. The valence band has primarily Se-p character, and the conduction band has primarily Hf-d character. 88

Figure 6.1. Predicted enthalpy of mixing using the model built with ternary enthalpies of mixing vs. as predicted using direct calculation of an SQS. Data shown is for using the lowest energy structure for each ternaries. The ternary mixing model is highly inaccurate. 91

Figure 7.1. Control of structural disorder through stereochemical frustration. a) $2\theta - \omega$ XRD spectra of Cu and Co variant ESO thin films. Only the 002 and 004 peaks from the ESO film are present, showing phase purity and epitaxy. * indicates MgO 002 and 004 substrate peaks. b) Out-of-plane lattice constants of the Cu variant and Co variant ESO films determined using Cohen's method. c) Reciprocal space map of equimolar, X = 0.20, ESO, showing the film is clamped to the substrate in the Q_X direction (in-plane). d) Normalized peak intensities of the ESO 002 and 004 peaks, showing a decrease in the peak intensity with increasing Cu. e) Full-width at half-max ($\Delta\theta$) of the 002 peaks in a), deconvolved with peak position, showing a significant increase in the peak width with increasing Cu concentration and a small decrease with Co composition. 95

Figure 7.2. Simulated bond length disorder in compositionally variant ESOs. a) 94-atom supercell of Cu-rich ESO relaxed using DFT. Ideal planes of atoms are overlain in red, highlighting the structural distortions (emphasized by arrows) most clearly on the oxygen anion sites (shown in grey). The Cu cations are shown in orange. b) Histograms of bond lengths on the Cu-cation sites for $X_{Cu, Co} = 0.11, 0.20, 0.33$ ESOs, demonstrating the characteristic double peak of a Jahn-Teller distorted cation. c) Axial bond length of the Cu

site in Cu variant (Cu) and Co variant (Co) ESO. As the concentration of Cu is increased in the material, we observe an increase in the length of the z (extended)-axis on the Cu cation site, implying that the degree of distortion is sensitive to the local environment about the Cu site and the total concentration of Cu. 97

Figure 7.3. Bond angle disorder in compositionally variant thin film ESOs. a) Histogram of cation-anion-cation bond angles for Cu variant ESO calculated from DFT. b) Variance (σ^2) of the Gaussian fits to the data in a). As the concentration of Cu cations is increased, the variance of the calculated bond angle changes significantly. 99

Figure 8.1. Band gaps vs. in-plane lattice constant (a) for wurtzite group-III nitrides. The $B_xIn_{1.5x}Ga_{1-2.5x}N$ alloys investigated in this work (red diamonds) maintain approximate lattice match to GaN while their gaps span the entire visible range. The error bars show the uncertainty in the lattice constant (See Figure 8.3). Closed circles and full lines represent the direct gap materials. Open circles and dashed lines represent the indirect gap materials. . 102

Figure 8.2. Calculated transition temperature for the thermodynamic equilibrium random mixing of group III nitride alloys. (a) $B_xIn_{1.5x}Ga_{1-2.5x}N$ and $B_xGa_{1-x}N$ as a function of Boron mole fraction. (b) $In_{1.5x}Ga_{1-1.5x}N$ as a function of Indium mole fraction. The transition temperatures of $B_xIn_{1.5x}Ga_{1-2.5x}N$ are approximately 2/3 that of $B_xGa_{1-x}N$ of equal B mole fraction at low boron concentrations (<0.2), indicating that boron is more easily incorporated into InGaN than into GaN..... 106

Figure 8.3. The calculated lattice constants of InGaN and BInGaN alloys relative to GaN along (a) the a direction and (b) the c direction. Both the values for each configuration (crosses) and the configurational average (squares) are displayed. The *a* lattice constant data are fit to a bowing equation and have a bowing parameter of 0.052. The error bars show the

statistical uncertainty for each configurational average, calculated as half of the range divided by the square root of the number of samples. The mismatch of $B_xIn_{1.5x}Ga_{1-2.5x}N$ to GaN along the *a* axis is significantly reduced compared to an equivalent $In_{1.5x}Ga_{1-1.5x}N$ alloy, especially at lower boron and indium concentrations, while BInGaN is approximately lattice matched to GaN along the *c* direction. 107

Figure 8.4. The calculated band gaps of $B_xIn_{1.5x}Ga_{1-2.5x}N$, $In_{1.5x}Ga_{1-1.5x}N$, and $B_xGa_{1-x}N$ as a function of mole fraction x. The calculated gap values have been increased by 0.25 eV to match the experimental gap of GaN at room temperature (3.39 eV).[169] The band gap of BInGaN alloys spans the entire visible range. The gap of BInGaN has approximately the same value as an InGaN alloy of the same indium mole fraction, indicating that boron incorporation has a negligible effect on the gap of InGaN. Figure 8.7 shows the variability in the DFT band gap for all simulation cells used in the structural calculations. 108

Figure 8.5. Projected Density of States (pDOS) for a $B_{10}In_{15}Ga_{11}N_{36}$ solid solution. Similar to InGaN, the conduction-band edge is primarily composed of In and N states. The valence band displays a localized band of N 2p character caused by local planarization of B-N bonds near boron atoms. The electron density of the localized state and the planarized B atoms are visualized in the inset. The pDOS calculated with HSE06 and optB86b-vdW is qualitatively similar, the only major quantitative difference being the band-gap value (Fig. 8.8) 109

Figure 8.6. Hole localization energy for $B_xIn_{1.5x}Ga_{1-2.5x}N$ calculated using HSE06. No localized states are seen at boron mole factions less than ~0.1. The hole localization energy is maximum near the $B_{0.278}In_{0.417}Ga_{0.306}N$ composition. 110

Figure 8.7. Band gap of $B_xIn_{1.5x}Ga_{1-2.5x}N$ vs. boron mole fraction calculated with the optB86b-vdW functional for all cells used in the structural-analysis calculations. The band gap for each configuration is shown using black circles, while the red crosses denote the cells that most closely match the random pair-correlation functions at each composition that were subsequently used for the HSE06 electronic-structure calculations (Figures 8.4 and 8.6). 112

Figure 8.8. Partial Density of States (pDOS) of a $B_{10}In_{15}Ga_{11}N_{36}$ solid solution calculated (a) with the optB86b-vdW functional and (b) with the HSE06 functional, using a 2x2x2 Γ-centered Brillouin-zone sampling grid. Energies are referenced with respect to the highest occupied valence band state. Both functionals display qualitatively similar pDOS, with the only significant quantitative difference being the increased value of the band gap with HSE. The gap observed in the conduction band is an artifact caused by under-sampling of the Brillouin zone. For this reason, the optB86b-vdW functional with a rigid shift applied to correct for the band-gap underestimation was used to converge the pDOS in Figure 5 as a function of Brillouin-zone sampling (with an 8x8x8 Γ-centered grid). The hole localization energy with optB86b-vdW is 0.354 eV, while HSE with a 25% Hartree-Fock mixing parameter increases the localization energy by ~15% to 0.407 eV. Using a mixing parameter of 29.63%, which causes the calculated band gap of GaN to match experiment, has a negligible effect (~4 meV change) on the localization energy. 113

Figure 9.1. Thermodynamics of (a, b) wurtzite and (c, d) zincblende $B_yIn_xGa_{1-x-y}N$ alloys. (a, c) Calculated enthalpy of mixing per cation and (b, d) phase-transition temperature as functions of composition. The enthalpy of mixing and the phase transition temperature increase as the boron mole fraction increases. 119

Figure 9.2. Relative thermodynamic stability of wurtzite and zincblende $B_yIn_xGa_{1-x-y}N$ alloys. The wurtzite phase is more stable at compositions closer to InGaN, and the zincblende phase is more stable at compositions closer to BGaN. 120

Figure 9.3. Relative difference of wurtzite $B_yIn_xGa_{1-x-y}N$ calculated lattice constants with that of GaN as a function of composition along the (a) *a* and (b) *c* directions. The solid black lines indicate an exact lattice match with GaN along each direction. The lattice-match line in (a) corresponds to Eqn. 9.5, and that in (b) corresponds to Eqn. 9.6. A ratio of approximately 2 B to 3 In provides a lattice match to GaN in the *a* direction for up to ~5% B composition. 122

Figure 9.4. Relative difference of zincblende $B_yIn_xGa_{1-x-y}N$ calculated lattice constant with that of GaN as a function of composition. The solid black line indicates an exact lattice match with GaN and corresponds to Eqn. 9.7. 122

Figure 9.5. Calculated band gap of wurtzite $B_yIn_xGa_{1-x-y}N$ as a function of boron and indium mole fractions, depicted by the corresponding color on the visible light spectrum. The gap values calculated with HSE06 have been rigidly increased by 0.25 eV to match the experimental gap of wurtzite GaN at room temperature (3.39 eV).[169] 124

Figure 9.6. Calculated band gap of zincblende $B_yIn_xGa_{1-x-y}N$ as a function of boron and indium mole fractions, depicted by the corresponding color on the visible light spectrum. The gap values calculated with HSE06 have been rigidly increased by 0.31 eV to match the experimental gap of zincblende GaN at room temperature (3.24 eV).[177,178] 125

Figure 9.7. Calculated values for (a) phase-transition temperature, (b) enthalpy of mixing per cation, (c) boron mole fraction, and (d) band gap for wurtzite $B_{y(x)}In_xGa_{1-x-y(x)}N$ compositions exactly lattice matched to GaN along the *a* direction. As in Figure 6, the

HSE06 calculated gap values have been rigidly increased by 0.25 eV to match the experimental gap of GaN at room temperature (3.39 eV).[169] The lattice-matched curve in (b) is represented by Eqn. 9.5. 127

Figure 10.1. Transition temperature for thermodynamic stability between the alloy and the linear combination of group III nitride binaries as a function of boron fraction x for $B_xAl_{1-9x}Ga_{8x}N$, $B_xAl_{1-10x}Ga_{9x}N$, $B_xAl_{1-x}N$, and $B_xGa_{1-x}N$. 134

Figure 10.2. The enthalpy difference between ($B_xAl_{1-9x}Ga_{8x}N$, $B_xAl_{1-10x}Ga_{9x}N$) and the sum of the enthalpy for the equivalent $B_xAl_{1-x}N$ and $Al_{1-y}Ga_yN$ alloys. 135

Figure 10.3. Band gap as calculated with HSE06 for $Al_{1-x}Ga_xN$, $B_{0.1x}Al_{1-1.1x}Ga_xN$, and $B_{0.11x}Al_{1-1.11x}Ga_xN$ as a function of gallium fraction x. 136

Figure 10.4. Ratio of the alloy lattice constant to AlN's lattice constant for the in-plane *a* (left) and out-of-plane *c* (right) directions for $B_{0.1x}Al_{1-1.1x}Ga_xN$ (blue) and $B_{0.11x}Al_{1-1.11x}Ga_xN$ (red) as a function of gallium fraction x. Grey line shows the values for $Al_xGa_{1-x}N$ alloys for comparison. The *a* lattice parameter is reduced more by the substitution of aluminum for boron than the *c* lattice parameter is. 137

Figure 10.5. Structural u parameter as a function of the gallium fraction (x) for $Al_{1-x}Ga_xN$ alloys. The u parameter displays a bowing relationship with bowing parameter of b = 0.00299794. 138

Figure 10.6. u parameter vs aluminum content in $B_xAl_{1-x}N$. For low boron content, the u parameter roughly follows Vegard's law. 139

Figure 10.7. u parameter vs. the boron content (x) in $B_xGa_{1-x}N$ alloys. The data is very noisy at larger boron content, where the alloys are known to be experimentally unstable. The fit in this plot corresponds to b = 0.00590904. 140

Figure 10.8. Structural u parameter as a function of the gallium fraction (x) for $Al_{1-x}Ga_xN$, $B_{0.11x}Al_{1-1.11x}Ga_xN$, and $B_{0.1x}Al_{1-1.1x}Ga_xN$ alloys. Boron addition reduces the u parameter compared to equal Ga content $Al_{1-x}Ga_xN$ alloys, which means that boron alloys with the same band gap will have lower u parameters. 141

Figure 11.1. Schematic depiction of the change in 4f-shell and 5d-shell electron binding energies in Ce^{3+} when going from vacuum to a host environment "A". There is a significant lowering of the lowest energy 5d state relative to the 4f state, as well as a splitting of the 5d energy levels due to local bonding environment. Reprinted from the original paper.[208] 145

Figure 11.2. Average RMSE of crystal field depression, D, for the training (gold bar) and test (striped grey bar) datasets using either the best two bulk crystal descriptors (PBE band gap and average electronegativity) or a local environment descriptor in addition to the two bulk descriptors. The best two performing descriptors are Gaussian Symmetry functions and AGNI fingerprints. 147

Figure 11.3. Average RMSE of crystal field depression, D, for the training (gold bar) and test (striped grey bar) datasets using the AGNI Fingerprints and Gaussian Symmetry functions restricted to different maximum distances from the doping site center. Both perform optimally at 3.75Å. 148

Figure 11.4. Average RMSE of crystal field depression, D, for the training (gold bar) and test (striped grey bar) datasets using the AGNI Fingerprints and Gaussian Symmetry functions with and without angular components included. 149

Abstract

Alloyed semiconductor systems can provide improved properties beyond their unalloyed counterparts. Atomistic modeling of such systems was previously infeasible, but increases in computational power and improvements in modeling methods for random alloys have opened up this field of study, as well as unalloyed systems with natural disorder.

Using these techniques, we analyze the structure-composition-property relationships in many technologically relevant alloyed and disordered semiconductor systems. First, we show the band gap insensitivity of the solid-state Li electrolyte LLZO to tantalum and aluminum doping. Next we show that antisite defects play a crucial role in ferromagnetic ordering within the high Tc ferromagnetic semiconductor FeSb2Se4. We then predict the large absorption coefficient and optimal band gap of Cu4TiSe4 for function as a thin film solar cell absorber material, but also its tendency to form copper-related defects that would hinder functionality as a photovoltaic. We analyze new inorganic compounds, SrHfSe3 and (Ge, Sn, Pb)(S, Se, Te). Finally, we explore boron incorporation in group-III nitrides. We show that the incorporation of boron into InGaN, the material that is the active layer in blue LEDs and won the 2014 Nobel prize in physics, can maintain the electronic properties of InGaN while better matching its structural properties to the surrounding GaN. This will allow for thicker active layers to be grown in devices, improving overall device efficiency and reducing device size. Additionally, BAlGaN alloys are shown to be easy to lattice match to AlN with band gaps similar to AlGaN alloys of the same gallium content, but with a smaller structural u parameter that correlates to a TE polarized light emission that is easier to extract from LEDs. Additionally, we analyze the polarization of BAlGaN alloys.

Lastly, we also use machine learning on combined experimental and computational data for exploring vast chemical spaces for potential scintillator host materials. By adding local structural information into a machine learning model, we show improved ability to predict doping Ce d energy levels inside various host materials.

Chapter 1 Introduction

Ab initio, or completely theory-based with no empirical terms, prediction of material properties is a highly difficult task that has nevertheless seen much advancement and produced many results in recent years. These first-principles methods offer direct access to quantities such as electronic wavefunctions, local atomic relaxations, spin-state configurations, and many others that are difficult to measure experimentally. The scope of these methods has been continuously growing in terms of accuracy, number of properties able to be calculated, and the size of the atomic systems able to be analyzed.

1.1 The many-body problem

The fundamental challenge in these first-principles methods is the quantum nature of interacting electrons and nuclei. An ideal description of a material would require solving the combined wave functions of all electrons and nuclei in a way that obeys the many-body Schrodinger equation.

$$\hat{\mathcal{H}}\Psi_M(\{\boldsymbol{R}\},\{\boldsymbol{r}\}) = \mathcal{E}_M\Psi_M(\{\boldsymbol{R}\},\{\boldsymbol{r}\}) \tag{1.1}$$

where

$$\begin{aligned}\hat{\mathcal{H}} = &-\sum_{I=1}^{P}\frac{\hbar^2}{2M_I}\nabla_I^2 - \sum_{i=1}^{N}\frac{\hbar^2}{2m_e}\nabla_i^2 + \frac{e^2}{2}\sum_{I=1}^{P}\sum_{J\neq I}^{P}\frac{Z_I Z_J}{|\boldsymbol{R}_I - \boldsymbol{R}_J|} \\ &+ \frac{e^2}{2}\sum_{i=1}^{N}\sum_{j\neq i}^{N}\frac{1}{|\boldsymbol{r}_i - \boldsymbol{r}_j|} - e^2\sum_{I=1}^{P}\sum_{i=1}^{N}\frac{Z_I}{|\boldsymbol{R}_I - \boldsymbol{r}_i|}\end{aligned} \tag{1.2}$$

is the Hamiltonian that describes the coupled system of P electrons and N nuclei of atomic number Z_I and mass M_I. As written, the coupling terms between the nuclei, the electrons, and the electrons and nuclei make this equation incredibly difficult to solve for any system with multiple atoms.

1.1.1 Approximations for the nuclei

Instead, many approximations have been developed that offer more solvable and resource-efficient methods to treat electrons and nuclei while still providing accurate solutions. The first major approximation is the adiabatic or Born-Oppenheimer approximation, which says that the motion of the electrons and nuclei can be decoupled due to the large difference in their velocities and masses ($m_e/m_{nucleus} \sim 10^{-3}$). Using this approximation, the motion of the electrons is always solved while the nuclei are frozen in place. The motion of the nuclei is then solved by assuming that the electrons are always in their ground state position for the current nuclear configuration.

The second approximation is treating the nuclei in a classical instead of quantum sense. Since the mass of nuclei is so much larger than the electron mass, they can accurately be represented as classical point particles instead of waves. Using these two approximations, the electrons are always assumed to be in their ground state and the motion of each nuclei is determined by the electronic ground state and the simple Newton's equation of motion.

With these approximations, the many-body interacting Hamiltonian has been reduced down to only the electronic system and can be written as

$$\hat{h}_e = -\frac{\hbar^2}{2m}\sum_{i=1}^{N}\nabla_i^2 - e^2\sum_{I=1}^{P}\sum_{i=1}^{N}\frac{Z_I}{|\boldsymbol{R}_I - \boldsymbol{r}_i|} + \frac{e^2}{2}\sum_{i=1}^{N}\sum_{j\neq i}^{N}\frac{1}{|\boldsymbol{r}_i - \boldsymbol{r}_j|} \tag{1.3}$$

where the atomic nuclei $\mathbf{R}_I$ are simple parameters and not dynamic variables.

1.2 Solving the electronic many-body problem

In the above expression, the first term is the electronic kinetic energy, the second term is the electron-nuclei interaction ($V_{n\text{-}e}$), and the third term is the electron-electron interaction ($V_{e\text{-}e}$). Unfortunately, solving this Hamiltonian exactly is still impossible due to the complex nature of the electron-electron interaction. Solving this problem is at the core of theoretical condensed-matter physics, and many approximations have been proposed to make the problem computationally tractable. This introduction will only include some of the more popular techniques that are relevant to the work in the following chapters. Both Density Functional Theory (DFT) and Hartree-Fock (HF) methods are based in recasting the many-body wavefunction into single-particle states. Hartree-Fock calculations are often combined with traditional DFT in what are referred to as hybrid functionals for DFT.

1.3 Density Functional Theory (DFT)

The most popular solution to the electronic many-body problem is currently Density Functional Theory (DFT), which balances an accurate solution with a reasonable computational cost. It avoids the exponential increase in computational cost with the number of electrons in the system that direct wave function calculation would entail by remapping the problem onto one of single particles related through an effective potential.

1.3.1 The Hohenberg-Kohn theorem

Density functional theory is based upon the Hohenberg-Kohn theorem formulated in 1964.[1] The first theorem establishes a one-to-one correspondence (except for a constant) between

the external potential and the ground-state electronic charge density of the system. Since the charge density determines the external potential and also the Hamiltonian, this allows for determination of all physical properties of the system as well. This theorem massively reduces the dimensionality of the problem from 3N variables for an N electron system down to 3 variables for the electron density.

The second theorem states that the ground state total energy can be written as a universal functional of the density for any external potential. This means that for any external potential, the ground state energy of the system can be minimized with respect to the density to obtain the ground state electronic density of the system.

1.3.2 The Kohn-Sham equation

The functional describing the interacting system is complex, and thus minimization to the ground state is usually performed using the Kohn-Sham scheme instead.[2] The Kohn-Sham scheme maps the many-body interacting system to a fictitious non-interacting system using a different external potential, the Kohn-Sham potential, which is created in such a way to ensure that the ground state charge density and chemical potentials are the same in both systems.

The Hamilton is now split into four terms: the kinetic energy and $V_{n\text{-}e}$ terms discussed above, and a $V_{e\text{-}e}$ now split into two terms. The first, V_H, is called the Hartree potential and is the self-interaction of a classical uniform negative charge density. It is formally written as

$$V_H(\vec{r}_e) = \int \frac{\rho(\vec{r})d\vec{r}}{4\pi\epsilon_0 |\vec{r}_e - \vec{r}|} \tag{1.4}$$

The second part of $V_{e\text{-}e}$ is the exchange-correlation potential V_{xc}. It contains all leftover potential energy from the actual interacting system of electrons. All the complicated interactions and

higher-order many body terms are contained within this term, and its exact form is not known but approximated (detailed in the next section).

With a reasonable approximation for V_{xc}, computational evaluation of the Kohn-Sham system is now possible through a straightforward iterative procedure. An initial electron density is selected, and the single-particle equations are solved through the Kohn-Sham Hamiltonian, yielding single-particle eigenvalues and eigenstates. These can then be used to reconstruct a new electron density of the system. If the difference between input and output is within some tolerance, the system is converged and the electron density of the system is now known, along with other physical properties. If outside the set tolerance, the output density is fed back into the start of the loop, used to evaluate the Hamiltonian and recomputed the density again until convergence is reached. Typically, the convergence criterion used in practice is based upon system total energy.

The eigenvalues and eigenstates solved for through the Kohn-Sham equation are not formally the same as the physical quasiparticle energies and wavefunctions, but have been shown to have very strong resemblance to the experimental ones with the exception of an underestimated band gap for insulators and semiconductors when using the common set of exchange-correlation functionals detailed in the next set.[3] Thus, in practice, the Kohn-Sham eigenstates can be identified as zero order approximations of the physical eigenstates of the system. The systematic underestimation of band gaps is referred to as the band gap problem as is discussed later.

1.3.3 The Local Density Approximation (LDA)

The first approximation for the exchange-correlation functional is the Local Density Approximation and was proposed by Kohn and Sham.[2] It is based upon a system where the V_{xc}

is known to a high degree of accuracy, a locally homogeneous electron gas. The exchange part of the exchange-correlation is given by the Slater expression[4] (in atomic units).

$$\epsilon_{\mathrm{x}}(n(\boldsymbol{r})) = -\frac{3}{4}\left(\frac{3}{\pi}\right)^{1/3}\rho^{1/3} = -\frac{0.458}{r_s} \tag{1.5}$$

The correlation part of the exchange-correlation can be obtained by parameterizing the results of Monte Carlo simulations of a homogeneous electron gas, as was done upon the Monte Carlo calculations of Ceperley and Alder[5] by Perdew and Zunger.[6] In atomic units:

$$\epsilon_{\mathrm{c}}(n(\boldsymbol{r})) = \begin{cases} 0.0311\ln r_s - 0.048 + 0.002 r_s \ln r_s - 0.0116 r_s, & r_s \leq 1 \\ -0.1423/(1 + 1.0529\sqrt{r_s} + 0.3334 r_s), & r_s > 1 \end{cases} \tag{1.6}$$

The LDA has since been generalized to systems with spin polarization and non-collinear spin. Despite the complete lack of nonlocal many-body effects in the LDA, the approximation gives generally good agreement with physical experiment. Lattice constants, bond lengths and bond angles typically within 1-2% of experiment and bulk moduli and vibrational frequencies within a few percent. It works best for *s* and *p* electron systems with strong chemical bonds.

However, LDA errs on the side of overestimating binding energies and underestimating bond lengths. Exponential decay in vacuum regions instead of the correct 1/r behavior causes poor molecular properties. It also is poor at representing systems with weak bonds such as van der Waals and hydrogen bonding or strongly localized electrons such as those occupying d and f orbitals. As was mentioned before, it also systemically underestimates the band gaps of semiconductors and insulators.

1.3.4 The Generalized Gradient Approximation (GGA)

The Generalized Gradient Approximation is a computationally cheap way to improve upon the LDA, adding a dependence upon the gradient and higher-order derivatives of the local density. The most popular version of GGA is known as PBE after its authors, Perdew, Burke, and Ernzerhof.[7] GGA functionals tend to be more accurate than LDA for predicting molecular properties. They err on the side of underestimating binding energies and overestimating bond lengths, opposite of LDA's trend. Like LDA, they are still poor for treating weak bonds and strongly localized electrons, and also suffer from the band gap problem.

1.3.5 The band gap problem

As was mentioned in the previous sections, the common implementations using only local density or local density and gradient information in the exchange-correlation functional pathologically fail at reproducing experimental band gaps of semiconductors and insulators.

A brief exercise can be used to help explain the origin of the band gap problem. Consider a semiconductor with N occupied valence bands, a direct band gap located at Γ, and assume each band holds one electron. DFT calculated band gaps using the eigenvalues from solving the Kohn-Sham equations, so the N^{th} eigenvalue corresponds to the valence band and the $(N+1)^{th}$ eigenvalue corresponds to the conduction band. The Kohn-Sham DFT band gap is thus defined as:

$$E_{gap}^{KS} = \epsilon_{N+1}^{KS}(N) - \epsilon_{N}^{KS}(N) \tag{1.7}$$

where the argument is the number of electrons present in the system and the subscript is the Kohn-Sham eigenvalue of the system. It is the difference between the highest occupied and lowest unoccupied states within the system. For molecules, these are referred to as the Highest Occupied Molecular Orbital (HOMO) and Lowest Unoccupied Molecular Orbital (LUMO). For

an extended solid, these are the Conduction Band Minimum (CBM) and Valence Band Maximum (VBM). However, the electronic band gap of the system is defined as:

$$E_{gap} = \epsilon_{N+1}^{KS}(N+1) - \epsilon_{N}^{KS}(N) \tag{1.8}$$

The difference between these can be easily seen by adding and subtracting $\epsilon_{N+1}^{KS}(N)$ and rearranging the terms as follows:

$$E_{gap} = \epsilon_{N+1}^{KS}(N+1) - \epsilon_{N}^{KS}(N) + \epsilon_{N+1}^{KS}(N) - \epsilon_{N+1}^{KS}(N)$$

$$E_{gap} = [\epsilon_{N+1}^{KS}(N) - \epsilon_{N}^{KS}(N)] + [\epsilon_{N+1}^{KS}(N+1) - \epsilon_{N+1}^{KS}(N)]$$

$$E_{gap} = E_{gap}^{KS} + \Delta_{xc} \tag{1.9}$$

From the form of Δ_{xc}, it can be seen to represent the shift to the CBM when an electron occupies it. The addition of a single electron to a system of infinite size, such as a periodic system, produces an infinitesimal change in the electron density. As the V_{xc} of both the LDA and GGA are parameterized from the homogeneous electron gas, they have a smooth variation for infinitesimal changes in the density, which equates to $\Delta_{xc} = 0$. The true exchange-correlation functional is known to have a derivative discontinuity for systems with a band gap[8,9], and thus neither LDA nor GGA can possibly correctly calculate electronic band gaps.

1.3.6 Hartree-Fock and hybrid Functionals

Hybrid functionals are a popular method currently for achieving more accurate DFT calculations at the cost of increased computational cost. They are able to either partially or fully correct the Kohn-Sham band gap, more accurately treat d and f electrons, and are better able to describe localized states. For many situations, they are often the best trade-off in cost and accuracy amongst current methods.

Hybrid functionals are a literal mixing of standard DFT (usually a GGA functional) with the Hartree-Fock method. The Hartree-Fock method is a different way of replacing the many-

body problem with a solvable approximation. Hartree originally expressed the many-body wavefunction as a product of single-particle states, known as orbitals, which described both the positions and the spin degrees of freedom. Fock later amended the method to enforce antisymmetry of the wavefunction by constructing the product via a Slater determinant.[10] Within this framework, the single particle Hamiltonian is the same as DFT, except the exchange-correlation potential has been replaced by the Hartree-Fock exact exchange, which has the form:

$$V_{\mathrm{x}}^{\mathrm{HF}}(\vec{r}_e) = -\int \frac{\rho_{\mathrm{x}}(\vec{r}_e, \vec{r})d\vec{r}}{4\pi\epsilon_0 \left|\vec{r}_e - \vec{r}\right|} \tag{1.10}$$

where the exchange density is defined as:

$$\rho_{\mathrm{x}}(\vec{r}_e, \vec{r}) = \sum_{j \neq i} \frac{\psi_i(\vec{r})\psi_i^*(\vec{r}_e)\psi_j(\vec{r}_e)\psi_j^*(\vec{r})}{\psi_i(\vec{r}_e)\psi_i^*(\vec{r}_e)} \tag{1.11}$$

V_x^{HF} describes the effects of exchange between electrons. Hartree-Fock does not include the effects of screening in the system, which is an important cancellation term that should appear in the correlation energy. Thus, Hartree-Fock alone is only well suited to isolated atoms and other systems where screening is not important. The integral form of V_x^{HF} makes Hartree-Fock calculations significantly more expensive than DFT calculations.

A hybrid functional for DFT simply uses a fraction of Hartree-Fock exact exchange in replacement of some of the exchange from the base DFT functional. For example, the single particle Hamiltonian for a hybrid functional would have this general form:

$$H = \frac{-\hbar^2}{2m_{\mathrm{e}}}\nabla_{\mathrm{e}}^2 + V_{n-e} + V_H + V_{\mathrm{xc}} + \alpha\{V_{\mathrm{x}}^{\mathrm{HF}} - V_{\mathrm{x}}^{\mathrm{DFT}}\} \tag{1.12}$$

where the first term is the electron kinetic energy, the second term is effective potential from the nuclei-electron interactions, the third term is the Hartree potential, the fourth term is the

exchange-correlation term from DFT, and the last term replaces a fraction of the DFT exchange with Hartree-Fock exact exchange, where α controls the fraction chosen. As α is a free parameter, DFT calculations with hybrid functionals are semi-empirical instead of truly from first principles. A value of 0.25 for α has been shown to give reasonable performance for many semiconductor systems, although larger values are typically needed to correctly predict the experimental band gap for wide gap materials.

There are many possible varieties of hybrid functionals, but the two most popular by far are PBE0[11–13] and HSE.[14–16] Both methods use the GGA method of Perdew, Burke, and Ernzerhof[7] for the DFT portion of the functional, and both typically replace 25% of the DFT exchange with Hartree-Fock exact exchange. However, HSE truncates the contributions to exact exchange beyond a set length, typically 0.2 Å for the most popular HSE06 formalism. This effective screening length for the Hartree-Fock exchange typically gives improved bulk properties as well as significantly reducing the computational overhead for large systems.

1.4 Modeling Alloys

DFT has historically been most useful and most used to evaluate the properties of systems with small numbers of atoms (~10s). Pure, periodic crystals without defects can typically be represented by a handful of atoms and thus all their properties can be relatively easily calculated by DFT. Hundreds to many thousands of atoms can be modeled using the simpler techniques (LDA and GGA), but often the systems of interest require both higher accuracy functionals and larger numbers of atoms. Examples of this include crystalline defects, extended state defects such as line dislocations, surfaces and interactions with them, and alloyed materials. There exist techniques for mitigating the problems of all these types of calculations, but this section will focus on a brief overview of the techniques for modeling alloyed systems.

1.4.1 Random Supercells

The simplest way to model an alloy with random atomic placement is through supercells, or multiples of the primitive cell. Increasing the system size and randomly assigning each site an atom with a probability equal to the occupation fractions will eventually tend towards a perfect model of the random alloy at an infinitely large system size. However, as Kohn-Sham DFT scales roughly as the cube of the number of electrons in the system, its cost becomes prohibitive.

1.4.2 Virtual Crystal Approximation (VCA) & Coherent Potential Approximation (CPA)

The simplest technique for affordably modeling alloys is the Virtual Crystal Approximation (VCA). In an alloy such as a solid solution with both elements of the same crystal structure, the crystal structure can be represented as the crystal structure of either end compound with partial occupancy of the crystal sites by each element in equal fraction to its total atomic fraction composition. The VCA replaces the representations of actual atoms by virtual atoms composed of the linear interpolation of the actual atoms. It thus has the same computational cost for calculating the alloy as for calculating either end compound. However, this is a poor approximation, as all local (structural and electronic) effects, disorder/ordering effects, scattering effects, etc. are not accounted for.

A more complicated version of the VCA is the Coherent Potential Approximation (CPA). This method produces a replacement effective potential that is equivalent to the configurationally random alloy in regards to stationary scattering properties. It is designed for and most useful for scattering dominated processes such as thermal transport in alloys. As it still produces a regular periodic potential, it cannot model local structural effects and provides poor descriptions of total energies and system geometries.

1.4.3 Special Quasi-Random Structures

It is possible to get reasonably accurate representations of random states in finite system sizes. In order to do this, it is necessary to have a measure of randomness in a system and then design a small system to have the desired randomness.

Randomness can be quantified as the degree of correlation between elements in the system. In a perfectly ordered system, knowing the location and identity of a single atom and the ordering of the system tells you with perfect knowledge the location and identity of all other atoms in the system. For systems with known sites but random occupation of those sites, correlation functions between sites give the likelihood of a second site being occupied by a particular atom if the first site is occupied by a particular atom. For example, in a completely random alloy of 50% A, 50% B, knowledge of one site gives you no knowledge about another site's occupant. Therefor the correlation function would be equal to 0. For any composition, the correlation functions of a perfectly random alloy can be analytically determined.

The way to make a system of finite size accurately model a random system of infinite size is therefore to design a system whose correlation functions closely match those of the infinite random system. For most properties of interest in randomly alloyed materials, this assumption is true. These systems are known as Special Quasi-random Structures (SQSs). As there are infinitely many correlation functions, both in distance and in the number of sites included (pair, triplet, etc.), SQS construction makes a couple of assumptions. Firstly, that shorter distance correlations matter more than longer distance correlations. Secondly, that higher order correlation functions matter less than lower order correlation functions. As such, SQSs are typically designed to mimic the first several shortest pair correlation functions of the material. Extension of the process to longer distance and higher order functions is possible, but typically

unlikely to matter beyond 10 Å and triplets. These SQSs can be significantly smaller than the equivalent random supercell. The original paper from 1990 by Zunger et al.[17] shows that an 8 atom SQS for CuPt has an average error in the first 6 pair correlation functions that is approximately the same as a 128 atom supercell using random assignment. With the roughly cubic scaling of DFT, this is a ~4096x more efficient structure to use for the same accuracy.

SQSs for more complicated systems can be difficult to create. As the size of the SQS desired increases, there are an exponentially larger number of possible SQSs to evaluate the pair correlations functions for. To overcome this issue, SQSs are typically created through Monte Carlo algorithms, where atoms are randomly switched within the trial SQSs and the SQS with the correlation functions closest to true random (or with the smallest weighted penalty function if weighting is used) is selected as the best SQS.[18]

1.4.4 Small Sets of Ordered Structures (SSOS)

For systems with many elements, large SQSs can be required to accurately model the random state. In these cases, it can be useful to use a further approximation on top of the SQS approach. The Small Set of Ordered Structures (SSOS) technique assumes that if a set of structures has correlation functions that (weighted) average to the random correlations functions, their (weighted) average property will also average to the random system's property.

This can have large cost savings. Jiang and Uberuaga showed that three 5 atom structures can reproduce the first and second nearest neighbor correlation functions of a 125 atom SQS, and showed good agreement in formation energy of the unrelaxed structures.[19] This corresponds to a speedup of ~5200x. However, they showed slightly worse agreement when including structural relaxation, as shown in Figure 1.1, indicating that not all local effects were captured in the SSOS. Presumably, inclusion of enough terms and careful enough creation of the SSOS could mitigate

this issue, but there is not currently an efficient and robust algorithmic implementation available for generating these sets.

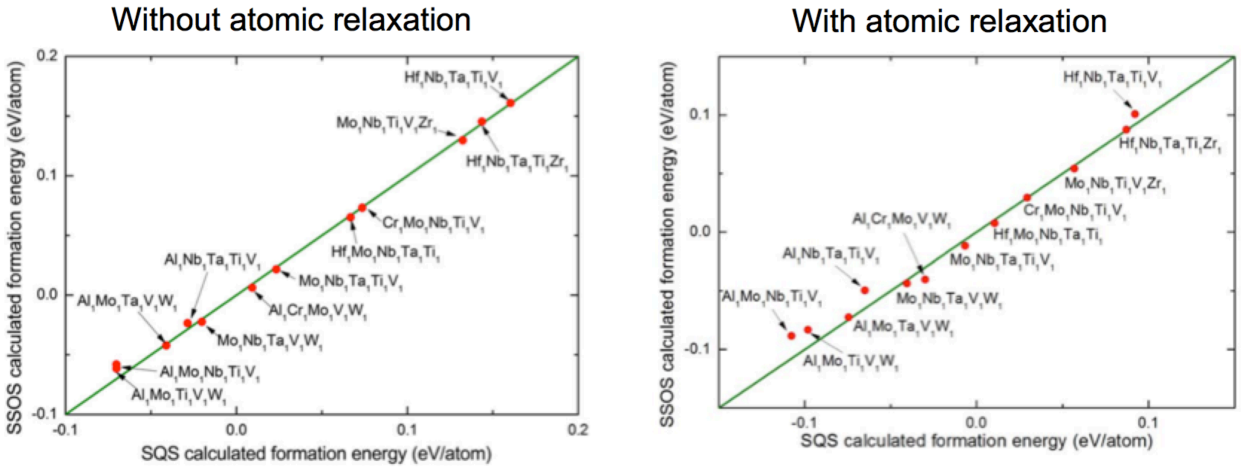

Figure 1.1. Comparison of the calculated formation energies using SSOSs and SQSs both without (left) and with (right) atomic relaxation. Adapted from the original paper.[19]

1.4.5 Cluster Expansion

All of the above methods are designed to model random alloys. However, many technologically relevant systems contain some degree of ordering. Cluster expansion is a related technique that allows for the calculation of a property for an arbitrary system configuration. The basic premise of cluster expansion is that any scalar property dependent upon the configuration of the system can be expressed as a summation of structural motifs present in the system multiplied by the effect of those motifs. Formally, it is a sum over cluster correlation functions multiplied by weights called effective cluster interaction parameters, as shown below:

$$f(\sigma) = J_0 + \sum_{\alpha} \sum_{s} D_{\alpha}^{s} J_{\alpha}^{s} \bar{\Phi}_{\alpha}^{s}(\sigma) \tag{1.13}$$

where D is the degeneracy factor, J is the Effective Cluster Interaction (ECI), Φ is the correlation function, σ is the configuration, and the double sum runs over clusters α and "decorations" *s* that specify the type of point function associated with each site in cluster α. The correlation functions

and degeneracy factors are calculated from the structure. The ECIs must be learned from a training set. Typically, calculations of the property of interest for a collection of small to medium cells with a variety of configurations and compositions are used for training data with least squares fitting used to tune the ECIs. As with SQSs, the lower order clusters and the shorter distance clusters are known to typically be the most important, though this is not a strictly true rule, particularly in structurally complex system. Compressed sensing techniques can be combined with cluster expansion training to weed out clusters with little effect on the property of interest and produce more accurate results at the same cost by including a greater number of relevant terms. Naturally, larger training systems are needed for training clusters of greater size that do not exist by periodic symmetry of a smaller system.

Once a cluster expansion has been trained, if it is well converged and contains all physically relevant clusters, it can accurately predict the property for any system configuration. This causes cluster expansion to require far more initial investment than the other methods mentioned, but allows for great efficiency and versatility with a properly trained model.

Chapter 2 Electronic Properties of $Li_7La_3Zr_2O_{12}$ (LLZO)

This chapter is primarily adapted from the collaborative paper listed below. The author performed the calculations of the band gap and Density of States for the Ta and Al doped series, performed data analysis, and assisted in writing. Additional work not included in the paper is in a section at the end of the chapter.

2.1 Introduction

Li-ion battery technology has advanced steadily over the past few decades.[20–22] Despite these advancements, emerging applications such as electric vehicles would benefit considerably from step-change improvements to the cost, safety, longevity, and capacity of Li-ion batteries.

Optimization of Li-ion systems has largely focused on improving electrode properties, for example, by raising the voltage of cathodes and increasing the capacity of anodes.[20] A promising, yet less examined alternative strategy is to replace the battery's liquid electrolyte with a fast ion-conducting solid.[23] A viable solid-state electrolyte could unlock several high-capacity battery concepts. Examples include Li−S batteries, metal−air batteries, solid-state batteries employing Li metal anodes, and all-oxide solid-state Li-ion batteries. The substitution of flammable liquid electrolytes with stable solid-state compounds also offers clear safety

* DOI: 10.1021/acsenergy-lett.6b00593.

advantages.[24,25] Finally, the wide electrochemical window of some solids could enable the use of high-voltage cathodes, resulting in additional gains in energy density.

The garnet mineral structure represents a family of complex oxides spanning a broad range of compositions. Of the possible garnet formulations, the cubic phase with composition $Li_7La_3Zr_2O_{12}$ (LLZO) has recently emerged as one of the most promising solid electrolytes.[24–27] Garnets are typically wide band gap oxides that are expected to be stable at high oxidation potentials.[28] Earlier studies have also suggested that some formulations of LLZO are stable against Li metal.[29,30]

These features suggest that high-energy LLZO-based cells combining Li metal anodes and ~5 V cathodes may be within reach. Despite this promise, limited understanding of several properties of LLZO presents potential roadblocks to its implementation. One such property is the electrochemical window (EW). The EW determines an electrolyte's resistance to undesirable electronic transport, and by extension controls phenomena such as short-circuiting and self-discharge. Accurate estimates do not yet exist for basic EW-related properties of LLZO such as its band gap and the positions of its band edges. These properties are now routinely examined in the assessment of liquid electrolytes,[31–34] but have not been thoroughly explored for solid electrolytes. Moreover, experimental measurements of the LLZO EW often employ transient techniques such as cyclic voltammetry (CV), which can be insufficient to determine electronic transport properties.[35] Lacking these data, it is unclear whether the promising performance reported for LLZO represents an intrinsic property of the bulk phase or is instead a consequence of fortuitous "kinetic stabilization" arising from interfacial reactions with the electrodes.[20,36,37]

The present study aims to close this knowledge gap by assessing the intrinsic EW of LLZO-based solid electrolytes using multiple experimental techniques and first-principles

calculations. Direct current (DC) polarization measurements were performed over a range of voltages of relevance for high- voltage cathodes. These measurements confirm that LLZO is both a fast ion conductor and an excellent electronic insulator, as the fraction of the total current attributable to electronic carriers is less than 10^{-4}. These observations are consistent with the large band gap predicted for LLZO, ranging from 5.5 to 6.4 eV, determined using a combination of optical measurements and quasi-particle calculations. The position of the valence band maximum (VBM) in bulk LLZO further supports the observation of limited electronic transport at high (positive) voltages: p-type conduction arising from hole injection into the valence band is hindered by the low energy of the VBM, which is ~6 V more positive than the Li/Li^+ redox potential. In addition, the conduction band minimum in LLZO is predicted to lie slightly above Li/Li^+, suggesting moderate stability against electron injection (n-type conductivity) from the Li anode. These data indicate that a wide EW is an intrinsic property of LLZO, facilitating its use in next-generation batteries.

2.2 Methodology

Cubic LLZO garnet with the nominal composition $Li_{7-x}La_3Zr_{2-x}Ta_xO_{12}$ (x = 0.25, 0.5, 0.75, and 1.5) and $Li_{6.5}Al_{0.25}La_3Zr_2O_{12}$ were synthesized and assembled into Li/LLZO/Au cells. Details of the sample preparation can be found in previous reports[38] and in the Supporting Information. Chronoamperometric and alternating current (AC) electro-chemical impedance spectroscopy (EIS) measurements were used to evaluate the EW of LLZO. Chronoamperometric steps between 3 and 8 V vs Li/Li^+ were held for 2 h, after which the steady-state current was recorded. This current is electronic owing to the semiblocking cell configuration.[39] EIS from 7 MHz to 50 mHz using a 50 mV sinusoidal amplitude was performed at the end of each chronoamperometric step while maintaining the applied bias.

The band gap of Al-doped LLZO was determined by measuring the optical absorption of light transmitted through a dense transparent specimen of $Li_{6.17}Al_{0.28}La_3Zr_2O_{12}$ prepared from hot-pressed powder,[40] cut to 1 mm thickness and polished. The absorption coefficient, α, was measured for wavelengths from 190 to 600 nm (UV-1601, Shimadzu, Japan). A Tauc plot of $(\alpha h\nu)^{1/r}$ versus $h\nu$ was used to determine the optical band gap. Here $h\nu$ is the energy of light, while the exponent r relates to the direct (e.g., $r = 1/2$) or indirect nature of the band gap.[41]

First-principles calculations were used to predict the density of states (DOS), band gap, and absolute positions of the band edges for LLZO. All calculations were performed with the projector-augmented wave method, as implemented in the Vienna Ab initio Simulation Package.[42] Three different levels of theory were employed: (i) the semilocal generalized gradient approximation (DFT-GGA) of Perdew, Burke, and Ernzerhof (PBE);[7] (ii) the hybrid functional of Heyd, Scuseria, and Ernzerhof (HSE06);[14,16] and (iii) quasi-particle (QP) calculations based on many-body perturbation theory (G_0W_0 method).[43] These methods were recently used to predict the band gaps of antiperovskite superionic conductors[44] and the EW of liquid electrolytes at electrode interfaces.[34] A 4-formula-unit primitive cell was used for DOS and band gap calculations, in combination with quasi-random Li-site occupations that satisfy the experimental occupancy ratio of symmetry-equivalent sites.[45]

2.3 Results and Discussion

Figure 2.1 illustrates the Tauc plot used to determine the band gap of LLZO. These data suggest that Al-doped LLZO exhibits a large optical gap of approximately 5.5 eV. This value agrees well with the band gaps predicted by first-principles computations, shown in Table 2.1. Band gaps calculated at the HSE06 level of theory are approximately 5.8 eV and are largely insensitive to the Ta or Al doping level. Quasi-particle calculations based on the G_0W_0 method

yield slightly larger gaps of 6.07 (PBE+G_0W_0) and 6.42 (HSE06+G_0W_0) eV. GW calculations, in particular those based on HSE06 input wave functions, typically yield highly accurate band gaps that are in better agreement with experimental photoemission data than those predicted by hybrid functionals.[46] (The slightly smaller gap suggested by our absorption measurements is likely due to exciton effects, which yield a smaller effective band gap relative to photoemission measurements.) These factors lead us to conclude that the band gap of LLZO is best approximated by the HSE06+G_0W_0 gap of 6.4 eV.

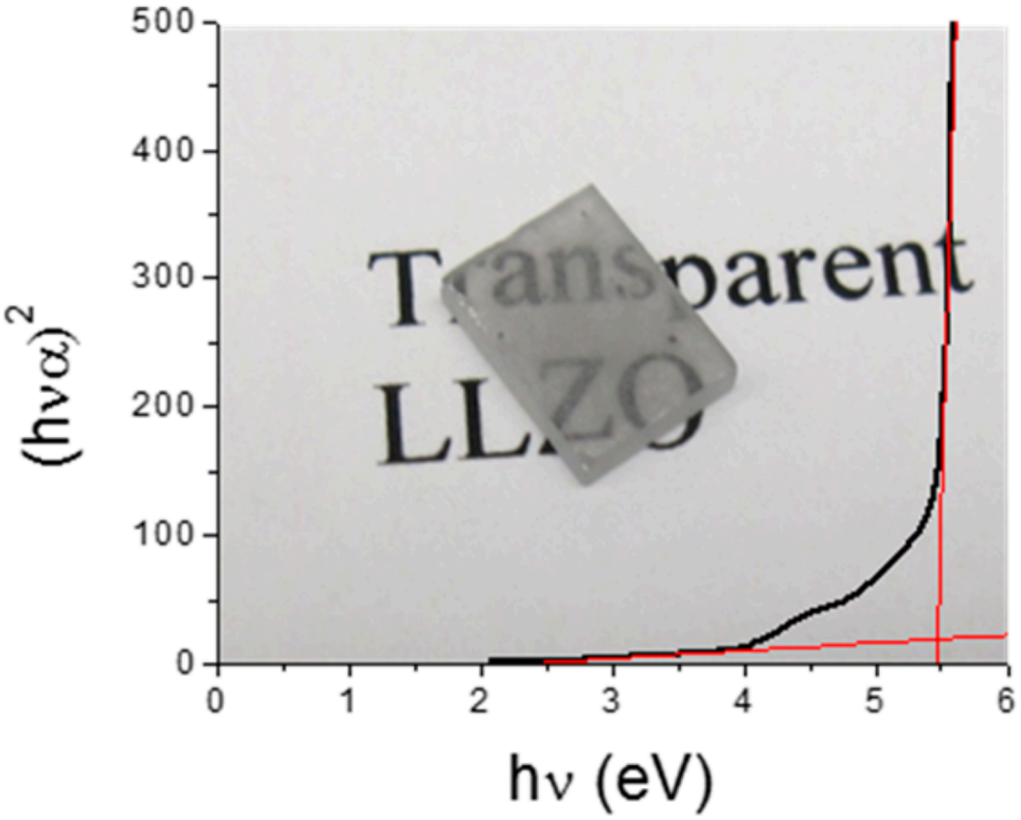

Figure 2.1. Tauc plot of the optical absorption measurement for Al-doped LLZP with an optical band gap of 5.46 eV indicated by the intercept of the two fitted lines

Table 2.1. Band Gap, Electronic Conductivity, and Peak Potential for LLZO as a Function of Composition[a]

	0.25 Ta	0.5 Ta	0.75 Ta	1.5 Ta	0.25 Al	undoped LLZO
calculated band gap [eV]	–	5.85	5.83	5.86	5.87	5.79, 6.07,[b] 6.42[c]
measured optical band gap [eV]	–	–	–	–	5.46	
median electronic conductivity [$\times 10^{-9}$ S cm^{-1}]	2.1	1.5	1.4	1.1	1.4	
peak potential [V]	5.0	5.75	5.5	5.5	5.75	
electronic conductivity at min. transference no. [$\times 10^{-9}$ S cm^{-1}]	5.0	2.3	6.2	4.8	5.9	

[a]Unless otherwise indicated, calculated band gaps are reported at the HSE06 level of theory. [b]PBE+G_0W_0. [c]HSE06+G_0W_0.

The large band gap reported here is consistent with earlier CV measurements[47] suggesting that LLZO should be compatible with high-voltage cathodes. Nevertheless, it is important to recognize that a large band gap is a *necessary, but not sufficient* condition for a suitable EW; it is also desirable for the LLZO band edges to be positioned so as to avoid the transfer of electronic species (electrons or holes) to/from the adjacent electrodes. For example, tunneling of electrons into the LLZO conduction band from the negative electrode could generate undesirable n-type electrical conductivity, ultimately short-circuiting the battery. Similarly, the creation of holes in the conduction band via charge transfer to the positive electrode (p-type conductivity) should also be avoided.

The possibility for the emergence of electronic conductivity in LLZO under an applied bias was assessed by measuring the ionic transference number, t_i, as shown in Figure 2.2a. The

transference number was observed to be nearly equal to 1 ($t_i > 0.9999$) over the entire voltage window examined and is largely insensitive to the LLZO composition. This indicates that the vast majority (>99.99%) of the conductance arises from ionic transport. Furthermore, because the Li ions migrate within a rigid ceramic framework of ions with far lower mobility (i.e., the Zr, O, and La sublattices), essentially all of the ionic conduction can be attributed to the transport of Li ions. The median electronic conductivity for each composition over the potential range measured is listed in Table 2.1. These values range from 1.1 to 2.1 × 10^{-9} S/cm and agree well with measurements made at single potential points.[48,49]

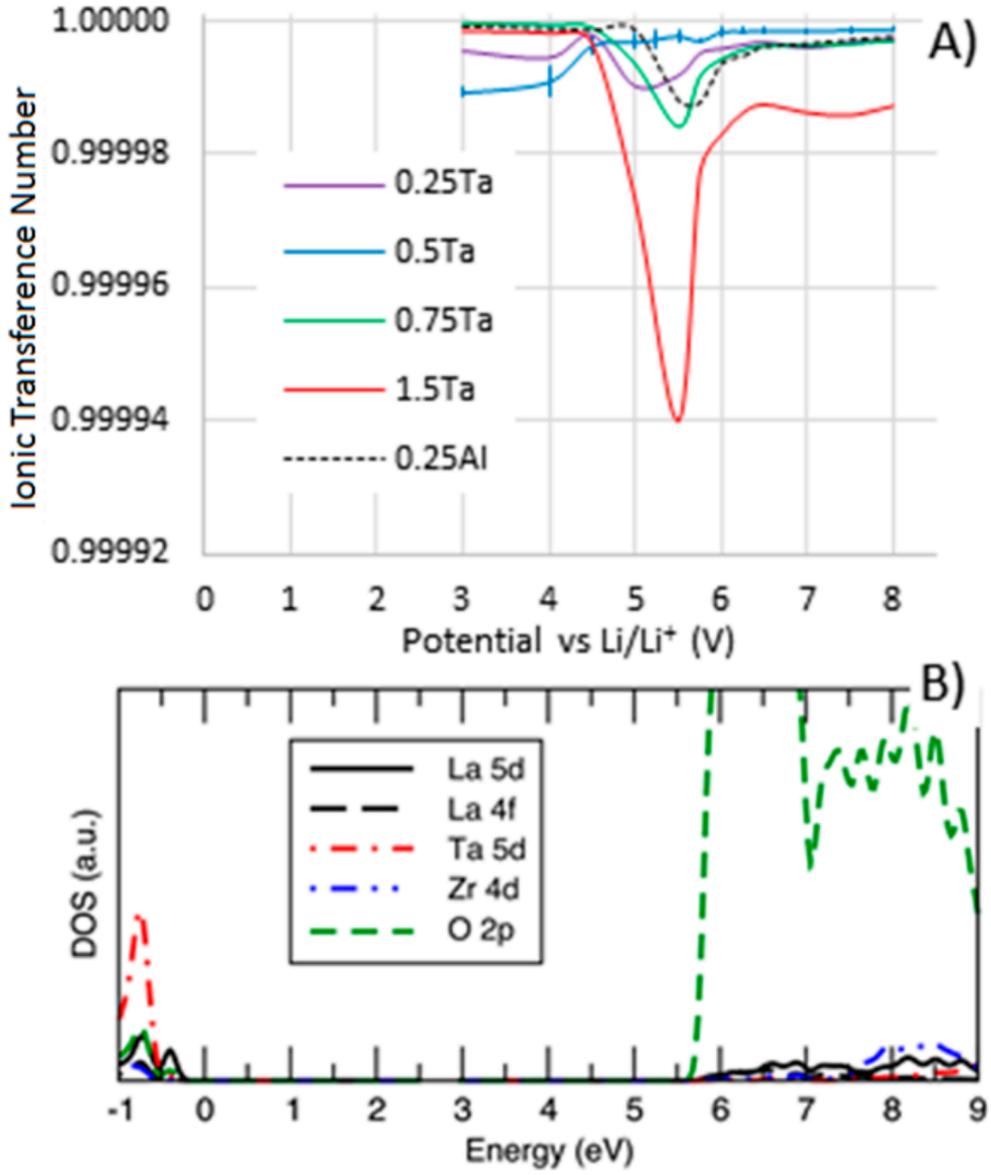

Figure 2.2. (a) Ionic transference number determined from DC galvanostatic polarization and EIS measurements. (b) Calculated partial density of states for the Ta = 0.75 LLZO composition, illustrating the orbital character of the band edges. The PDOS is scaled to match the band edge positions calculated used HSE+G_0W_0. The abscissa in both panels is aligned to facilitate comparisons between the transference number and the DOS.

While the transference number data indicate that transport in LLZO is almost entirely ionic, we note that the transference number versus voltage data shown in Figure 2.2A exhibits a small dip near 5.5 V vs. Li/Li^+ and then recovers at more positive voltages. Consequently, the 5−6 V region exhibits a slightly higher electronic conductivity; nevertheless, the electronic conductivity never exceeds 0.01% of the ionic conductivity in this voltage window and is an

even smaller fraction of the total conductivity outside of this window. As the Ta content decreases from Ta = 1.5 to Ta = 0.5, the magnitude of the dip in t_i also decreases, suggesting a correlation with Ta content. (For Ta = 0.25, the decrease in t_i occurs over a range of voltages. As reported previously,[38] the Ta = 0.25 composition is a mixture of cubic and tetragonal phases, and this most likely accounts for the broader decrease in t_i.) Similar to the Ta = 0.5 composition, the Al-doped LLZO exhibits a dip in t_i near 5.75 V. As described in more detail below, the voltage at which the dip in t_i is observed is similar to the calculated position of the LLZO valence band maximum (VBM). This suggests that the dip in t_i may arise from the injection of holes into the VBM at these voltages.

EIS was performed at each applied bias to confirm that the increase in current associated with the dip in t_i (Figure 2.2A) arises from an increase in electronic transport. Nyquist plots of the complex impedance data indicate that the total ionic conductivity does not change with increasing bias. Furthermore, the magnitude of ionic conductivity agrees well with the bulk and total ionic conductivities of Ta-doped samples investigated previously using blocking electrodes.[38,50] As described by Huggins,[39] the low-frequency response of a nonblocking or semiblocking cell can indicate mixed conduction. In the present study, no electronic conduction was observed in the impedance data at open circuit, and the cell exhibited blocking behavior as expected. As the applied bias approached 6 V, the low-frequency response did indeed exhibit an electronic contribution. This contribution decreased again at higher voltages. Thus, the AC data is consistent with the DC data shown in Figure 2.2A.

Cyclic voltammetry (CV) was performed on each cell at the conclusion of DC polarization measurements. Similar to previous reports,[47] plating and stripping of Li was observed around 0 V vs. Li/Li^+, and no faradaic peaks were observed for applied voltages larger

than 3 V vs. Li/Li^+. These measurements highlight the inadequacy of the transient CV technique in evaluating the EW: no change in the current flow is observed with CV even though a change in the electronic transport is clearly observed in DC measurements in an equilibrated cell. The combination of DC and AC methods used in the present study allows for the ionic and electronic portions of the total conductivity to be separated. These techniques suggest that the LLZO EW spans the range of voltages tested (up to 8 V), at least for the electrodes used here. Of course, the presence of a realistic cathode, as opposed to the inert Au electrode employed here, could generate interfacial chemical reactions absent from the present cell.[37,51] We next describe why only limited electronic conduction is observed in LLZO, given that the band gap (~6 eV) is smaller than the largest bias tested (8 V).

Density functional theory (DFT) calculations were performed to clarify the electronic conduction mechanism in LLZO. The calculated partial density of states of Ta-doped LLZO is shown in Figure 2.2B. To facilitate comparisons with the voltage ranges shown in the transference number plot (Figure 2.2A), the energy axis is mirrored from a standard DOS, such that the conduction bands are plotted at low energy (equivalent to more negative voltages) and the valence bands are shown at higher energy (equivalent to more positive voltages). In addition, the band edge positions are set to match those from our GW calculations.

With this alignment it is evident that the valence band edge in the DOS coincides with the dip in ionic transference number (Figure 2.2A and Table 2.1) near 5.5 V. At these high positive biases, holes are expected to be injected into the valence band, which consists almost entirely of oxygen 2p orbitals. As previously described, the dip in t_i is small in magnitude; similarly, the measured electronic conductivity remains low at all voltages. This behavior can be explained by the localized nature of the orbitals that host the injected holes. Our DFT calculations show that

the radius of the O 2p orbitals (as determined by the outermost peak of the radial probability distribution of the free ions) is 0.84 Å. In LLZO, the oxygen−oxygen distance as measured by neutron diffraction is approximately 3 Å,[50] resulting in insignificant overlap of orbitals, which is expected to suppress charge hopping between oxygen sites. Thus, even though biasing the cell to >6 V should induce p-type conductivity, the limited overlap between orbitals (i.e., low mobility of charge carriers) suppresses significant electrical conductivity. Furthermore, the decrease in t_i (Figure 2.2A) exists for only a narrow voltage window of 5−6 V and disappears for more positive voltages. This behavior seems counterintuitive, because the thermodynamic driving force for hole injection into LLZO should grow as the bias becomes more positive. The measured behavior could be explained, however, by the formation of an electronically insulating interfacial phase (formed by LLZO oxidation products) that blocks further hole injection.

2.4 Supplemental Information

The Density of States (DOS) was plotted for all Ta and Al doped systems calculated. In all cases, the valence band is composed of O 2p orbitals and the conduction band edge is composed of La 5d orbitals as well as Ta 5d orbitals for the Ta doped systems.

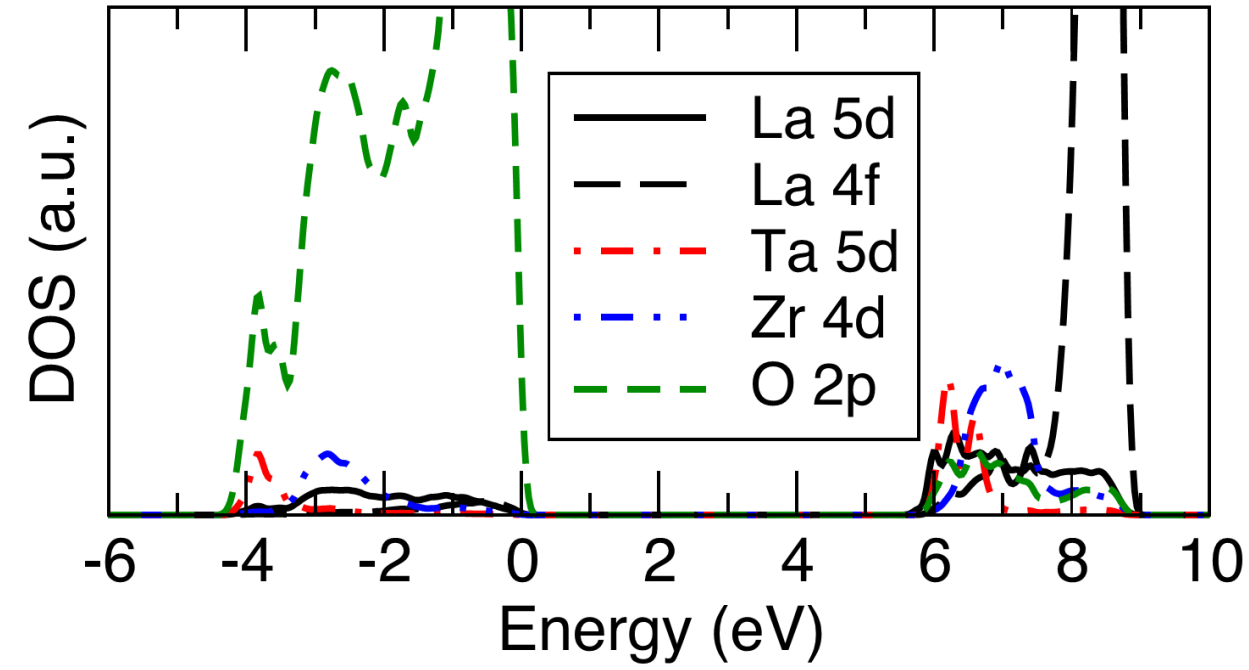

Figure 2.3. Partial density of states for the Ta = 0.5 LLZO composition.

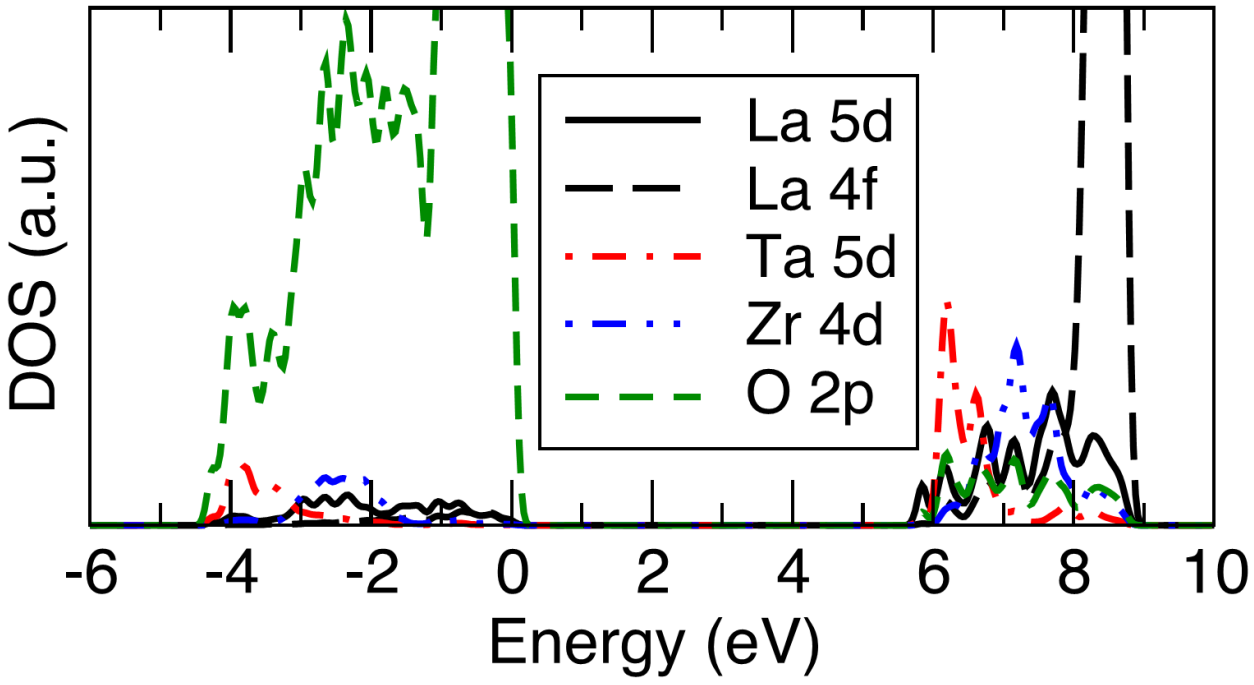

Figure 2.4. Partial density of states for the Ta = 0.75 LLZO composition.

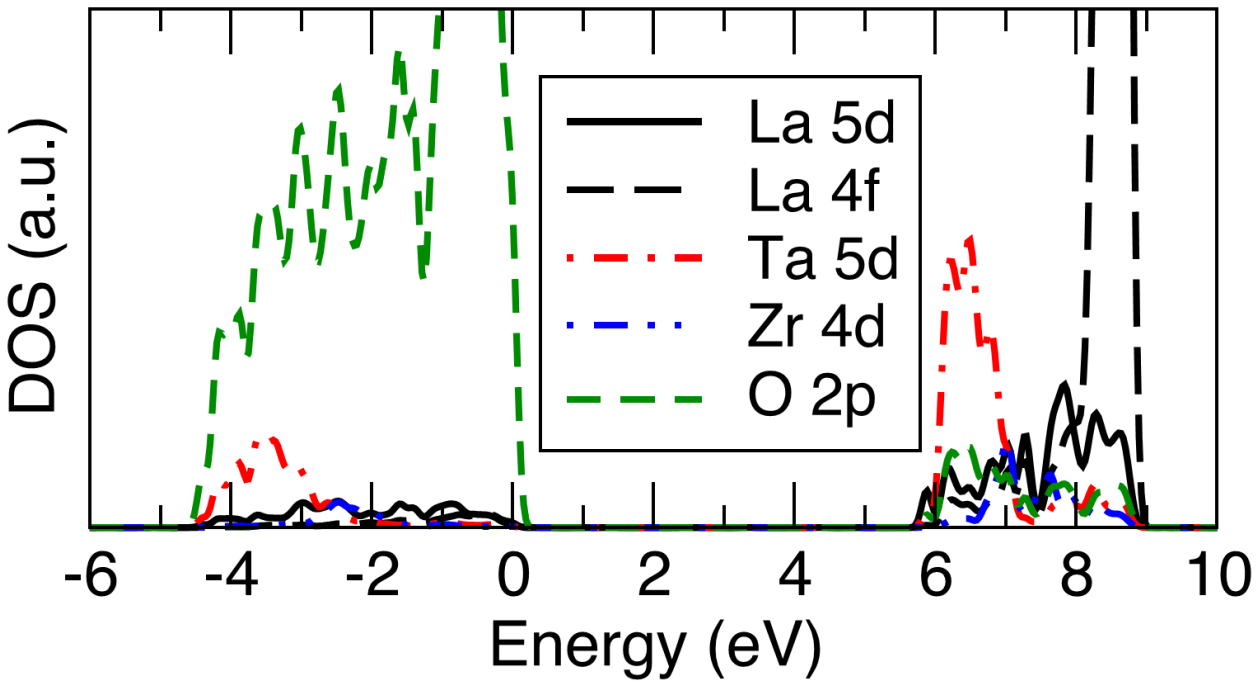

Figure 2.5. Partial density of states for the Ta = 1.5 LLZO composition.

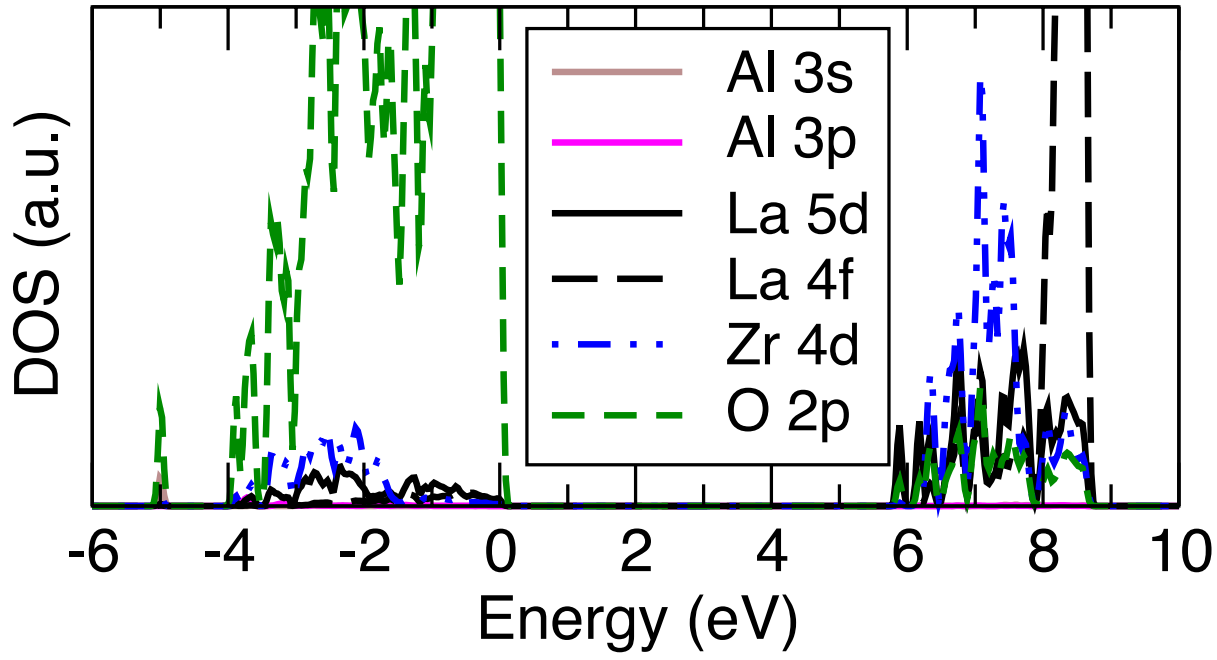

Figure 2.6. Partial density of states for the Al = 0.25 LLZO composition.

2.5 Additional Work

The band structure for several $Li_{6.5}La_3Ta_{0.5}Zr_{1.5}O_{12}$ cells were calculated using PBE and one is shown below. Both the valence and conduction bands are very flat. $Li_{6.5}La_3Ta_{0.5}Zr_{1.5}O_{12}$ has an indirect gap ~5 meV smaller than its direct gap.

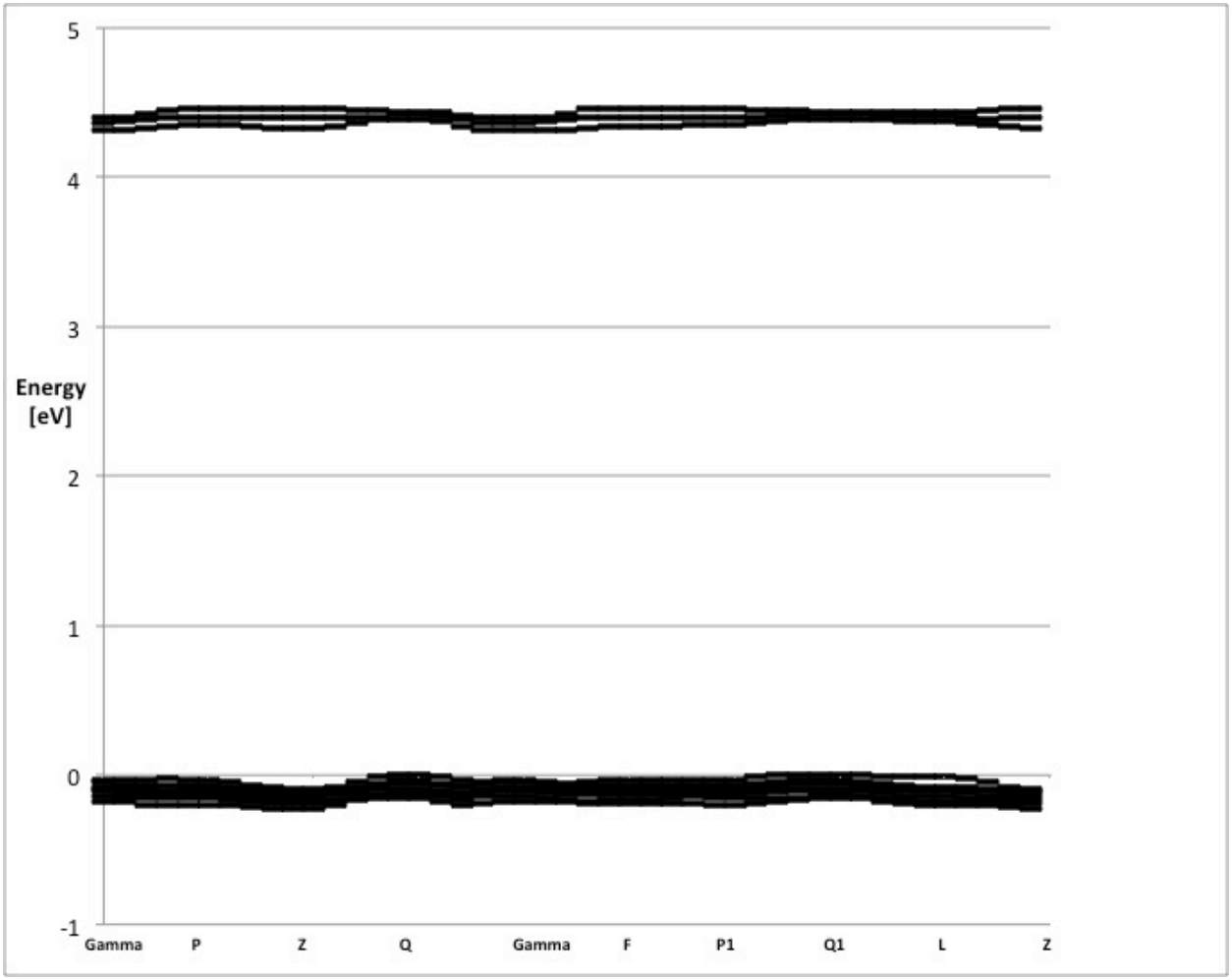

Figure 2.7. Band structure of the bottom three conduction bands and top 7 valence bands of $Li_{6.5}La_3Ta_{0.5}Zr_{1.5}O_{12}$ as calculated by PBE. The gap is indirect by ~5meV.

Charge density iso-surfaces of the valence and conduction band edges of $Li_{6.5}La_3Ta_{0.5}Zr_{1.5}O_{12}$ display the different character of the bands. The valence band is composed of isolated O 2p orbitals, while the conduction band is composed of overlapping La 5d orbitals that connect neighboring La atoms.

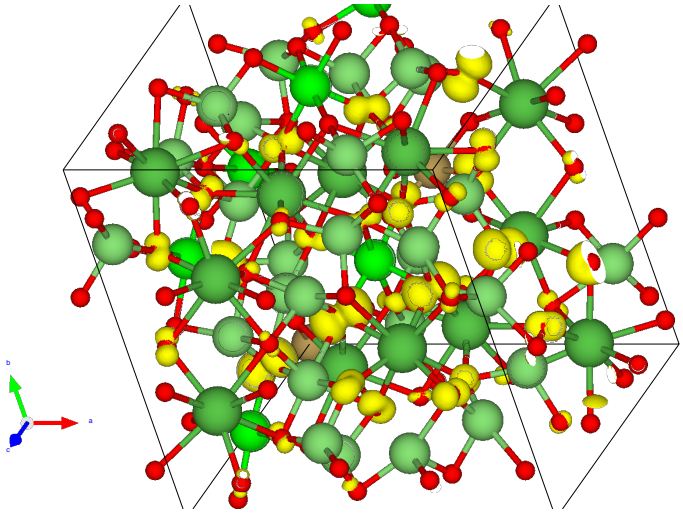

Figure 2.8. Charge density iso-surface of the valence band edge of $Li_{6.5}La_3Ta_{0.5}Zr_{1.5}O_{12}$. Charge (displayed in yellow) is in the shape of O 2p orbitals.

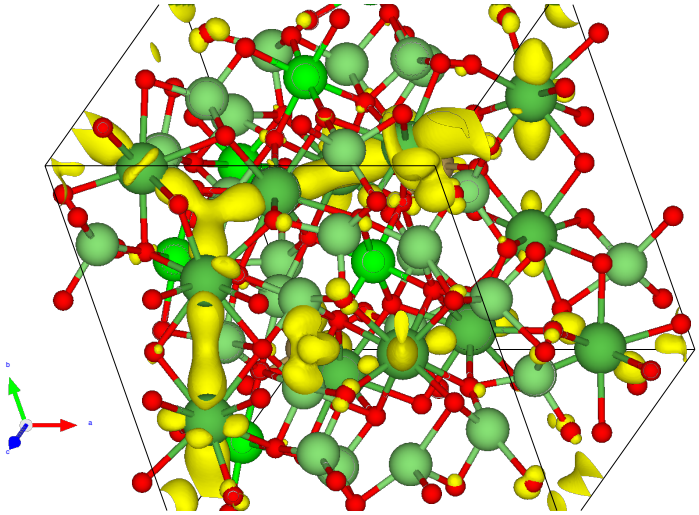

Figure 2.9. Charge density iso-surface of the conduction band edge of $Li_{6.5}La_3Ta_{0.5}Zr_{1.5}O_{12}$. Charge (displayed in yellow) is primarily located at the overlap of La 5d orbitals between neighboring La atoms.

Chapter 3 Defect Mediated Magnetic Coupling in $FeSb_2Se_4$

The work from this chapter has been performed in collaboration with Juan Lopez and Pierre Ferdinand P. Poudeu.

3.1 Introduction

Semiconductors with ferromagnetism and high electrical conductivity at temperatures above 300 K are necessary for the development of practical spintronics devices.[52] Furthermore, the ability to independently control and manipulate the ferromagnetism or conductivity within the material through application of external (electrical or magnetic) fields is required for the creation of memory, field sensor, spin transistor, and quantum information processing devices.[53–56] The most popular approach to create ferromagnetic semiconductors (FMSs) has historically been to substitute magnetic atoms for non-magnetic atoms in conventional semiconductors, creating the so-called diluted magnetic semiconductors (DMSs).[57–62] Most studied DMSs are III-V or II-VI semiconductors with the III or II atom partially substituted by Mn. The Mn atoms are both the dopant species, acting as holes and making the material *p*-type, and the magnetically active species, providing the localized magnetic moments. The Mn atoms in these systems are randomly distributed and sometimes take interstitial positions instead of the intended dopant site.[63–65] These details combined mean that it is not possible to independently control the carrier density, the effective concentration of Mn in the system, and the Mn-Mn separation that controls the magnetic ordering in the system. Due to the difficulty of trying to optimize the linked

properties in these systems, the Curie temperatures (T_c) of *p*-type DMSs has been limited to ~185 K.[54,66,67]

Over the last decade, the Poudeu group has been researching high-T_c FMSs whose structures are composed of ordered arrays of magnetic atoms embedded within a semiconducting network of non-magnetic atoms. The structural separation of the magnetic and non-magnetic ions can potentially allow for independent tuning of the magnetic and electronic conduction properties. Of note are two materials, $FeBi_2Se_4$[68] and $FeSb_2Se_4$[69,70], which are *n* and *p*-type ferromagnetic semiconductors with T_c ~ 450 K. They are isostructural with each other and crystallize in the monoclinic space group *C2m* (No. 12). The structure has 4 crystallographically independent metal sites and four Se positions. The (0, ½, ½) position is fully occupied by Fe, while the (0,0,0) position is 85% Fe + 15% Sb for $FeSb_2Se_4$ and 41% Fe + 59% Bi for $FeBi_2Se_4$. The remaining two metal sites are ~96% Sb + ~4% Fe for $FeSb_2Se_4$ and ~85% BI + ~15% Fe for $FeBi_2Se_4$. The idealized $FeSb_2Se_4$ structure with all sites rounded to full occupancy can be described as Fe atoms octahedrally coordinated by six Se atoms, sharing octahedral edges to form one dimensional Fe chains along the *b* axis. The chains are interconnected by a matrix of Sb atoms in either distorted octahedral or distorted square pyramid coordination with Se atoms.

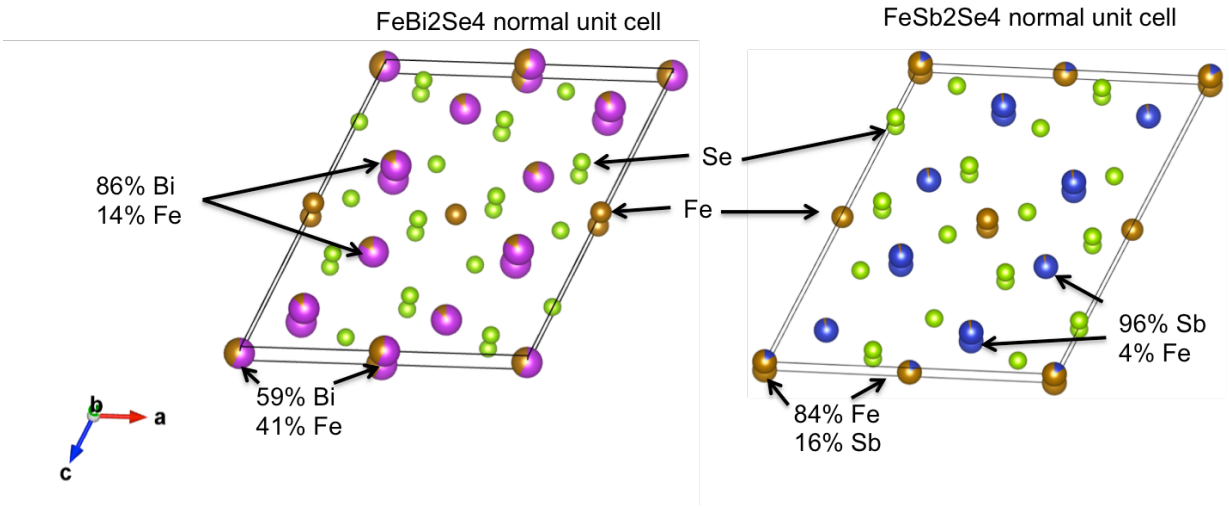

Figure 3.1. Structures of $FeBi_2Se_4$ and $FeSb_2Se_4$ showing the partial occupancy of sites in the structure.

While both $FeSb_2Se_4$ and $FeBi_2Se_4$ are ferromagnetic, they are only weakly so (~4% of if all spins were aligned), and their exact magnetic structure and the mechanisms governing it are currently unknown.

3.2 Methodology

We performed DFT calculations based on the projector augmented wave (PAW) method[71,72] using the Vienna *Ab initio* Simulation Package (VASP).[42,73–75] Pseudopotentials with 14, 6, and 5 valence electrons were used for Fe, Sb, and Se respectively, with a 500 eV plane-wave cutoff. PBE+U was used with a (U-J) parameter of 4 eV for Fe. Forces on atoms were relaxed to within 10 meV/Å. Spin was modeled using the collinear approximation without spin orbit coupling.

3.3 Results and Discussion

Calculations were initially performed under the assumption that the Fe chains would be ferromagnetically aligned. This was later found to be false in the idealized structure. Calculation with the idealized, unitary occupancy structure predicts the material to be antiferromagnetic. The

energy difference between the ferromagnetic and antiferromagnetic states is ~20 meV/magnetic atom.

Calculations with the assumption of ferromagnetic chains revealed an interesting phenomenon that is likely to explain the overall ferromagnetic behavior of the material when extended to the chains as well. Calculation of the idealized structure with ferromagnetic chains predicts that the chains will align antiferromagnetically to one another, as shown in Table 3.1. The energy difference between the ferromagnetic and antiferromagnetic states is ~30 meV/magnetic atom.

Table 3.1. Energy of different magnetic configurations of $FeSb_2Se_4$, under the assumption of ferromagnetic alignment within the Fe atom chains and unity occupation of the sites by their most common occupant. Antiferromagnetic arrangements of the chains are the most energetically favorable. The configurations correspond to the atoms labeling scheme shown in Figure 3.2.

#	Configuration	ΔE from lowest [meV/magnetic atom]	Net Magnetization
8	↓-↑-↑-↓	0	0
7	↑-↓-↑-↓	0.25	0
4	↑-↓-↑-↑	9.5	4
5	↓-↑-↑-↑	9.5	4
2	↑-↑-↑-↓	15.5	4
3	↑-↑-↓-↑	15.5	4
6	↑-↑-↓-↓	20.25	0
1	↑-↑-↑-↑	29.5	16

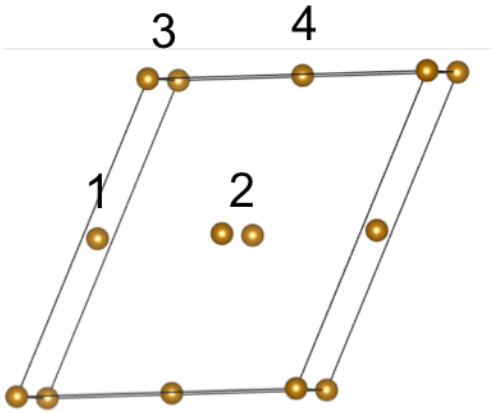

Figure 3.2. Schematic representation showing the $FeSb_2Se_4$ unit cell with only the Fe atoms shown. The labels correspond to the ordering of the configuration labels in Table 3.1.

Inserting a single Fe_{Sb} antisite defect on a Sb site next to an iron chain produces very different behavior, as shown in table 3.2. In this case, partially ferromagnetic configurations are the most energetically favorable. In the case of the Fe_{Sb} shown in figure 3.2, the defect acts to ferromagnetically couple the two chains located above it in the *c* direction.

Table 3.2. Energy of different magnetic configurations of $FeSb_2Se_4$, under the assumption of ferromagnetic alignment within the Fe atom chains and unity occupation of the sites by their most common occupant, except for the inclusion of one Fe_{Sb} antisite defect, as shown in Figure 3.3. The Fe_{Sb} defect stabilizes partially ferromagnetic arrangements of the Fe chains in the structure.

Rank	Configuration	ΔE from lowest [meV/magnetic atom]	Net Magnetization – final (initial)
1	↑-↓-↑-↑-↓	0	11.08 (12)
2	↓-↑-↑-↑-↑	1.67	19.3 (20)
3	↑-↓-↑-↑-↑	3.44	19 (20)
4	↑-↓-↓-↓-↑	3.56	-11.08 (-12)
5	↑-↑-↓-↓-↓	6.44	-3.38 (-4)
6	↑-↓-↓-↑-↑	7.11	3.47 (4)

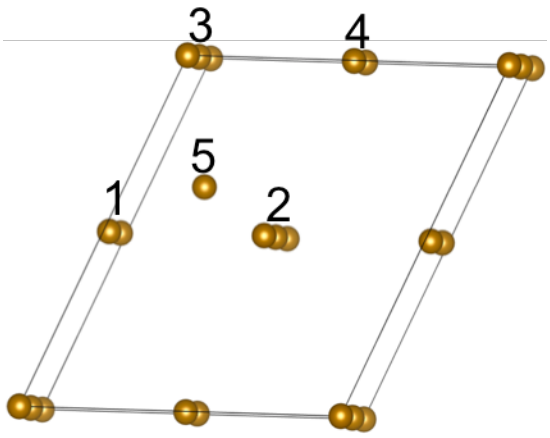

Figure 3.3. Schematic representation showing the $FeSb_2Se_4$ unit cell including one Fe_{Sb} antisite defect with only the Fe atoms shown. The labels correspond to the ordering of the configuration labels in Table 3.2. The antisite defect causes ferromagnetic coupling of the two chains located above it in the z direction.

Antisite defects, either Fe_{Sb} or Sb_{Fe}, are likely also responsible for ferromagnetic alignment of Fe atoms along the chains in the structure. The relatively weak ferromagnetism of these materials (~4% of full spin alignment) is predicted to be due to an antiferromagnetic base structure that is partially ferromagnetically ordered by random antisite defects acting to couple local spins.

Chapter 4 Electronic Properties of Cu_4TiSe_4

This chapter is primarily adapted from the paper listed below, in which the author is 2nd author. The author performed the theoretical work except for the phonon dispersion and the elastic moduli, performed data analysis for the Tauc analysis and estimated photoelectric conversion efficiency, and co-wrote the manuscript. Additional work not included in the paper is in a section at the end of the chapter.

Chem. Sci., 2018,**9**, 5405-5414 - Published by The Royal Society of Chemistry.[†]

4.1 Introduction

Solar-cell research has focused on the development of low-cost highly efficient absorber materials. Recently popular materials include metal-halide perovskites, organic–inorganic hybrid perovskites,[76] and copper metal chalcogenides (CMC) such as $CuInSe_2$ (CIS)[77] and $CuIn_{1\_x}Ga_xSe_2$ (CIGS).[78–80] The large absorption coefficient of these materials, coupled with the ability to engineer their band gap by chemical substitution, enable the realization of solar cells with power conversion efficiencies exceeding 20%.[77–79,81,82] Although the efficiencies remain inferior to that of single-junction devices based on bulk crystalline silicon (25.6%),[83,84] and thin-film GaAs (28.8%),[85] the ability of perovskite- and CMC-based materials to be readily solution processed to solar cells[86–89] provides a cost advantage that could pave the way to terawatt-scale deployment of photovoltaic technologies. Despite the promise of these material systems, the

[†] DOI: 10.1039/c8sc00873f

thermal instability of hybrid perovskites, the restrictions on the use of heavy metals (Cd, Pb, etc.), and the limited global supply of indium are roadblocks to the large-scale deployment of the existing leading perovskites and chalcogenide-based technologies. To address these issues, Earth-abundant copper-metal chalcogenides such as kesterites, $Cu_2SnZn(S,Se)_4$ (CZTS), obtained through chemical substitution of In^{3+} atoms in $CuIn(S,Se)_2$ by Zn^{2+} and Sn^{4+}, have been investigated.[89,90] However, the efficiencies of devices based on these materials remain around 12.6% due to relatively low absorption coefficients, compared to CIGS, and unavoidable anti-site defects such as CuZn and ZnCu.[91–94] Therefore, it appears that achieving low-cost, Earth-abundant copper metal chalcogenide solar cells with high efficiency requires the development of new chemical compositions and crystal structures rather than incremental variations of the chemistry of existing structures. Here, we report the discovery of a new ternary Earth-abundant CMC, Cu_4TiSe_4, copper titanium selenide (CTSe), and demonstrate its potential as a promising light-absorber for ultra-thin low-cost high-efficiency solar cells.

4.2 Methodology

4.2.1 Electronic Band Structure and Optical absorption calculations

Density functional and many-body perturbation theory calculations for the band structure and optical properties were per- formed using the Vienna Ab initio Simulation Package (VASP).[42,72–75] The GW series of Projector Augmented Wave (PAW) pseudopotentials was used.[71,72] Valence electrons 11, 12, and 6 were included for Cu, Ti, and Se respectively. Forces on all atoms were relaxed to under 0.005 eV $Å^{-1}$. The plane wave basis set cutoff was set at 700 eV. The electronic convergence criterion was set at 10^{-8} eV. Multiple levels of theory were used. The hybrid functional of Heyd, Scuseria, and Ernzerhof (HSE06)[15,16] was used to relax the crystal structure and to obtain the starting point for subsequent many-body perturbation theory

calculations. Quasi-particle (QP) corrections based on the GW method (G_0W_0)[43] along with the maximally localized Wannier function method as implemented in the Wannier90 code[95] were used to determine the quasiparticle band structure throughout the Brillouin zone. The dielectric functions and the optical absorption coefficient were obtained with the Bethe–Salpeter equation (BSE) method.[96,97] Gamma-centered grids of 4 x 4 x 4 k points were used for all calculations. Convergence parameters of 1440 bands, a 300 eV GW basis set energy cutoff, and a value of 200 for NOMEGA were used in G0W0 calculations. BSE calculations included 32 occupied and 28 unoccupied bands.

4.2.2 Ellipsometry Measurement of Reflective Index (n) and Extinction Coefficient (k)

A spectroscopic ellipsometer (J.A. Woollam Co. M-2000) is used to measure the index of refraction (n) and the extinction coefficient (k) of CTSe thin film. The measurement was carried out at three incident angles of 55°, 65°, and 75°. The ellipsometer measures the amplitude and phase difference of the s- and p- polarized light after their reflection off the sample. Afterwards, an inverse calculation was done in order to extract the optical properties of the film. Since the deposited CTSe film is thin and semi-transparent in certain wavelength ranges, the incident light will penetrate through the film and reach the Si substrate. In order to separate the effect of light absorption by the Si substrate, and accurately determine the refractive index of the deposited CTSe thin-film, a thin layer (~300 nm) of thermal oxide was first deposited on the Si substrate prior to the CTSe film deposition. The additional thermal oxide layer facilitates the decoupling of either film thickness or absorption coefficient contributions to J and D, by providing additional reflected light, and thus, additional information for an accurate evaluation of the refractive index and thickness of the CTSe film during the ellipsometry data fitting process (interference enhancement method).[98,99] The ellipsometry data was fitted with a B-spline model

that takes into account the Kramers–Kronig relation. This experimental setup and modeling determine the quantities n, k and the film thickness. The index of refraction n and the extinction coefficient k are shown in Figure 4.5.

4.2.3 Determination of absorption coefficient and optical band gap

Using the extinction coefficient (k) determined from the fitting of the spectroscopic ellipsometry data (Figure 4.5), we are able to calculate the absorption coefficient using the expression $\alpha = 4\pi k/\lambda = 10\ 135\ 462Ek$, where α is the absorption coefficient in inverse meters, k is the extinction coefficient, and E is energy in eV. The absorption coefficient is then used for Tauc analysis[100] using the equation $y = (\alpha h\nu)^{1/r}$, where *h* is Planck's constant, *v* is frequency and r is a constant (r = 2 for allowed indirect transition and r = 1/2 for direct allowed transition). Fitting the linear portion of the transformed absorption coefficient vs. energy curve enabled determination of both direct and indirect bang gap as the linear regression's x intercept as shown in Figure 4.6a and b.

4.2.4 Estimated Photovoltaic conversion efficiency (EPCE)

The upper limit of the estimated photovoltaic conversion efficiency (EPCE) as a function of thickness of the absorber layer was calculated according to a modified version of the Shockley–Queisser limit as shown in Figure 4.4.[101] The impedance matching factor, or fill factor, and the ratio of open circuit voltage to band gap voltage were left constant at the values expected for full absorption of light into the materials, as tabulated by Rühle.[102] The spectrum losses were modified to account for the fraction of light that would be absorbed for a given thickness, using material absorption coefficients that were interpolated throughout the energy range specified in the AM1.5G solar spectrum.[103] Due to incomplete data, for CdTe, the absorption coefficient from 4.145 eV to 4.429 eV was assumed to remain constant at the 4.145 eV value; this region of

the solar spectrum has a negligible effect on the final result due to the small phonon flux in this region and the relatively high absorption coefficients in this region compared to the 1–3 eV range.

4.2.5 Electronic Transport Measurement

Specimens for simultaneous measurement of the thermopower and electrical conductivity were fabricated by pressing polycrystalline CTSe powder with a uniaxial hot press using graphite dies and plungers. 100 MPa of pressure was applied with the hydraulic system and the furnace shell was evacuated and flushed with argon several times before maintain a constant 20 L min^{-1} flow of argon for the remainder of the pressing time. The furnace temperature was increased to 450 °C at a scan rate of 200 °C h^{-1}, dwelled for 4 hours and finally ramped down to room temperature at 100 °C h^{-1}. Rectangular bars specimen, ~2.0 x 2.1 x 9.5 mm, were cut from the pressed pellets using a wire saw and SiC slurry, then polished to mirror finished using SiC papers. The thermopower and the electrical resistivity were measured simultaneously from room temperature to 525 °C using an ULVAC-RIKO ZEM-3 apparatus. The instrument's precision on the electrical resistivity and the Seebeck coefficient data is ±4%. CTSe exhibits p-type semiconducting behavior as indicated by the positive values of the thermopower and the nearly exponential increase in the electrical conductivity with increasing temperature (Figure 4.9). The thermopower rapidly increases from 30 mV K^{-1} at 300 K to 200 mV K^{-1} at 800 K. The electrical conductivity initially remains constant at 1 S cm^{-1} from 300 K to 450 K and thereafter slowly increase with rising temperature to 4 S cm^{-1} at 600 K. Beyond this temperature, the electrical conductivity drastically increase with further increase in temperature reaching 11 S cm^{-1} at 800 K.

4.3 Results and Discussion

4.3.1 Structure

CTSe crystallizes in the noncentrosymmetric cubic space group $F\bar{4}3c$ (no. 219) at ambient conditions with lattice parameter a = 11.2936 (2) Å and adopts a new structure type that can be regarded as a 2a x 2a x 2a superstructure of sulvanite (Cu_3VS_4).[104] Figure 4.1 shows the structure and some of the structural motifs present in it.

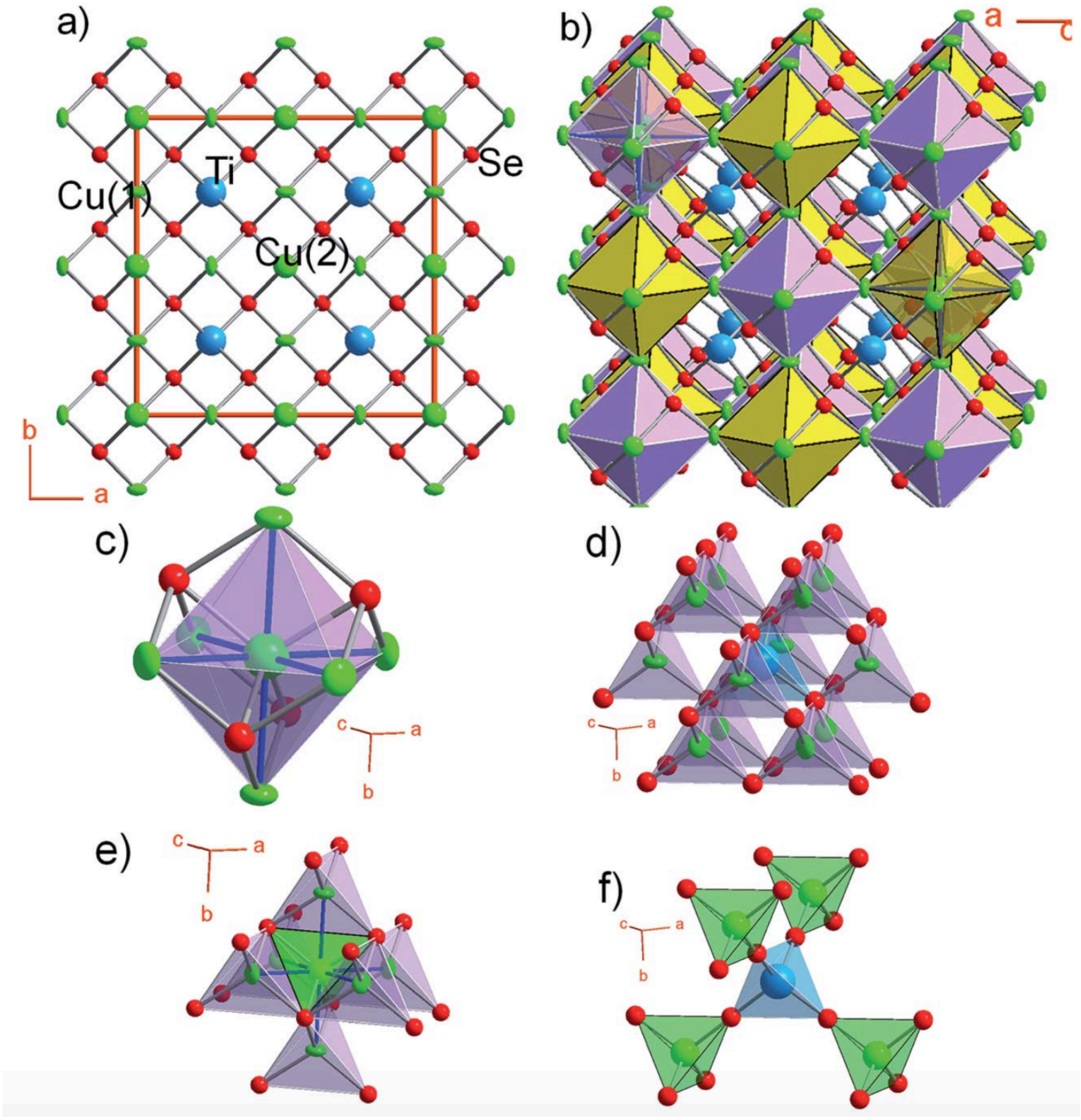

Figure 4.1. Crystal structure of CTSe project along [001]. (a) A ball-and-stick representation showing the 3D connectivity between metal tetrahedra, MSe_4; (b) an alternate polyhedral representation highlighting octahedral building blocks of $[Cu_4Se_4]^{4-}$ anionic clusters. The $[Cu_4Se_4]^{4-}$ anionic clusters form two interpenetrated face centered cubic (fcc) lattices (yellow and purple denote the two sublattices) to generate a 3D structure that is topologically similar to a double perovskite, with Ti^{4+} ions located at tetrahedral sites within the channels; (c) $[Cu_4Se_4]^{4-}$ anionic clusters consisting of a Cu-centered hexanuclear octahedral $[Cu]_6$ cluster capped by Se atoms on four of the eight triangular faces; (d) $TiSe_4$ tetrahedron shares only corners with $Cu(1)Se_4$ tetrahedra; (e) environment of Cu(1) and Cu(2) and their connectivity within the $[Cu_4Se_4]^{4-}$ anionic cluster. $Cu(2)Se_4$ tetrahedron share all edges with $Cu(1)Se_4$ tetrahedra, $Cu(1)Se_4$ tetrahedra exclusively share corners with each other and $Cu(2)Se_4$ tetrahedra are isolated from each other; (f) $TiSe_4$ tetrahedron shares only corners with $Cu(2)Se_4$ tetrahedra and $TiSe_4$ tetrahedra are isolated from each other.

4.3.2 Electronic Structure

Band-structure calculations with hybrid density functional and many-body perturbation theory reveal that CTSe is an indirect-gap semiconductor with a 1.22 eV gap from M to G (Figure 4.2a). However, the minimum direct gap (at M), which determines the onset of optical absorption, is slightly larger at 1.46 eV and close to the Shockley–Queisser optimal value.[101] What makes CTSe particularly promising for solar cells, however, is the large density of states (DOS) near the band edges (Figure 4.2b), which gives rise to optical absorption coefficients larger than 10^5 cm^{-1} throughout the visible range (Figure 4.3). The large DOS derives from the flat valence (which consists of Cu 3d and Se 4p orbitals) and conduction (composed of Ti 3d states) bands. As a result of this unique band structure, CTSe is a superior absorber material for thin-film solar cells compared to GaAs, CIGS, and CZTS (which feature broad s-type conduction bands with a lower density of states), and CTSe thin-film solar cells reach comparable efficiencies at a much lower thickness. The calculated absorption coefficient of CTSe is compared to experiment and other absorber materials in Figure 4.3. CTSe is predicted to outperform all established absorber materials in the 1.1–2.8 eV range that contains most of the terrestrial solar spectral irradiance.

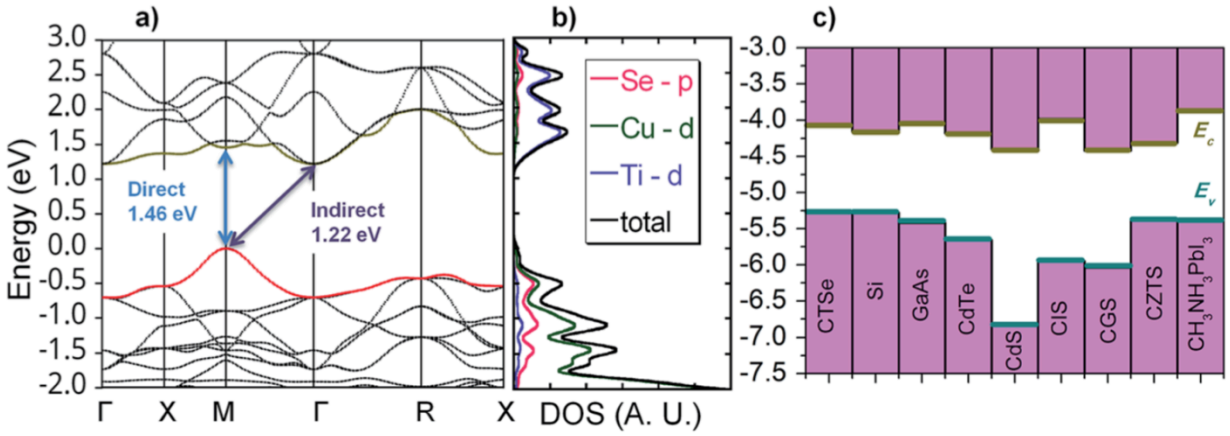

Figure 4.2. Electronic band structure of CTSe. (a) Calculated band structure highlighting the relatively flat valence (VB) and conduction (CB) bands, and the presence of both indirect (1.22 eV) and direct (1.46 eV) band gaps with similar

values. (b) Projected density of states (DOS) highlighting the major orbital contributions; (c) band alignment of CTSe relative to vacuum and other photovoltaic materials.

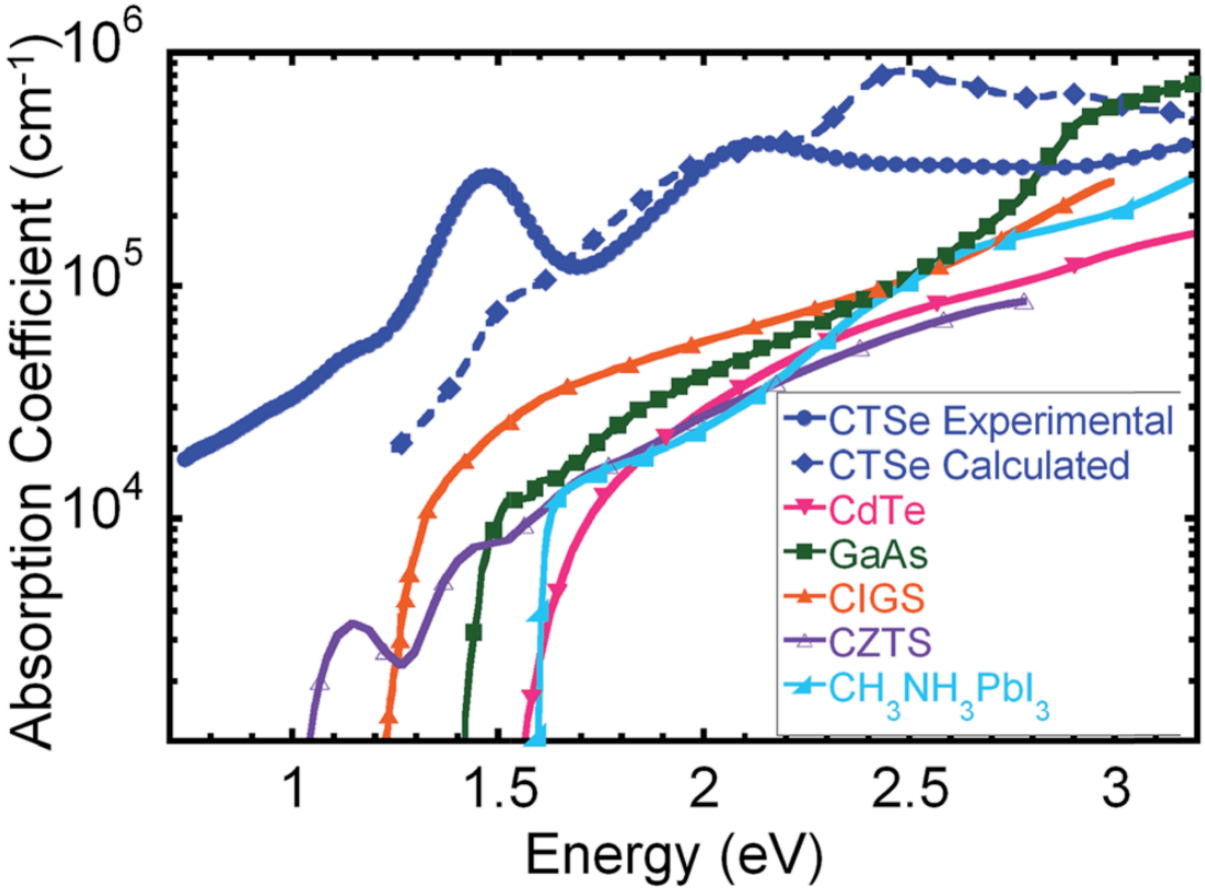

Figure 4.3. Theoretical and experimental absorption coefficients of CTSe compared to leading solar absorber materials such as CdTe,[105] GaAs,[106] CIGS,[107] and CZTS,[108] and $CH_3NH_3PbI_3$.[109] CTSe outperforms all established solar-absorber materials in the 1.1–2.8 eV range.

4.3.3 Optical and electronic properties

The optical properties of the deposited films were characterized by the reflection-type spectroscopic ellipsometry from 200 nm to 1680 nm. The measured refractive index (n) and extinction coefficient (k) of CTSe (Figure 4.7) show a broadband absorption in the visible and near-infrared (near-IR) range and two strong absorption peaks around 650 nm and 900 nm, respectively. The absorption coefficient of CTSe calculated using the extinction coefficient from ellipsometry data is plotted in Figure 4.3 and compared to our theoretical predictions and other

materials. Both the predicted and the measured absorption coefficient of CTSe are larger than 10^5 cm^{-1} and far superior to the absorption coefficients of most traditional solar absorbers such as CdTe, GaAs, CIGS, CZTS, and Si within the range 1.1 eV to 2.8 eV, where most of the light in the terrestrial solar spectrum resides. Careful analysis of the absorption curves using Tauc fitting enables the determination of experimental indirect band gap of 1.15 eV and direct band gap of 1.34 eV (Figure 4.6). Interestingly, the direct band gap extracted from ellipsometry is very similar to the direct optical band gap of 1.31 eV derived from diffuse reflectance data on CTSe powder sample (Figure 4.7). These experimental values of the band gaps are comparable to the theoretically predicted indirect (1.22 eV) and direct (1.46 eV) band gaps of CTSe, and are well within the Shockley–Queisser range of optimal band gaps (1.1–1.5 eV). In addition, the indirect band gap of CTSe favors long minority-carrier lifetimes and precludes the re-emission of the absorbed photons and the need for photon recycling, in contrast to direct-gap solar absorbers such as GaAs. Moreover, the small energy difference (~0.2 eV) between the direct and indirect gaps implies only a small additional energy loss due to carrier thermalization. These data offer the possibility of creating CTSe based solar cells of equal or superior efficiency to CdTe or GaAs cells at a fraction of the thickness. However, careful examination of the optical absorption curve from ellipsometry measurement on CTSe thin film (Figure 4.3) as well as the diffuse reflectance data (Figure 4.7) measured on CTSe bulk powder sample revealed a tail below the sharp absorption peak. This likely indicates that the as-synthesized CTSe is doped with impurity states located within the band gap. Indeed, the Urbach tail analysis of the absorption curve revealed the presence of three linear regions with Urbach energies 135 meV, 297 meV, and 429 meV within the band gap of CTSe (Figure 4.8). The large values obtained for the Urbach energy point to large concentrations of defects existing within the band gap of CTSe. Our preliminary theoretical

defect calculations indicated that the impurities arose from the formation of Cu vacancies such as V_{Cu} as well as antisite defects.

Temperature dependent electronic transport measurement revealed that CTSe is a p-type semiconductor (Figure 4.9). The thermopower increases with temperature from 30 mV K^{-1} at 300 K to 200 mV K^{-1} at 800 K whereas the electrical conductivity increases from 1 S cm^{-1} at 300 K to 11 S cm^{-1} at 800 K. Interestingly, the temperature dependence of the electrical conductivity show two thermally activated electronic transitions around 400 K and 700 K. Fitting both transitions using the Arrhenius equation $\ln(\sigma) = \ln(\sigma_0) - E_a/KT$ (where E_a is the activation energy and K is the Boltzmann constant) leads to the activation energy of ~140 meV for the transition at 400 K and an activation energy of ~296 meV for the transition at 700 K (Figure 4.10). The observed activations energies are consistent with the Urbach energies calculated from the analysis of the tail of the optical absorption curve, further confirming the presence of localized electronic defects within the band gap of CTSe. Therefore, further work focusing on the reduction of the density of electronic defects within CTSe is needed to improve its potential as solar absorber material.

To quantify the advantages of CTSe for thin-film solar cells, we determined the upper limit of the estimated photovoltaic conversion efficiency (EPCE) as a function of absorber thickness and compared to that of GaAs, CdTe. The EPCE upper limit was calculated by evaluating the fraction of incident light absorbed for each wavelength in the AM1.5G solar spectrum, as determined by the absorption coefficient (Figure 4.3), and by including the spectral losses in the Shockley–Queisser limit.[101–103] The fill factor and the ratio of the open-circuit voltage to the band gap voltage were left at their full absorbance values for this analysis. As shown in Figure 4.4, the estimated maximum efficiency of CTSe obtained using both the

predicted and the measured absorption coefficients is significantly larger than that of GaAs and CdTe at low film thickness. This result is supported by the ultra-large absorption coefficient of CTSe throughout the 1.1–2.8 eV range, which enables higher efficiencies at approximately one order of magnitude lower film thickness compared to CdTe and GaAs. For instance, a maximum EPCE of 30% is anticipated for a 0.2 mm CTSe thin film compared to 5 mm GaAs film for similar EPCE value. This analysis suggests the potential for the production of high-efficiency and flexible CTSe-based solar cell devices at low cost, paving the way to sustainable large-scale deployment of lightweight, high-efficiency solar cells based on absorber materials from cheap and environmentally friendly elements.

The analysis of the band alignment of CTSe relative to other leading p-type solar absorber materials such as Si, GaAs, CdTe, CdS, CIS, CGS, CZTS and $CH_3NH_3PbI_3$ is shown in Figure 4.2c. The conduction band minimum (CBM) of CTSe is located 4.06 eV below the vacuum level and the valence band maximum (VBM) is located 5.28 eV below the vacuum level. This places the band edges very close to those of GaAs (-4.00 eV and -5.39 eV), CdTe (-4.18 eV and -5.66 eV) and $CH_3NH_3PbI_3$ (-3.88 eV and -5.39 eV), a halide perovskite that is currently the focus of intense research efforts for solar cell applications.[86] The similarity of the band-edge positions to established solar absorbers indicate that CTSe may be compatible with commercial solar-cell architectures and manufacturing technologies, which should accelerate the development of optimal CTSe-based devices. However, to achieve such working photovoltaic device based on CTSe, one must first reduce or eliminate the high density of defects (Cu vacancies) that contribute to absorption well below the band gap and therefore hamper the

photoconductivity of the materials.

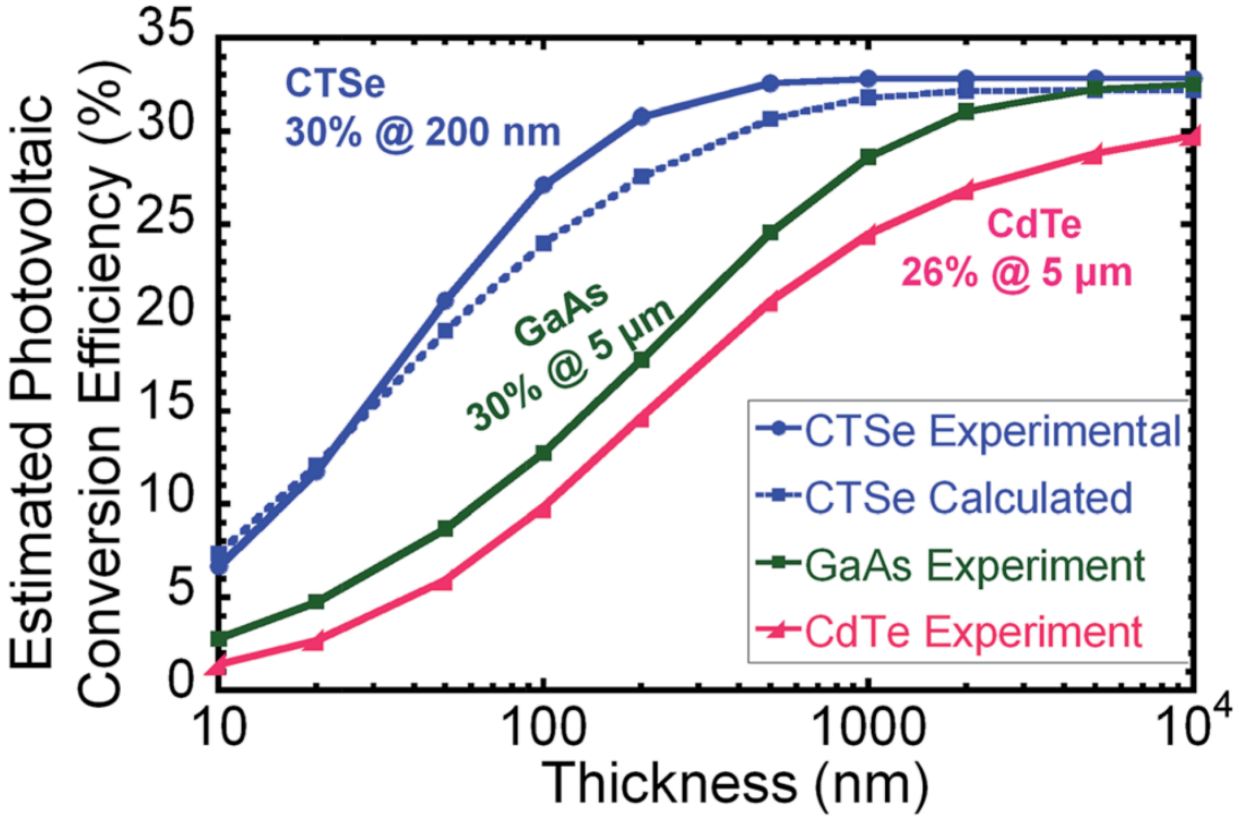

Figure 4.4. Estimated photovoltaic conversion efficiency (EPCE) as a function of thickness for CTSe compared to CdTe[105] and GaAs.[106] CTSe reaches an efficiency of 30% for a thickness of 200 nm, approximately one order of magnitude thinner than typical CdTe or GaAs devices (1.5–5 mm).

4.4 Concluding Remarks

In summary, we discovered a new Earth-abundant ternary copper titanium selenide, CTSe, and assessed its potential as a promising solar absorber for low-cost, scalable, high-efficiency single junction solar cells. CTSe adopts a new cubic structure type in which $CuSe_4$ tetrahedra share both corners and edges to form a 3D framework topologically similar to double perovskite with isolated TiSe4 tetrahedra located within the channels. The unique structural feature of CTSe results in optimal theoretical/experimental band gaps of 1.22 eV/1.15 eV (indirect) and 1.46 eV/1.34 eV (direct), in the optimal range according to the Shockley–Queisser analysis. The Ti 3d orbital character of the conduction band results in ultra-large absorption

coefficient (~10^5 cm^{-1}) throughout the visible, outperforming most traditional absorbers such as CZTS, CIGS, GaAs and CdTe in the 1.1–2.8 eV range. A CTSe material thickness of only 200 nm is needed to outperform GaAs and CdTe solar cells that are typically a few microns thick. In addition, CTSe was found to be stable from energetic, elastic and dynamic aspects, which significantly enhances the prospect of realizing scalable, low-cost, high- efficiency, lightweight, and environmentally friendly next generation solar cells.

4.5 Author Contributions

E. C. synthesized the samples, carried out structural characterization, fabricated CTSe thin-film, performed the SEM characterization, performed data analysis, and co-wrote the manuscript. A. O. helped with sample synthesis, performed structural characterization and data analysis, and co-edited the manuscript. L. W., G. S., and E. K. performed calculations for the electronic band structure, band gap, optical absorption coefficient, and the estimated photovoltaic conversion efficiency, performed data analysis and co-wrote the manuscript. C. Z. and J. G. performed optical property measurement, performed data analysis and co-edit the manuscript. M. Z. and L. Q. performed calculations of phonon dispersion, and elastic constants, performed data analysis and co-edit the manuscript. J. T. H. helped with thin-film fabrication, data analysis and co-edited the manuscript. P. F. P. P. conceived the experiment, performed crystal structure measurement, analyzed the results and co-wrote the manuscript.

4.6 Acknowledgements

We gratefully acknowledge the financial support from the Department of Energy, Office of Basic Energy Science under Award # DE-SC-0008574 for materials synthesis, structural characterization, and fabrication of CTSe thin-film. The band structure and optical absorption calculations were supported by the National Science Foundation through grant number DMR

1561008, and used resources of the National Energy Research Scientific Computing Center, a DOE Office of Science User Facility supported by the Office of Science of the U.S. Department of Energy under Contract No. DE-AC02-05CH11231. This work made use of the SEMs (FEI Quanta3D and FEI Nova Nanolab) from the Michigan Materials Characterization Center, $(MC)^2$, purchased with funds from the National Science Foundation Awards DMR-0315633 and DMR-0723032.

4.7 Additional Tables and Figures

Table 4.1. Selected crystallographic data for Cu_4TiSe_4 at 300K.

Crystal system; space group	F-43c; (No. 219)
Formula weight (g/mol)	1235.8
Density (ρ_{cal}) (g/cm^3)	5.69815
Lattice parameter (Å) $a = b = c$	11.2936(13)
Volume (Å^3); Z	1440.45(29); 4
Crystal size (mm)	[0.05] x [0.05] x [0.05]
Crystal shape, color	Faceted cubic, dark gray
Radiation (Å)	$\lambda(MoK_\alpha) = 0.71073$
μ (cm^{-1})	327.8
Diff. electron density (e/ Å^3)	+2.20 to -1.78
Transmission factor	0.2997 – 0.6709
2range; index range	$6.2° \leq 2\theta \leq 59.80°$; $-15 \leq h \leq 15$; $-15 \leq k \leq 15$; $-14 \leq l \leq 15$
R_1 (Fo>4σ(Fo))[a]	0.0414
wR_2 (all)[b]	0.1025
Goodness of fit	1.030

[a] $R_1 = \Sigma||F_o|-|F_c||/\Sigma|F_o|$; [b] $wR_2 = [\Sigma w(F_o^2-F_c^2)^2/\Sigma w(F_o^2)^2]^{1/2}$

Table 4.2. Atomic coordinates, Wyckoff positions (W. P.), site occupancy factors, and equivalent isotropic displacement parameters (U_{eq} in $Å^2$) for all atoms in Cu_4TiSe_4.

Atom	W.P.	S. O. F.	*x*	*y*	*z*	U_{eq}
Se1	32e	0.33333	0.12432(8)	0.12432(8)	0.12432(8)	0.01274
Cu2	24d	0.25000	1/4	0	0	0.01536
Cu1	8a	0.08333	0	0	0	0.02828
Ti1	8b	0.08333	1/4	1/4	1/4	0.04238

U_{eq} is defined as one-third of the trace of the orthogonalized U_{ij} tensor.

Table 4.3. Selected inter-atomic distances (Å) in Cu_4TiSe_4.

Bond Type	Bond Distance (Å)
Cu2-Se1$^{iii, iv, v}$	2.4407(6)
Cu1-Se1^{iii,vii,viii}	2.4318(2)
Ti1-Se1$^{xi, xii, xiii}$	2.4584(2)

Operators for generating equivalent atoms:
(i) y, z, x; (ii) z, x, y; (iii) x, −y, −z; (iv) 0.5−y, x, −z; (v) 0.5−y, -x, z; (vi) 0.5+y, x, z; (vii) −x, y, −z; (viii) −x, −y, z; (ix) −y, z, -x; (x) z, −x, −y; (xi) x, 0.5−y, 0.5-z; (xii) 0.5−x, 0.5−y, z; (xiii) 0.5−x, y, 0.5−z.

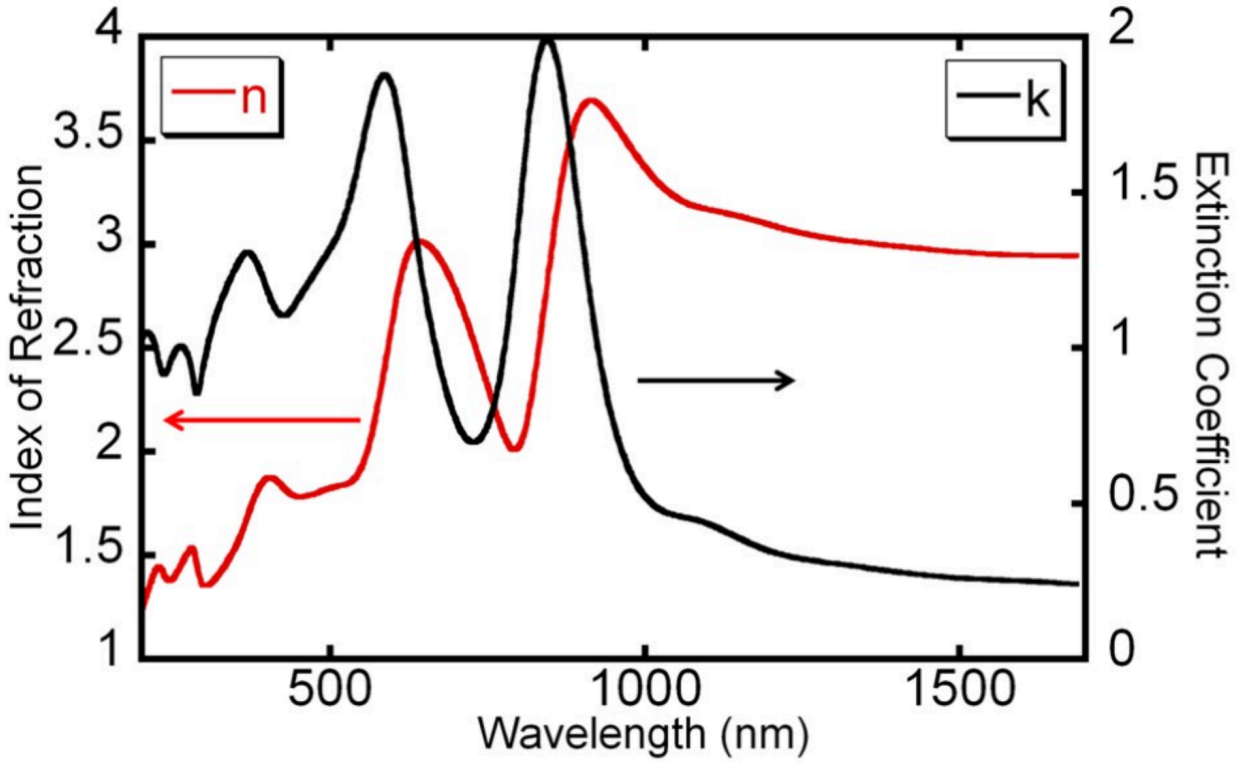

Figure 4.5. Index of refraction (n) and the extinction coefficient (k) as a function of wavelength extracted from ellipsometry data.

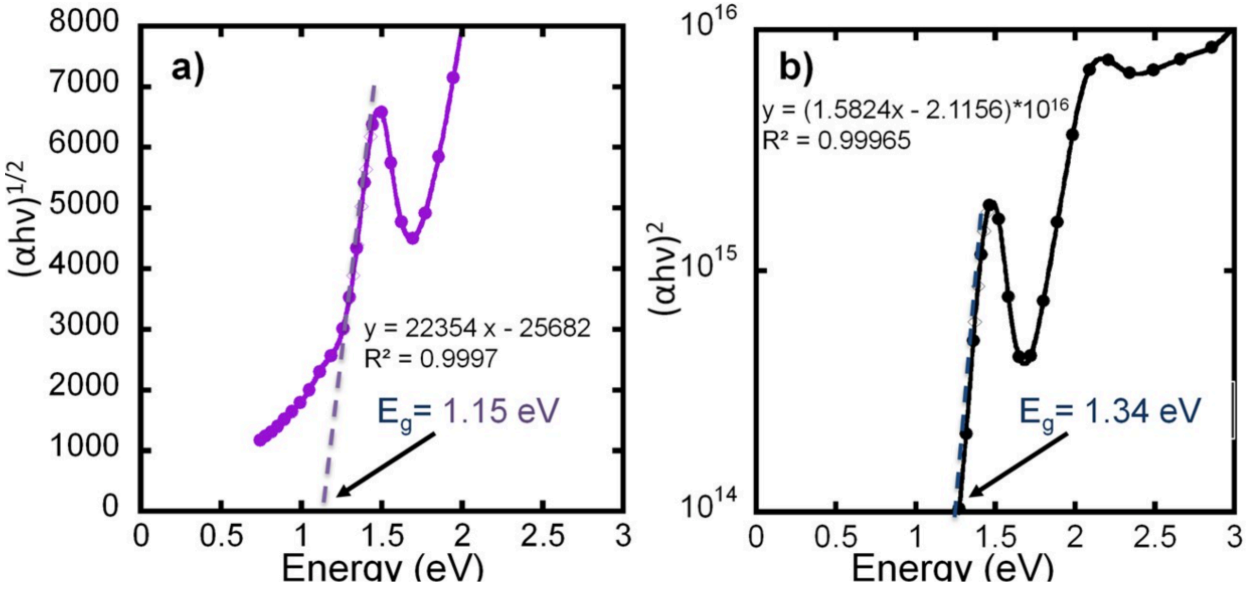

Figure 4.6. Tauc analysis for the determination of optical band gap. a) allowed indirect transition and b) allowed direct transition.

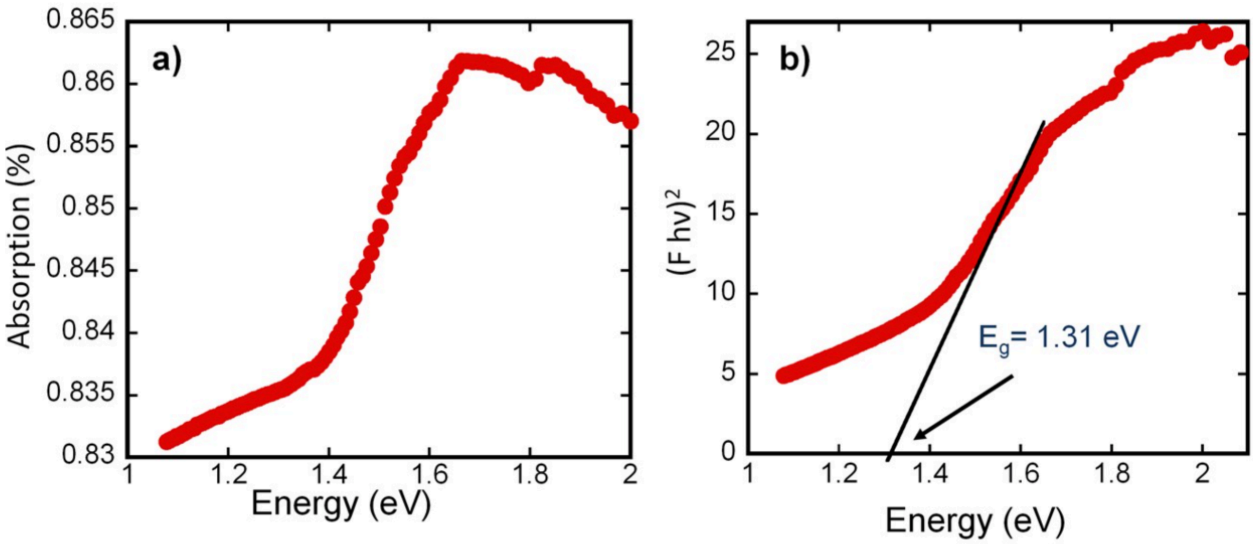

Figure 4.7. (a) Diffuse reflectance data on bulk CTSe powder. (b) Tauc fitting for allowed direct transition using diffuse reflectance data indicating an optical band gap of ~1.31 eV.

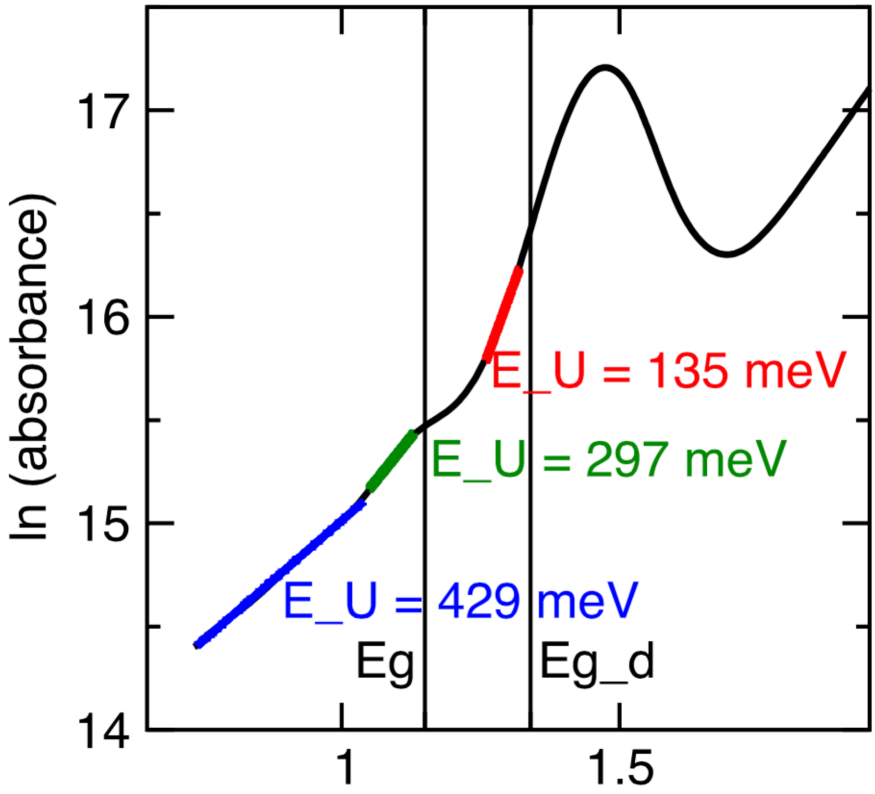

Figure 4.8. Urbach tail analysis of the optical absorbance of CTSe. The Urbach energy is calculated using the empirical formula lnα = lnαo + (hν/E_U) and fitting the linear region of lnα vs hν. Urbach absorption tails typically arise from thermal fluctuation at the band edges or the presence of defects. Three linear regions are present giving Urbach energy (E_U) of 135 meV, 297 meV, and 429 meV within CTSe band gap. The large values obtained for the Urbach energy point to large concentrations of defects existing within the band gap.

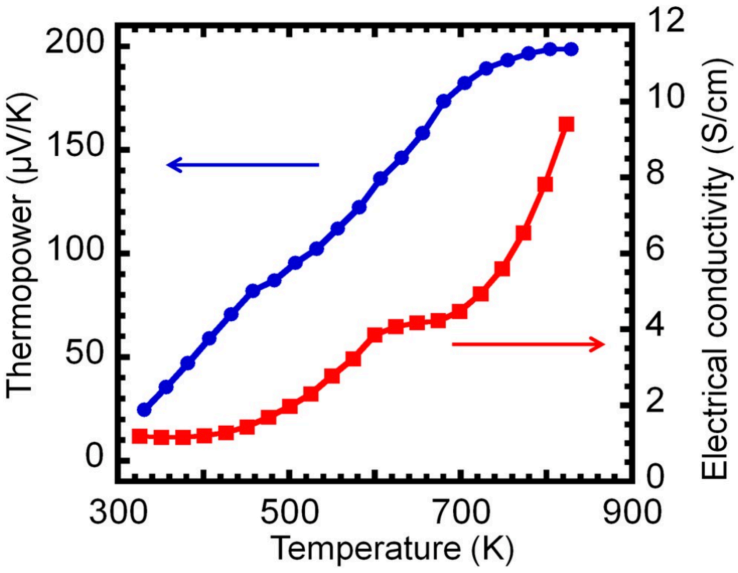

Figure 4.9. Temperature dependence of the thermopower (S) and electrical conductivity (s) of CTSe. The positive values of the thermopower indicate holes as the majority carriers and the gradual increase of the electrical conductivity with rising temperature is consistent with the intrinsic semiconducting behavior of the compound.

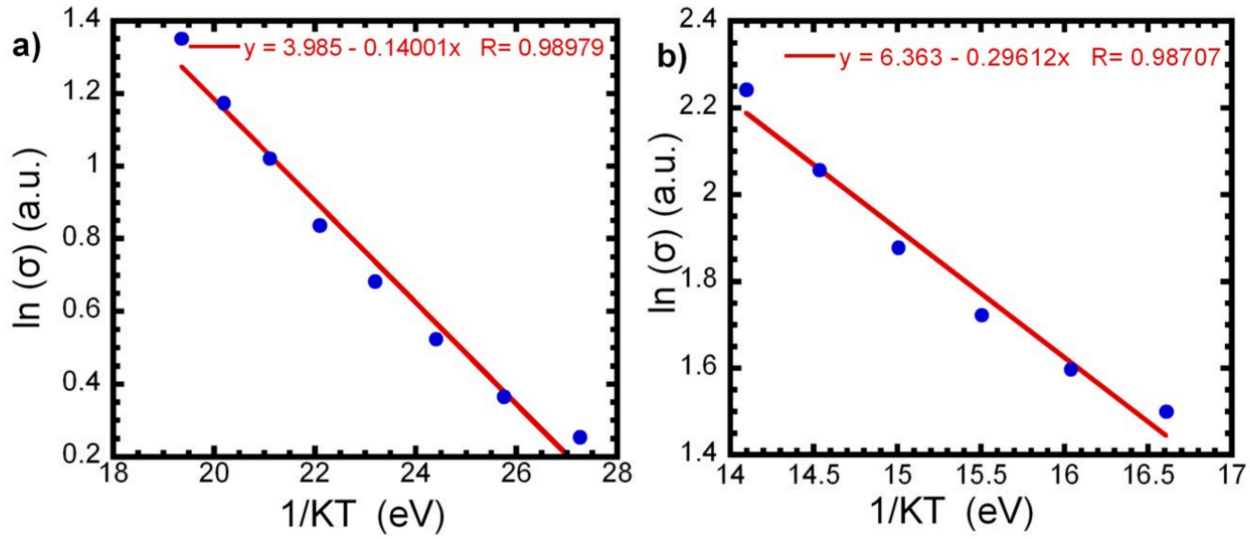

Figure 4.10. Fitting of the electrical conductivity of CTSe using Arrhenius equation for thermal activation conductivity, Ln (σ) = Ln (σ_0) – Ea/KT. (a) low temperature transition (400 to 600 K) with activation energy of ~140 meV; (b) high temperature transition (700 to 800 K) with activation energy of ~296 meV.

4.8 Additional work after the paper

4.8.1 Seebeck Coefficient

The Seebeck coefficient for a range of carrier densities for p-type Cu_4TiSe_4 were calculated from first principles and are show below in Figure 4.11. The values calculated for a

carrier concentration of ~1E21 cm^{-3} are in rough agreement with experiment, as shown in Figure 4.12.

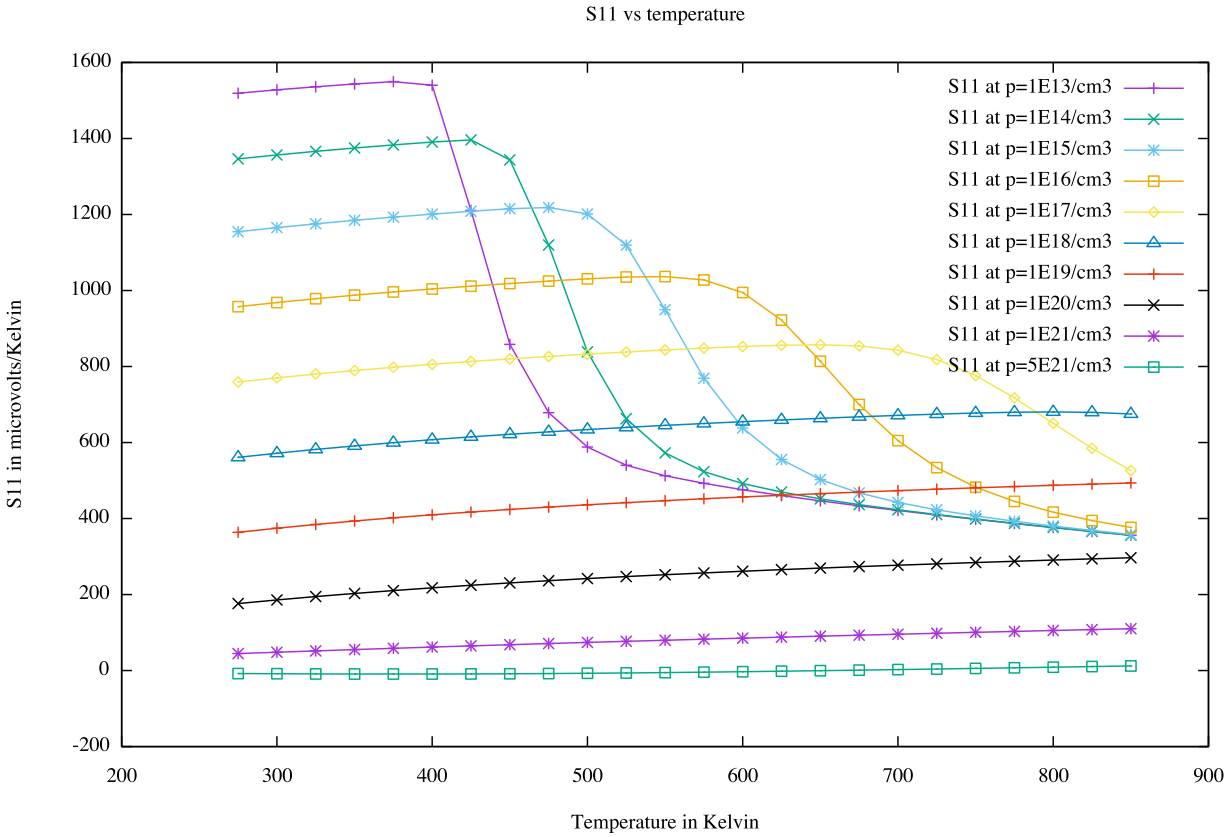

Figure 4.11. Calculated Seebeck coefficient for p-type Cu_4TiSe_4 as a function of carrier concentration and temperature.

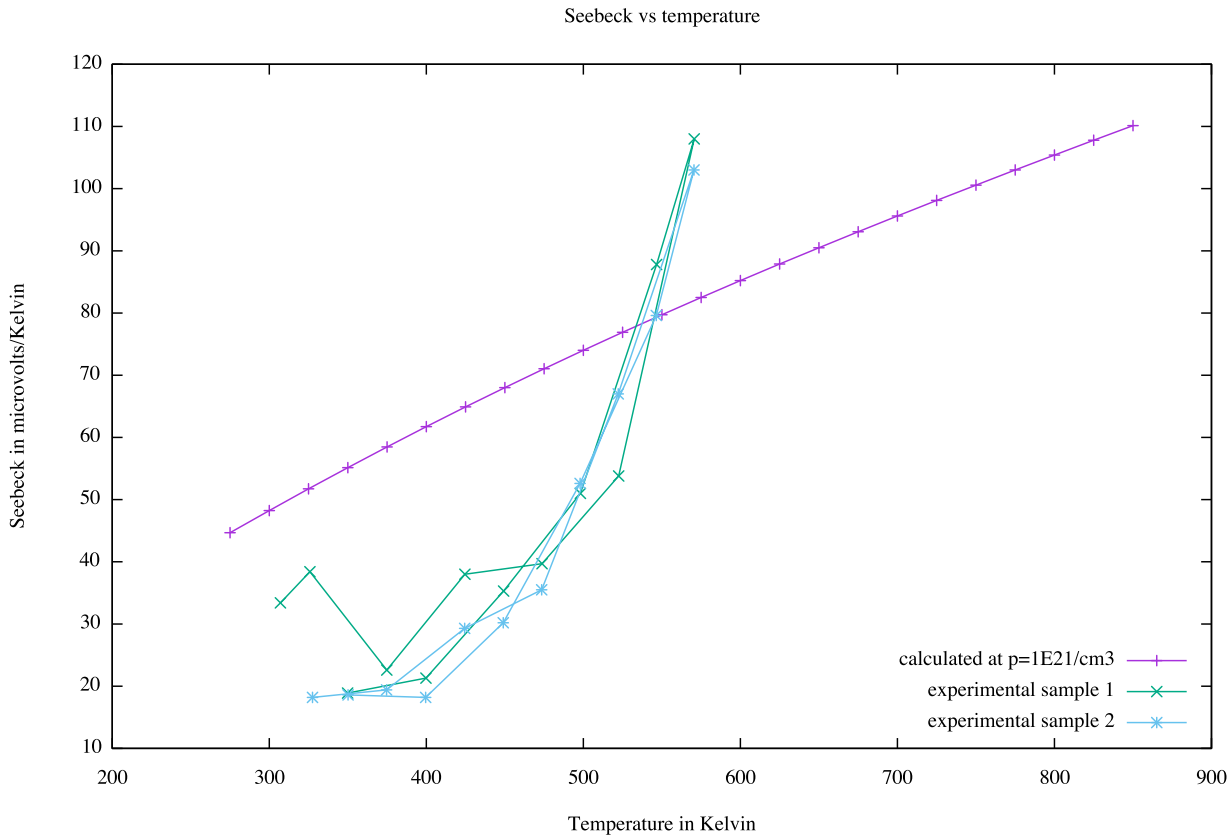

Figure 4.12. Seebeck coefficient for CTSe as calculated using p = 1x10^{21} cm^{-3} and from two experimental samples, showing rough agreement in order of magnitude.

4.8.2 Spectroscopic Limited Maximum Efficiency

The Spectroscopic Limited Maximum Efficiency (SLME)[110] is a detailed balance approach to predicting the maximum efficiency that a material can reach as a photovoltaic absorber layer. Unlike the Shockley-Queisser (SQ) limit[101], the SLME approach does not assume full absorption of light into the material above the band gap. SLME uses the material absorption coefficient to calculate phonon absorption. The absorption into the material, and thus maximum efficiency, can be calculated for different thicknesses of the absorber layer. The SLME approach also changes differs from the SQ limit in treatment of losses within the material. Instead of assuming that radiative recombination is the only loss mechanism for all materials, SLME assigns a fraction of radiative loss based on a Boltzmann equation and the energy difference

between the band gap and the lowest allowed direct gap: $f_r = e^{-(E_g^{da} - E_g)/kT}$. This is equivalent to the SQ treatment for direct, allowed gap materials and imposes a penalty upon the maximum efficiency of indirect and forbidden gap materials. This is a more accurate treatment than the SQ approximation, but is known to be overly harsh in predicting the efficiency of materials with large differences between their band gap and lowest direct allowed gap. For example, Si is predicted to be 0% efficient by SLME[111], while Si solar cells can exceed 20% efficiency. However, this allows the SLME limit to act as a low bound of expected maximum efficiency for defect-free Cu_4TiSe_4 as calculated. The increased absorption of the experimental sample at lower energies is likely due to large defect concentrations, which would prevent the material from functioning well as a photovoltaic material. Seen in Figure 4.13, due to the material's large absorption coefficient, Cu_4TiSe_4 is predicted to be more efficient than current leading photovoltaic materials at low thicknesses. At higher thicknesses, the predicted losses to nonradiative recombination mechanisms give a lower maximum efficiency compared to direct gap materials with similar band gaps.

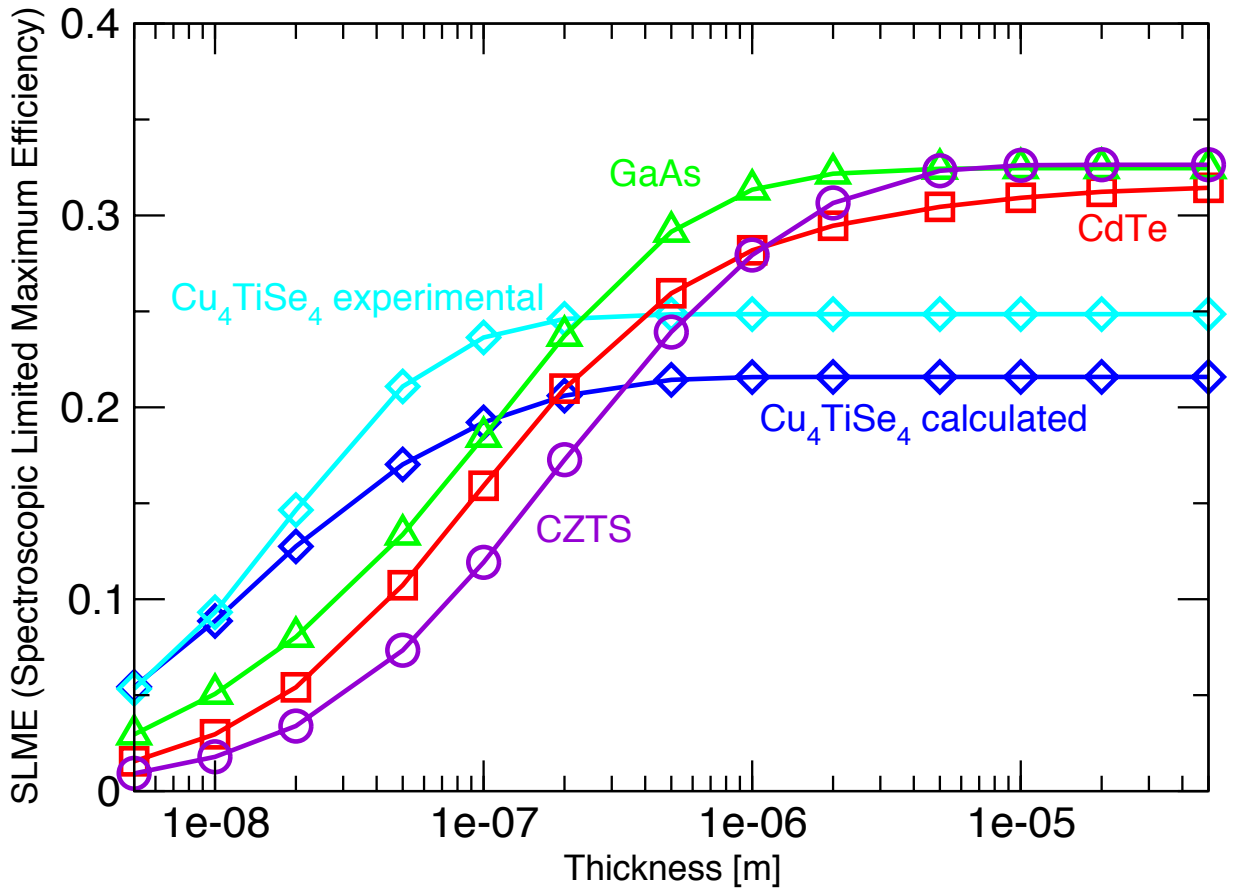

Figure 4.13. Spectroscopic Limited Maximum Efficiency (SLME) for CTSe, GaAs, CdTe, and CZTS as function of thickness. CTSe is predicted to have poorer photovoltaic performance at large thickness due to losses attributable to its indirect band gap, but higher photovoltaic efficiency at low thickness due to its superior absorption properties.

4.8.3 Properties of the cubic and tetragonal phases of Cu_4TiSe_4 and Cu_4TiS_4

Many selenide compounds have sulfur analogs with similar properties. Sulfur is also both more abundant and safer to work with than selenium, making an analogous Cu_4TiS_4 an attractive potential improvement upon Cu_4TiSe_4. Cu_4TiS_4 is known to exist in a tetragonal structure similar to a double stack of the cubic phase with a half unit cell shift of the Ti atom in the x direction. Calculation of the cubic and tetragonal phases revealed that the sulfur compounds have band gaps ~0.3 eV higher than the selenium compounds, that the tetragonal phases have band gaps ~0.9 eV larger than the cubic phases, and that the tetragonal phase is predicted to be the more thermodynamically stable phase (by ~100meV/atom) for both the sulfur and the selenide

compounds. As the cubic phase is the experimentally observed phase for Cu_4TiSe_4, the relatively instability in the calculation was surprising. Further calculations using molecular dynamics showed significant distortions of the cubic structure towards structural motifs present in the tetragonal phase. Additional work by Zihao Deng on the defect energetics in the cubic phase have shown that many copper defects are thermodynamically stable, indicating that the cubic phase is likely stabilized relative to the tetragonal phase by the presence of defects.

Table 4.4. Indirect band gaps, direct band gaps, and formation energy differences for the cubic and tetragonal phases of Cu_4TiSe_4 and Cu_4TiS_4 using the HSE06 functional. Calculations used a 4 x 4 x 4 gamma-centered k-points grid for the cubic phases and a 4 x 4 x 2 gamma-centered k-points grid for the tetragonal phases. In both compounds, the tetragonal phase is predicted to be thermodynamically more stable.

	Cubic Cu_4TiSe_4	Tetragonal Cu_4TiSe_4	Cubic Cu_4TiS_4	Tetragonal Cu_4TiS_4
Indirect band gap (eV)	1.25	2.17	1.54	2.49
Direct band gap (eV)	1.37	2.18	1.70	2.60
Formation energy difference (meV/atom)	116	0	101	0

Chapter 5 Electronic Properties of $SrHfSe_3$

This chapter is reprinted from segments of the paper listed below in which the author is the 3rd author. The author performed theoretical calculations of the band structure and the electronic density of states.

5.1 Introduction

The perovskite family of crystals has seen a great deal of research interest due to the wide compositional space they inhabit and the wide variety of properties they can display. Recently, theory predicted that compounds of the form $ABSe_3$ where A = Ca, Sr, and Ba, and B = Ti, Zr, Hf would possess band gaps in the range of 1.3-1.7 eV in the distorted perovskite phase and band gaps in the 0.75 – 1.0 eV in the needle-like (orthorhombic) phase, making them potentially useful for photovoltaic and thermoelectric devices respectively.[112]

To date, the only previously known compounds of the type $ABSe_3$ where A = Ca, Sr, and Ba, and B = Zr and Hf are $SrZrSe_3$, which was successfully synthesized as phase pure by Tranchitella et al. in 1997[113], and $BaZrSe_3$, synthesized in 1964 by Aslanov.[114,115] However, $SrZrSe_3$ crystallized in a new orthorhombic needlelike structure while $BaZrSe_3$ forms in the

‡ DOI: 10.1021/acs.inorgchem.8b01038

hexagonal $CsNiCl_3$ structure. This work reports the synthesis and properties of $SrHfSe_3$, which adopts the needle-like (orthorhombic) $SrZrSe_3$-type structure.

5.2 Methodology

5.2.1 First-Principles Calculations

DFT calculations were performed using the Vienna Ab Initio Simulation Package (VASP),[42,73–75] with projector augmented wave pseudopotentials,[71,72] including 10, 10, and 6 valence electrons for Sr, Hf, and Se, respectively. The band structure without spin−orbit coupling effects was calculated utilizing the hybrid functional of Heyd, Scuseria, and Ernzerhof (HSE06)[14,16] in conjunction with interpolation based on maximally localized Wannier functions as implemented in the wannier90 code.[95] The functional of Perdew−Burke−Ernzerhof (PBE)[7] was used to evaluate the magnitude of spin−orbit coupling. The plane wave basis set cutoff was set at 400 eV. Gamma-centered grids of 4 × 8 × 3 were used to sample the first Brillouin zone for all calculations.

5.2.2 Optical Band Gap Measurements

A Varian Cary 5000 spectrometer, equipped with a Harrick Praying Mantis diffuse reflectance accessory, was used to collect the optical diffuse reflectance spectra of the compounds over the ultraviolet, visible, and near-infrared spectral regions (UV/vis/NIR). Each sample was ground and placed in a sample holder to a depth of 3 mm. Barium sulfate (Fisher, 99.92%) was used as a 100% reflectance standard. The measurement was conducted at a scan rate of 600 nm/min. The optical band gaps of the samples were estimated from the UV/vis/NIR spectra by extrapolation of the absorption edge to the baseline. The absorption spectra were calculated from the reflectance spectra via the Kubelka−Munk equation.[116] The direct allowed

transmission model was used to fit each set of data in order to produce Tauc plots to estimate the optical band gap.

5.3 Results and Discussion

DFT calculations using the HSE06 functional were performed to investigate the band structure (Figure 5.1) and the partial density of states (PDOS) (Figure 5.3) of $SrHfSe_3$. The band structure calculated along high-symmetry directions of the first Brillouin zone shows that both the conduction band (CB) minimum and the valence band (VB) maximum are located at the Γ point, indicating that $SrHfSe_3$ is a direct gap semiconductor with a band gap of 0.88 eV (Figure 5.1). This result does not include the effects of spin orbit coupling. Calculations with the PBE functional showed that spin−orbit coupling effects on the gap are minor, narrowing the gap by approximately 50 meV. Interestingly, the band gap obtained from our calculation is similar to the value previously anticipated for the hypothetical needle-like structure of $SrHfSe_3$,[112] and is close to the experimental value of 1.02 eV obtained from diffuse reflectance measurements (Figure 5.2). Both experimental and theoretical values of the band gap are consistent with the black color of the $SrHfSe_3$ polycrystalline powder sample.

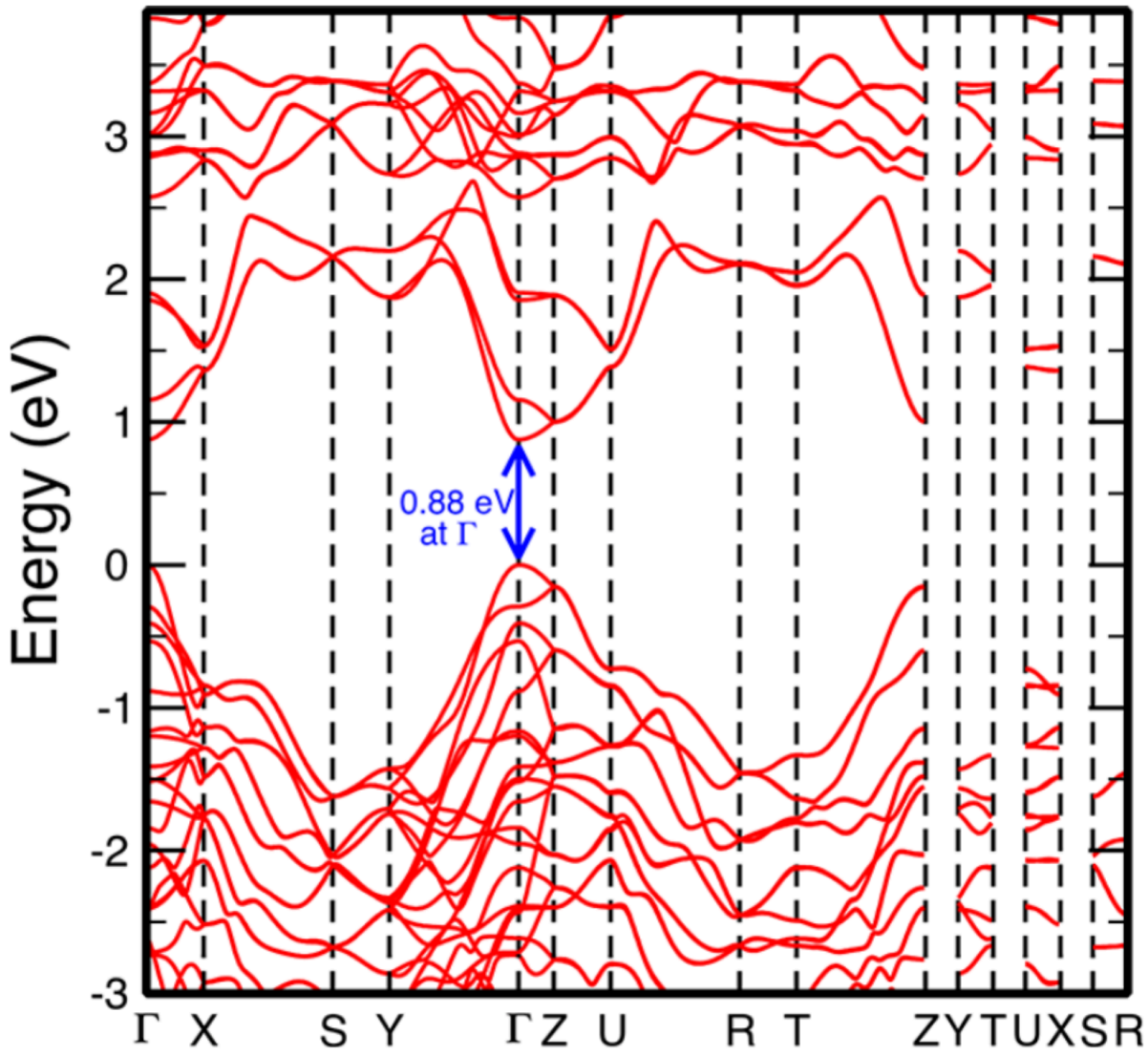

Figure 5.1. Band structure of $SrHfSe_3$ calculated using the HSE06 functional. Energies are referenced to the valence band maximum. The compound is a direct gap material with a calculated gap of 0.88 eV.

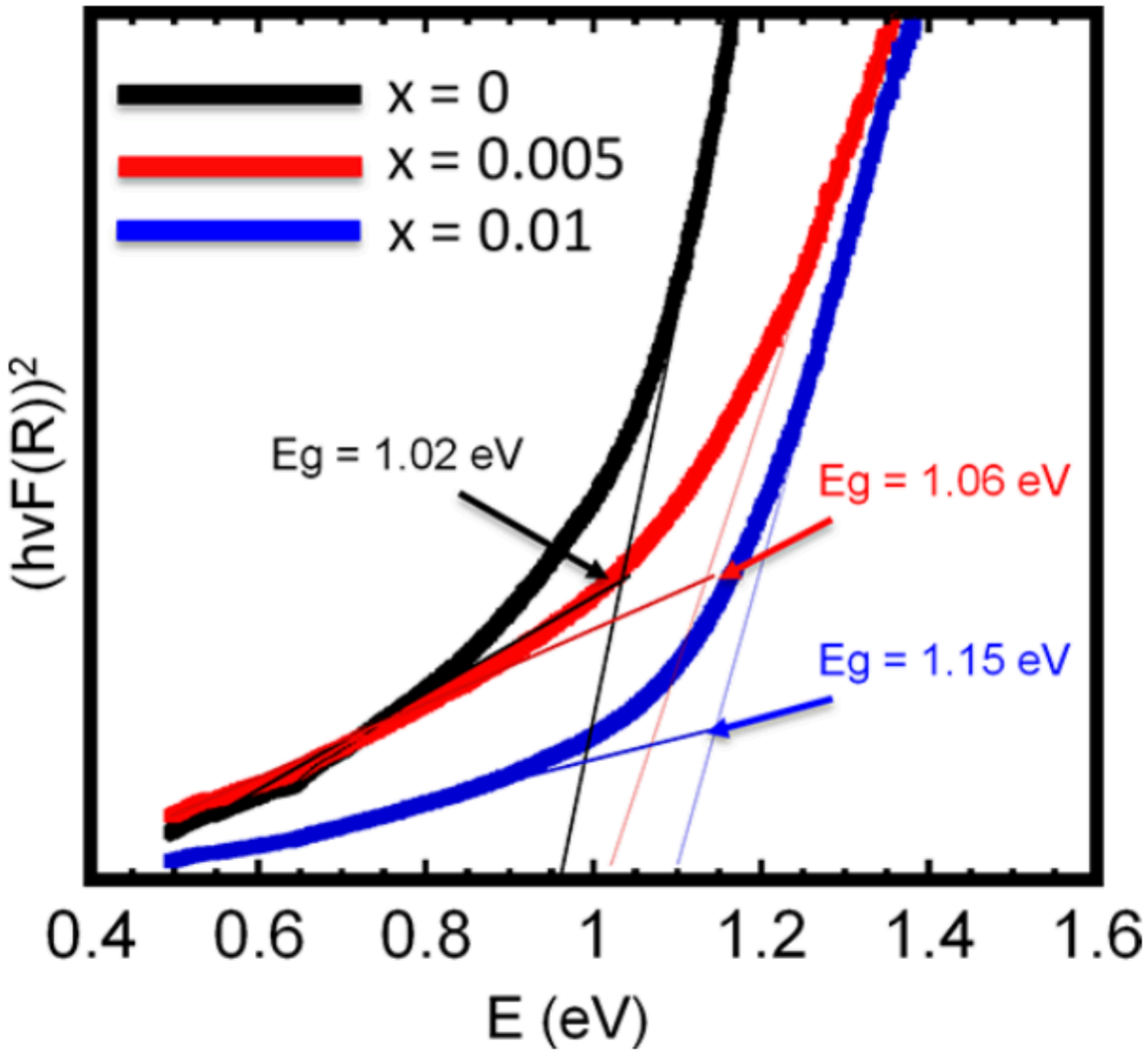

Figure 5.2. Optical band gaps of $Sr_{1-x}Sb_xHfSe_3$ showing increasing band gap with increasing Sb content.

Careful analysis of the partial densities of states (PDOS) indicates that the highest occupied valence band (or HOMO) primarily consists of Se-4p orbitals, whereas the lowest unoccupied conduction band (or LUMO) is mainly composed of Hf-5d orbitals (Figure 5.3). This implies that the optical absorption of $SrHfSe_3$ can be mainly ascribed to the promotion of carriers from the Se-4p to the Hf-5d orbitals. The valence bands between −5 and 0 eV (referenced to the HOMO) mostly consist of Se-4p orbitals, whereas the conduction bands from 0.88 to 5 eV are dominated by Hf-5d states. Therefore, the band gap in $SrHfSe_3$ is essentially determined by the

Se-4p and Hf-5d orbitals with little to no contribution from Sr atoms. Typically, band edges of p- and d-characters are a good indication of a potentially strong absorption coefficient due to the high density of states of the localized p and d orbitals. This points to a potential application of $SrHfSe_3$ as an absorbing layer in photovoltaic devices. However, significant d-character of the conduction band could result in large carrier effective masses and low carrier concentration, which can lead to low intrinsic carrier mobility and low overall electrical conductivity.

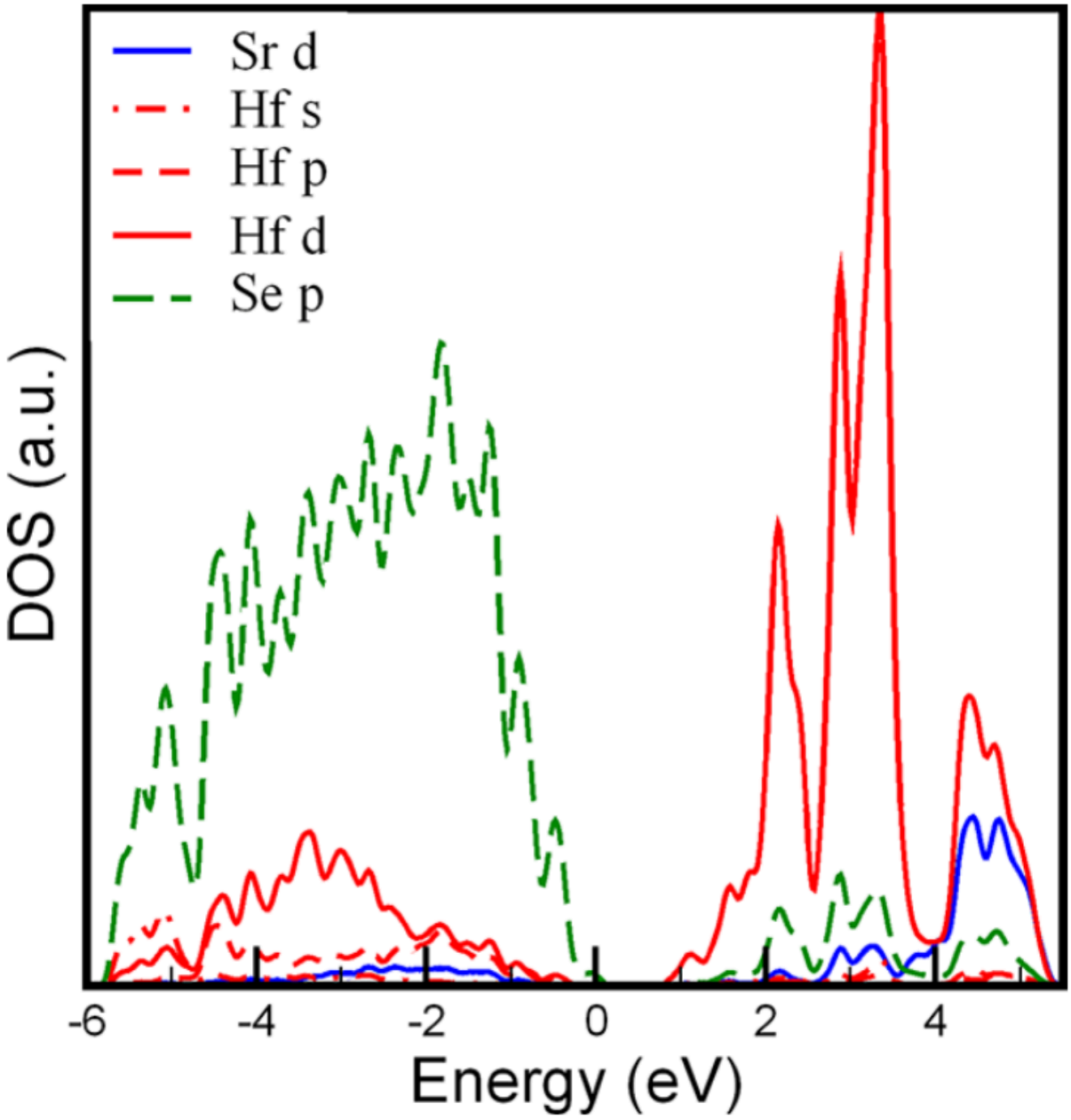

Figure 5.3. Calculated partial density of states (PDOS) of $SrHfSe_3$. The valence band has primarily Se-p character, and the conduction band has primarily Hf-d character.

Chapter 6 System Energy Modeling of (Ge, Sn, Pb)(S, Se, Te)

6.1 Introduction

High entropy alloys have attracted a great deal of research interest lately due to their often enhanced physical properties and stabilization of elements in unusual combinations and phases.[117–121] High entropy alloys are typically considered to be crystal with 5 or more primary components, and the large configurational entropy is thought to often be a critical factor in the stabilization of the single-phase solution, giving rise to the related name of entropy-stabilized materials. Most early work with high entropy alloys was performed on metals and ceramics, but other classes of materials can be designed using similar techniques.

Semiconductors designed as thermoelectric materials require high electrical conductivity simultaneously with low thermal conductivity. The scattering of phonons by disorder in an alloy is effective for greatly reducing the thermal conductivity of an alloy compared to the pure end compounds. Therefor, high entropy alloys offer a natural advantage in the development of low thermal conductivity semiconductors for thermoelectric devices. SnSe and PbTe both have high thermoelectric figures of merit above 1, and thus the group IV – VI chalcogenides are a natural system to analyze as potential thermoelectric materials.

The phase space of high entropy materials is incredibly vast due to its multi-dimensional nature. In order to make analysis of such systems more tractable, it is desirable to create a model that can represent the system built from some properties of the system's components.

6.2 Results and Discussion

As a very simple approximation, the enthalpy of mixing treated as a simple sum of the cost of all bonds in the system. For a metallic solid solution, this would mean that calculation of the mixing enthalpy of all binaries making up the high entropy system would contain sufficient information to approximate the mixing enthalpy of the high entropy system at any composition. For a cation-anion system such as (Ge, Sn, Pb)(S, Se, Te), the mixing enthalpy of all ternaries is needed. Bond counting frequency of the ternary systems, end compound binaries, and an arbitrary quinary system allows for the formula of the enthalpy of mixing of an arbitrary alloy to be related to the enthalpy of mixings of all component ternary alloys as:

$$\sum 4 * C_1 C_2 C_3 * \Delta H_{ternary,123} \tag{6.1}$$

For the (Ge, Sn, Pb)(S, Se, Te) system, there is an additional nuance of what structures to use when calculating the enthalpies of mixing. The high entropy alloy is most stable in the rocksalt phase. The component compounds exist in a variety of structures, including the Pnmb and R3mR structures. To test the model, enthalpies of mixing were calculated referenced to both the rocksalt structures only and to all the lowest energy structures for each composition. SQSs were created for all of the ternary alloys in each structure. Table 6.1 lists these ternary enthalpies of mixing. Neither version of the model performed well when tested using the comparison of SQS supercells of various high entropy compositions. Figure 6.1 shows the comparison for the lowest energy structures version of the model compared to SQS validation.

Table 6.1. Enthalpy of mixing for each ternary in the (Ge, Sn, Pb)(S, Se, Te) system calculated using either the lowest energy structures for each composition or only the rocksalt structures. The largest enthalpies of mixing exist when mixing Te and S in the same compound.

	enthalpy of mixing - lowest E [eV/cation]	enthalpy of mixing - rocksalt [eV/cation]
Ge_S_Se	0.03554	0.01659
Ge_Se_Te	0.01728	0.03123
Ge_Te_S	0.09215	0.09794
Sn_d_S_Se	0.00572	0.01203
Sn_d_Se_Te	0.02566	0.02200
Sn_d_Te_S	0.07448	0.05241
Pb_d_S_Se	0.00962	0.00962
Pb_d_Se_Te	0.02171	0.02171
Pb_d_Te_S	0.06240	0.06240
S_Ge_Sn_d	0.00804	-0.04315
S_Sn_d_Pb_d	0.02405	0.00238
S_Pb_d_Ge	0.04085	0.00981
Se_Ge_Sn_d	0.00704	0.02060
Se_Sn_d_Pb_d	0.00477	0.00111
Se_Pb_d_Ge	0.04649	0.04010
Te_Ge_Sn_d	0.02610	0.02098
Te_Sn_d_Pb_d	-0.00056	-0.00056
Te_Pb_d_Ge	0.04452	0.04066

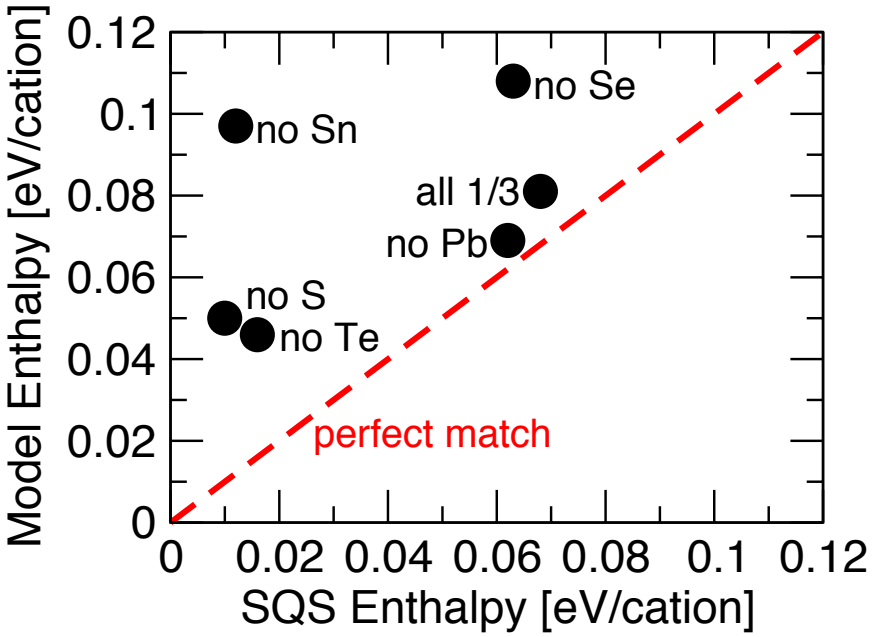

Figure 6.1. Predicted enthalpy of mixing using the model built with ternary enthalpies of mixing vs. as predicted using direct calculation of an SQS. Data shown is for using the lowest energy structure for each ternaries. The ternary mixing model is highly inaccurate.

The model was insufficient to describe the actual effects in the system. From a physical standpoint, the model assumes ideal entropy of mixing, where the maximum is reached at a 50/50 composition and has the shape of a symmetric parabolic arc, which is known to be false for many materials. From an algorithm standpoint, the model can be viewed as a very low order and short-range cluster expansion that only includes the correlations up to nearest cation-cation neighbor and nearest anion-anion neighbor clusters. There clearly exist additional terms necessary to accurately describe the system than those included in the simple model.

Chapter 7 Compositional-Structural relationships in (MgCoNiCuZn)O alloys

This chapter is an excerpt of a manuscript draft in which the author is 2nd author. The draft is by P. B. Meisenheimer, L. D. Williams, M. Trassin, E. Kioupakis, and J. T. Heron. The author performed the theoretical (DFT) work.

7.1 Introduction

Highly disordered, chemically homogeneous, single phase metallic and ceramic solid solutions have attracted significant interest in recent years due to the observation of enhanced physical properties and new emergent phases.[117–121] In high-entropy and entropy-stabilized materials, crystals with typically 5 or more species, the large configurational entropy is thought to be a critical factor in the stabilization of the phase. While this concept has been proposed in metal alloys several years ago, only recently has it been extended to ceramics where the configurational entropy is created by chemically disordering the cation sublattice.[122–124] Particularly for oxides, pioneering experimental work has demonstrated the emergence of a homogenous single phase at a critical entropy and that the critical temperature varies with the configurational entropy.[124] These, so-called, entropy-stabilized oxides (ESOs) enable an unprecedented new degree of chemical control in materials, as the technique can be used to incorporate typically immiscible concentrations of cationic species in an atypical coordination. As the properties of oxides are strongly correlated to their stereochemistry and electronic structure,[125–128] ESOs thus present the opportunity to tune charge,[129] lattice,[130–132] and spin[133] disorders to new extremes in a single-phase, single-crystalline material. In fact, remarkable

properties such as glass-like thermal conductivity[129] and colossal physical properties[133–135] have been observed, yet the contributions of disorder in structure and chemistry to these properties, along with their interplay and tunability, remains to be uncovered.

In a conventional binary rock salt oxide, such as MgO, NiO, or CoO, the cation species sit on octahedrally-coordinated sites. The (MgCoNiCuZn)O-type rock salt ESOs studied here, however, are expected to deviate from this ideal configuration due to the presence of disordering species. Specifically, Cu^{2+} cations will tend to undergo a tetragonal distortion from an octahedral configuration in order to break the e_g orbital degeneracy present in a d^9 system (i.e. the Jahn-Teller (JT) effect). In (MgCoNiCuZn)O, however, a fraction of the Cu^{2+} cations are forced into the rock salt structure, in competition with the JT effect, leading to a frustration of the atomic positions around the site. This competition is expected to significantly impact the functional properties and disorder.[133] Here we find that the crystalline lattice of (MgCoNiCuZn)O ESO thin films is structurally distorted by this stereochemical frustration.

We investigated copper variant $(Mg_{0.25(1-x)}Co_{0.25(1-x)}Ni_{0.25(1-x)}Cu_xZn_{0.25(1-x)})O$ (x = 0.11, 0.17, 0.20, 0.24, 0.27) and cobalt variant $(Mg_{0.25(1-x)}Co_xNi_{0.25(1-x)}Cu_{0.25(1-x)}Zn_{0.25(1-x)})O$ (x = 0.20, 0.27, 0.33) ESO thin films to probe the interplay of chemical and structural disorder on magnetic order. These compositions were chosen systematically because Cu^{2+} cations will tend to distort the octahedral site, creating a mechanism of structural disorder. Because these active sites are spread across the crystal in large concentrations (1/5 of cation sites in an equimolar, 5-component ESO), we hypothesize that this will create a concerted effect and drive structural frustrations across the whole system.[136,137] In contrast, Co^{2+} prefers octahedral coordination, minimizing structural disorder, and changes the average magnetic moment significantly (~1.6 to

1.9 μ_B cation^{-1}).[133] $(Mg_{0.2}Co_{0.2}Ni_{0.2}Cu_{0.2}Zn_{0.2})O$ was previously shown to not only be antiferromagnetic (AFM), but have a large ferromagnetic (FM)/AFM exchange coupling.[133]

7.2 Tuning of Structural Disorder

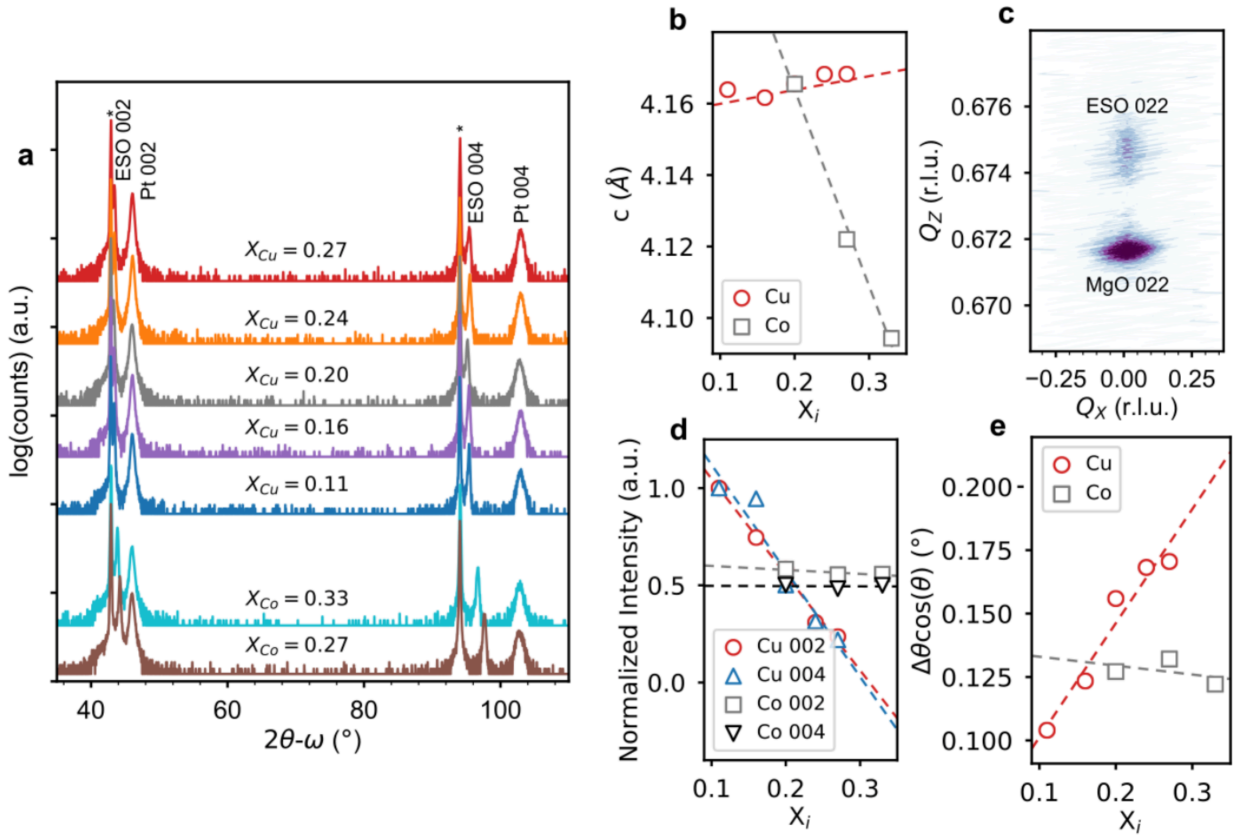

Figure 7.1. Control of structural disorder through stereochemical frustration. a) 2θ – ω XRD spectra of Cu and Co variant ESO thin films. Only the 002 and 004 peaks from the ESO film are present, showing phase purity and epitaxy. * indicates MgO 002 and 004 substrate peaks. b) Out-of-plane lattice constants of the Cu variant and Co variant ESO films determined using Cohen's method. c) Reciprocal space map of equimolar, X = 0.20, ESO, showing the film is clamped to the substrate in the Q_X direction (in-plane). d) Normalized peak intensities of the ESO 002 and 004 peaks, showing a decrease in the peak intensity with increasing Cu. e) Full-width at half-max (Δθ) of the 002 peaks in a), deconvolved with peak position, showing a significant increase in the peak width with increasing Cu concentration and a small decrease with Co composition.

In the typical Jahn-Teller distortion of Cu^{2+}, the axial bond will elongate and the basal bonds will contract in order to break the octahedral symmetry and remove the degeneracy of the unpaired electron in the e_g orbital.[136] This, naturally, gives rise to a bimodal distribution of bond lengths and a tetragonal distortion of the cation site. From our XRD spectra, we observe this structural distortion as a function of Cu composition. The peak intensities of the 002 and 004

film diffraction peaks, normalized to the substrate peak intensity and then scaled, show a linear decrease with increasing concentration of Cu (Figure 7.1**d**), consistent with an increasing tetragonal or monoclinic distortion of the lattice that breaks symmetry about the 002 peak.[136,137] Additionally, the peak width increases with the concentration of Cu (Figure 7.1**e**), implying a large degree of correlated disorder in the system.[138] In contrast, the relative intensity and peak widths of the 002 peaks for the Co variant films remain invariant (Figure 7.1**d and e**). From this, we are able to directly tie and tune the degree of global structural disorder in the material to the concentration of the Jahn-Teller species.

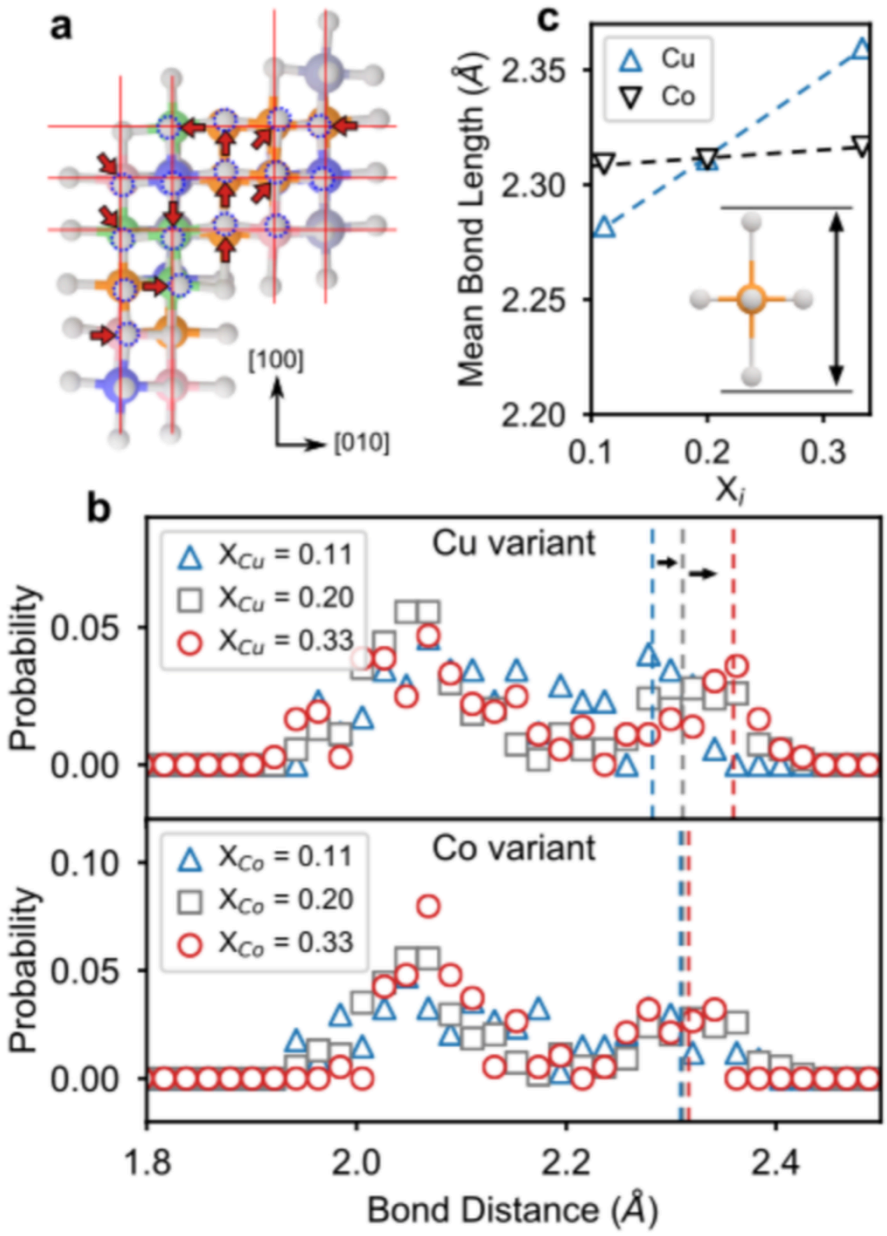

Figure 7.2. Simulated bond length disorder in compositionally variant ESOs. a) 94-atom supercell of Cu-rich ESO relaxed using DFT. Ideal planes of atoms are overlain in red, highlighting the structural distortions (emphasized by arrows) most clearly on the oxygen anion sites (shown in grey). The Cu cations are shown in orange. b) Histograms of bond lengths on the Cu-cation sites for $X_{Cu, Co}$ = 0.11, 0.20, 0.33 ESOs, demonstrating the characteristic double peak of a Jahn-Teller distorted cation. c) Axial bond length of the Cu site in Cu variant (Cu) and Co variant (Co) ESO. As the concentration of Cu is increased in the material, we observe an increase in the length of the z (extended)-axis on the Cu cation site, implying that the degree of distortion is sensitive to the local environment about the Cu site and the total concentration of Cu.

From density functional theory (DFT) calculations of our Cu variant ESOs, we can observe this structural distortion on an atomic scale. The relaxed atomic coordinates (Figure 7.2**a)** show a large spatial deviation from the perfect rock salt structure. The histogram of the

bond lengths in our simulated ESO supercells exhibits the characteristic bimodal distribution of the Jahn-Teller effect (Figure 7.2**b**). Interestingly, we also observe a shift in the peak length of the extended axial bond with increasing concentration of Cu (Figure 7.2**b** and **c**). In the case of varying Co concentration, the peak-length shift is negligible. This shows that Cu is responsible for the structural distortion, and that the intensities of the Cu-site distortions are sensitive to the local environment, specifically the presence of many nearest-neighbor Cu cations. Additionally, our analysis demonstrates that the disorder-driving sites are working in a concerted manner, agreeing with our observation in Figure 7.1 of a concerted symmetry breaking.

Further, our first-principles calculations of the structures for the Cu and Co variant ESOs also show a significant variation in bond angle (up to nearly 20°) that is correlated to increasing Cu incorporation (Figure 7.3). As the concentration of Cu in the supercell is increased, the variance of the bond angle distribution increases sharply, by 10x over the relatively small compositional space. This linear trend also agrees with the compositional disorder observed in our XRD measurement from the FWHM of the film diffraction peaks[138] (Figure 7.1**e**).

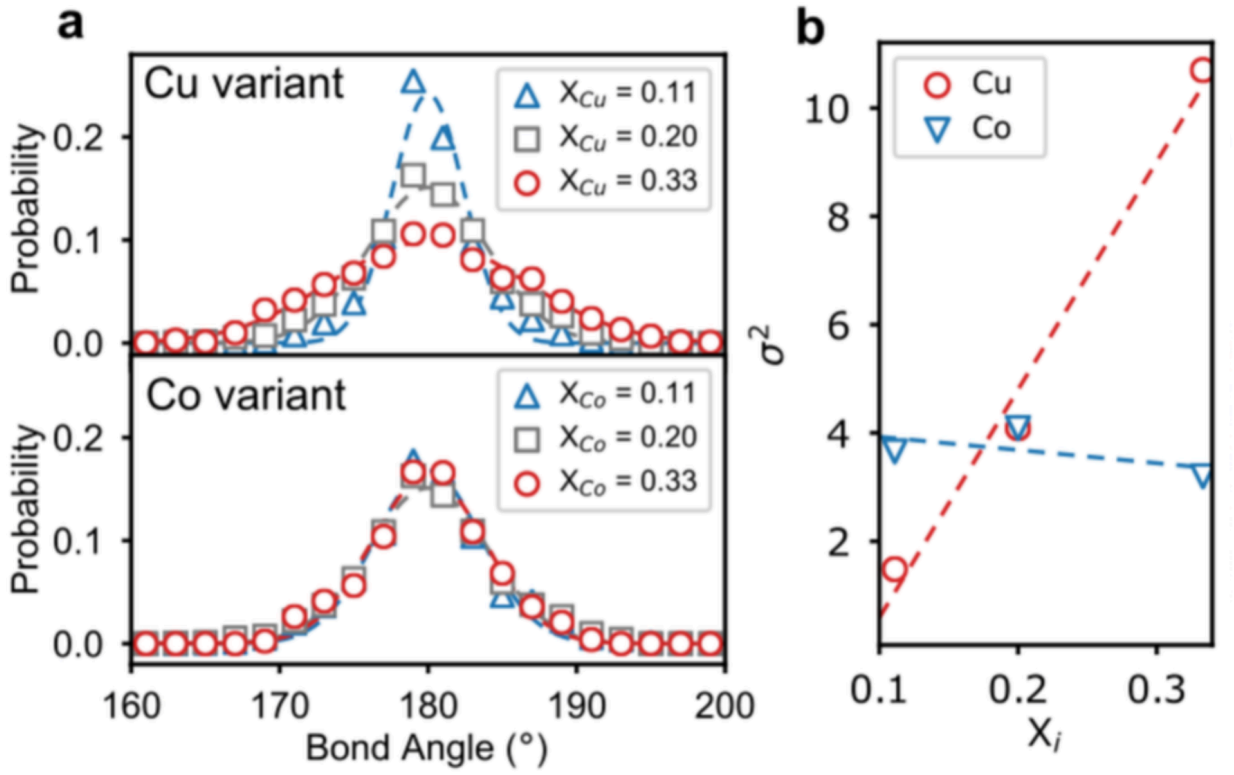

Figure 7.3. Bond angle disorder in compositionally variant thin film ESOs. a) Histogram of cation-anion-cation bond angles for Cu variant ESO calculated from DFT. b) Variance (σ^2) of the Gaussian fits to the data in a). As the concentration of Cu cations is increased, the variance of the calculated bond angle changes significantly.

7.3 Conclusion

In conclusion, we have demonstrated that the variation of the copper concentration can control the structural order in this entropy-stabilized oxide system. This is combined with experimental measurements in the full manuscript to show that composition-based structural order tuning can be used to control the degree of magnetic ordering in the alloy.

Chapter 8 Wurtzite $(B_2In_3)_xGa_{1-x}N$ alloys

This chapter is reprinted from the paper listed below in which the author was the primary author.

Reprinted from Appl. Phys. Lett. **111**, 211107 (2017), with the permission of AIP Publishing.[§]

8.1 Introduction

InGaN light-emitting diodes (LEDs) with an electricity-to-light conversion efficiency of ~39% provide large efficiency gains and cost reductions compared to incandescent and fluorescent light sources.[139] However, InGaN LEDs suffer from decreasing internal quantum efficiency at high currents (efficiency droop), particularly at longer wavelengths (green gap). The cause of the droop has been extensively studied, with Auger recombination identified as a major loss mechanism.[140] For equal electron and hole densities, the Auger recombination rate is equal to the carrier density cubed times a material-dependent Auger coefficient C. Since the Auger coefficient is an intrinsic property of InGaN that does not depend strongly on composition, temperature, or strain,[141] the carrier density at a given current density must be lowered to reduce the Auger losses.

Increasing the active-region volume is a straightforward approach to reduce the carrier density and hence the Auger loss, yet growth challenges limit its practicality. Devices using a

---

[§] DOI: 10.1063/1.4997601

single thick InGaN layer exhibit higher high-power efficiency than thinner quantum wells both for polar[142] and for semipolar[143] growth orientations. The thickness of InGaN active layers is however limited by the lattice mismatch with the underlying GaN layers, and the subsequent appearance of performance-degrading dislocations. On the other hand, the efficiency of multiple-quantum-well (MQW) structures is lower than a single InGaN layer of the same total active thickness[143] since hole injection is poor and only the first few QWs near the p-layer in a MQW structure emit light.[144,145]

The co-alloying of InGaN with wurtzite boron nitride (w-BN) can produce BInGaN alloys lattice-matched to GaN with gaps spanning the visible range (Fig. 8.1). Co-alloying has been demonstrated in, e.g., GaAsPBi[146] and GaAsNBi,[147] in which the co-incorporation of P (N) and Bi atoms yields alloys lattice-matched to GaAs with a reduced band gap. Under ambient conditions, BN adopts the hexagonal layered structure that can be exfoliated to form 2D materials. Wurtzite BN is a high-pressure polytype with the same crystal structure as InGaN. For low BN content, alloys of BN with InGaN are expected to also adopt the wurtzite structure to minimize dangling-bond formation. Moreover, although w-BN is an indirect-gap semiconductor, the gap of BInGaN is determined by the lower gap of the InGaN component, which is direct. The in-plane lattice constant of BInGaN is approximated, to first order, by Vegard's law. Based on the experimental in-plane lattice constants of GaN (3.181 Å), InN (3.538 Å) and w-BN (2.536 Å),[148–150] the optimal B mole fraction to lattice-match $B_yIn_{1-y}N$ to GaN is $y=0.356\approx0.4$. Therefore, an approximate ratio of B:In≈2:3 is expected to yield BInGaN alloys nearly-lattice-matched to GaN. Hence, varying the Ga mole fraction while keeping the B:In ratio constant is a promising method to tune the gap of BInGaN while keeping the in-plane lattice constant nearly matched to GaN.

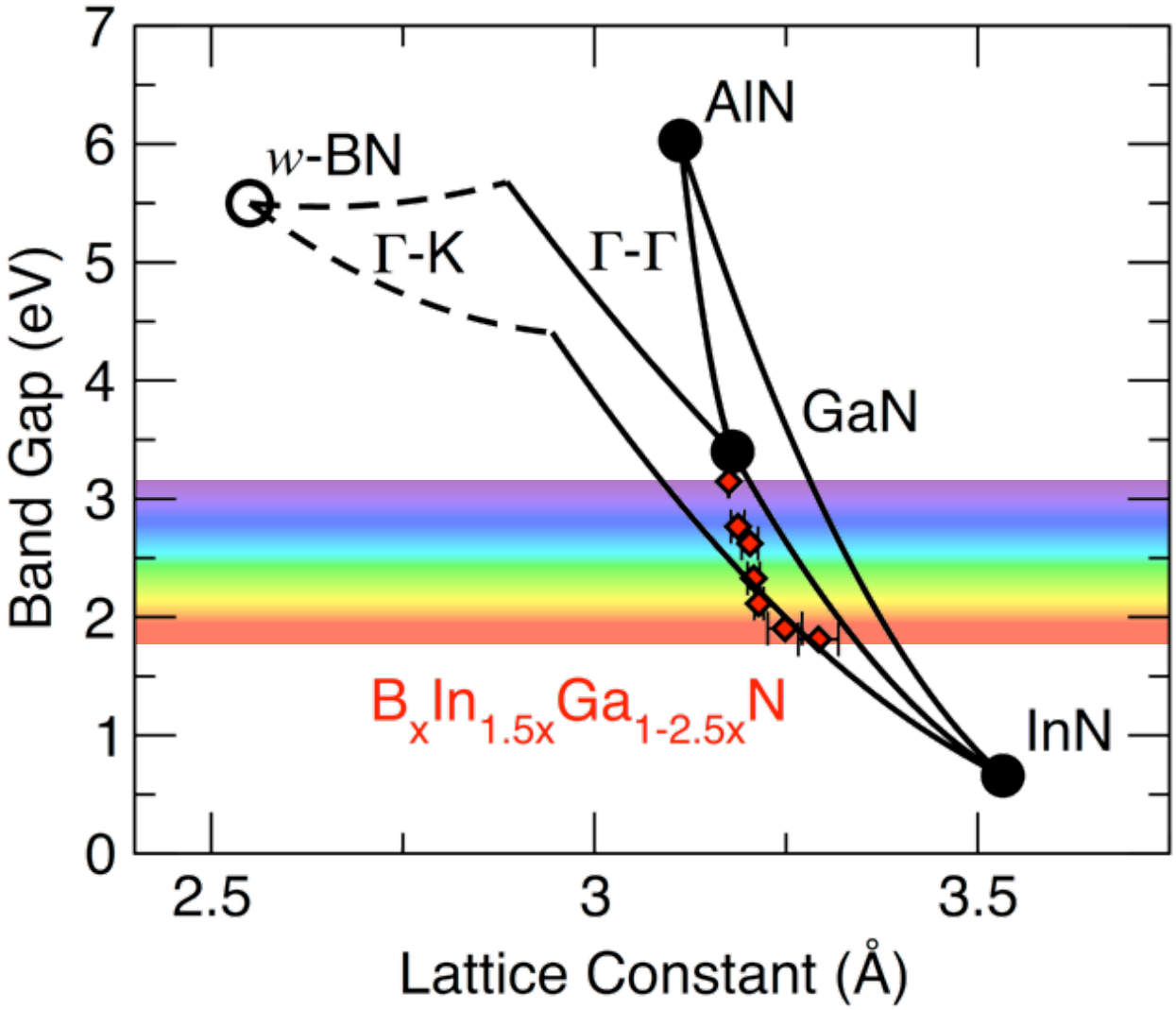

Figure 8.1. Band gaps vs. in-plane lattice constant (a) for wurtzite group-III nitrides. The $B_xIn_{1.5x}Ga_{1-2.5x}N$ alloys investigated in this work (red diamonds) maintain approximate lattice match to GaN while their gaps span the entire visible range. The error bars show the uncertainty in the lattice constant (See Figure 8.3). Closed circles and full lines represent the direct gap materials. Open circles and dashed lines represent the indirect gap materials.

Previous experimental and theoretical studies have explored the structural and electronic properties of B-containing GaN, InN, and InGaN. Ougazzaden et al. grew BGaN thin films with up to 3.6% boron.[151] They reported lower gaps than GaN and a large bowing parameter.[152] Kadys et al. used metal-organic chemical vapor deposition (MOCVD) to grow up to 2.9, 4.3, and 5.5% boron BGaN on GaN, AlN, and SiC substrates respectively.[153] Cramer et al. reported high-crystal-quality BGaN with up to 3% boron grown with plasma-assisted molecular beam epitaxy and observed statistically random atomic distributions.[154] Gunning et al. grew up to 7.4% boron

BGaN on AlN using metalorganic vapor phase epitaxy (MOVPE) at low temperatures and pressure (750-900 °C and 20 Torr), but reported severe structural degradation and a shift to a twinned cubic structure at higher boron concentrations.[155] Approximately equimolar nanocolumnar BInN has also been synthesized with a reported gap of 3.75 eV.[156] Quaternary BInGaN has been grown on GaN/sapphire and ZnO-buffered Si substrates with MOVPE by Gautier, Ougazzaden, et al.[157,158] They reported smaller lattice constants and gaps than GaN for up to 2% B and up to 14% In content.[157,158] The extracted bowing parameters were applied to predict the gap for a broader composition range. However, their InGaN bowing parameter is larger than subsequent predictive calculations,[159] while the BN gap was set to the indirect Γ-K value instead of the larger direct Γ-Γ one.[151,152,160] McLaurin also reported the growth of BInGaN.[161] Theoretically, Park and Ahn examined BInGaN/GaN quantum wells with effective mass theory. They reported a lower mismatch to GaN than InGaN, and a reduction of the polarization fields.[162] Assali et al. examined ordered BInGaN in the metastable zinc blende phase with density functional theory (DFT). They found a near-lattice-match to GaN for a composition with the same 2:3 B:In ratio as our estimate, and a small increase of the gap (0.1-0.3 eV) compared to InGaN of the same In content.[163] However, they did not examine the thermodynamically stable wurtzite phase, which has a larger gap than zinc blende,[164] and did not account for disorder. Overall, the properties of GaN-lattice-matched disordered wurtzite BInGaN alloys over their full composition range and their potential for reducing the LED droop problems remain unexplored.

8.2 Methodology

In this work, we explore the thermodynamic, structural, and electronic properties of statistically random quaternary wurtzite BInGaN alloys with hybrid-functional DFT. BInGaN

alloys with a B:In ratio of 2:3 are better lattice mismatch to GaN than InGaN. Co-alloying with In lowers the enthalpy of mixing and facilitates higher B incorporation. Our results show that BInGaN alloys can be designed nearly-lattice-matched to GaN with a direct band gap adjustable over the entire visible range, and are therefore promising active-layer materials to overcome the efficiency-droop and green-gap problems of nitride LEDs.

We performed DFT calculations based on the projector augmented wave (PAW) method[71,72] using the Vienna Ab initio Simulation Package (VASP).[42,73–75] The GW-compatible pseudopotentials including 3, 13, 13, and 5 valence electrons were employed for B, In, Ga, and N, respectively, with a 600 eV plane-wave cutoff. Structural relaxations were performed using the optB86b-vdW functional[165] and a Γ-centered Wisesa-McGill-Mueller Brillouin-zone grid with a minimum period distance of 21.48 Å.[166] Forces on atoms were relaxed to 1 meV/Å. Band-gap calculations were performed with the Heyd–Scuseria–Ernzerhof (HSE06) functional.[14,16] Random alloys were modeled using Special Quasi-random Structures (SQS) generated with the Alloy Theoretic Automated Toolkit[18] and a 3×3×2 wurtzite supercell. Cations were arranged to approximate the pair-correlation functions of random alloys up to 5.125 Å. Five SQSs were generated at each composition and relaxed to obtain structural parameters. The SQSs that most closely match random pair-correlation functions at each composition were used for electronic and thermodynamic calculations (Fig. 8.7). The projected density of states (pDOS) was calculated using the optB86b-vdW functional and a Γ-centered 8×8×8 Brillouin-zone grid, and the gap was rigidly shifted to the HSE06 value.

8.3 Results and Discussion

Our thermodynamic analysis reveals that the solubility of B into InGaN is higher than into GaN. To calculate the transition temperature between the solid-solution and the miscibility-

gap regimes as a function of composition, $T(x)=\Delta H(x)/S$, we evaluated the enthalpy of mixing as a function of alloy composition, $\Delta H(x)$, by subtracting the total energy of ternary and quaternary alloys from the linear combination of the binaries. The entropy was evaluated using the regular solution model, , $S = -k_B \sum_{i=1}^{N} x_i \ln x_i$ (x_i is the mole fraction for each of the N alloy ingredients, and k_B is Boltzmann's constant. The transition temperatures (Fig. 8.2) for $B_xIn_{1.5x}Ga_{1-2.5x}N$, $B_xGa_{1-x}N$, and $In_{1.5x}Ga_{1-1.5x}N$ are well above typical growth temperatures for x > 0.05, which is expected since nitrides are typically grown with epitaxial techniques (e.g., MOCVD or molecular beam epitaxy) that take place far from thermodynamic equilibrium. However, the relative equilibrium phase boundaries can be combined with experimental literature data to predict the limits of boron incorporation into InGaN. For boron mole fractions less than 0.2, the temperature needed to dissolve B into InGaN is approximately 2/3 of the temperature needed to dissolve it into GaN. The increased solubility of B into InGaN is due partly to the increased configurational entropy in the quaternary alloy, and partly to the partial cancellation of local stress by the opposite size mismatch between the smaller B and the larger In atoms. We therefore estimate that 1.5× as much boron can be incorporated into InGaN compared to GaN. Since high-quality, single-phase $B_xGa_{1-x}N$ alloys with boron concentration up to x=0.03 have already been demonstrated,[154] we anticipate that up to ~4.5% boron incorporation should be possible in BInGaN with existing growth approaches.

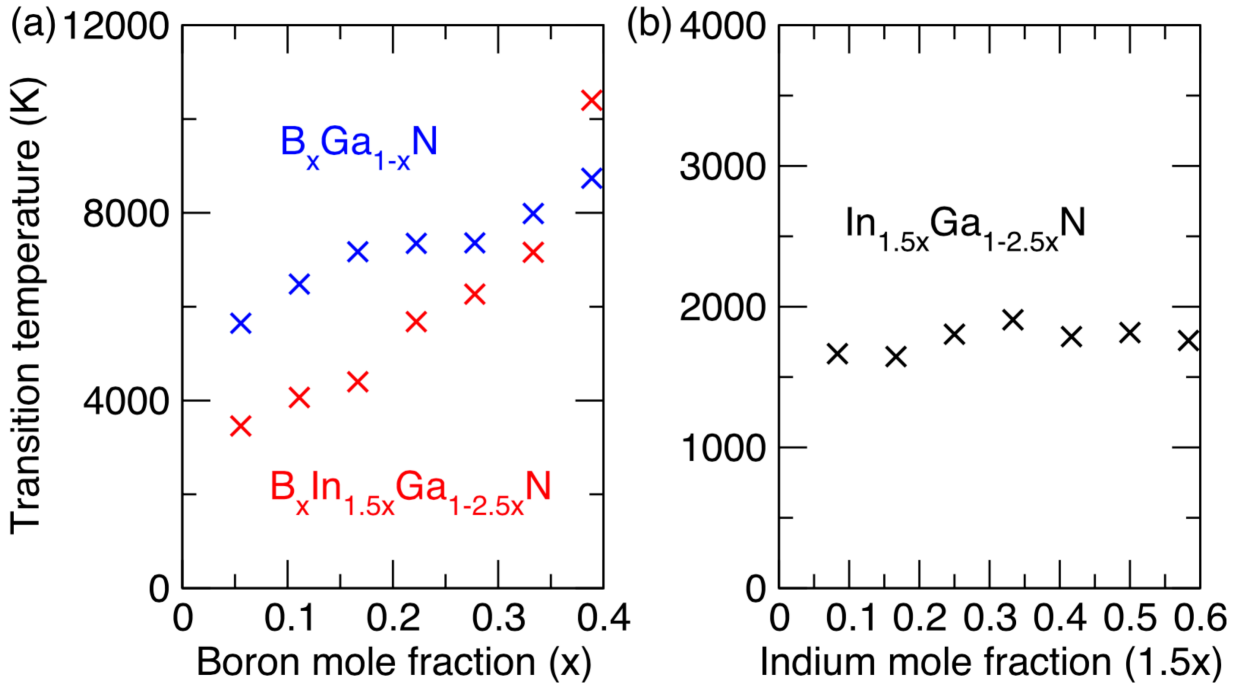

Figure 8.2. Calculated transition temperature for the thermodynamic equilibrium random mixing of group III nitride alloys. (a) $B_xIn_{1.5x}Ga_{1-2.5x}N$ and $B_xGa_{1-x}N$ as a function of Boron mole fraction. (b) $In_{1.5x}Ga_{1-1.5x}N$ as a function of Indium mole fraction. The transition temperatures of $B_xIn_{1.5x}Ga_{1-2.5x}N$ are approximately 2/3 that of $B_xGa_{1-x}N$ of equal B mole fraction at low boron concentrations (<0.2), indicating that boron is more easily incorporated into InGaN than into GaN.

Our calculations verify that BInGaN with a 2:3 B:In ratio is better lattice-matched to GaN substrates than InGaN and can therefore be grown to larger thicknesses. Figure 8.3 shows the calculated configurationally averaged *a* and *c* lattice constants of $B_xIn_{1.5x}Ga_{1-2.5x}N$ relative to GaN. The trend for *a* is not described well by a straight line, and therefore deviates from Vegard's law, agreeing with previous calculations for BGaN.[167] Instead, it follows a bowing relationship, $a_{\mathrm{BInGaN}}(x)/a_{\mathrm{GaN}} = a_1 x + a_2(1-x) - bx(1-x)$, where $a_1 = 1.034$, $a_2 = 1$, and $b = 0.052$. The a lattice-constant mismatch of BInGaN is smaller than +/–0.25% for indium fractions under 0.2 (Fig. 8.3(a)), which facilitates growth on the *c*-plane of GaN. Due to the bowing, the mismatch of $B_{0.045}In_{0.0675}Ga_{0.8875}N$ to GaN is predicted to be only *–0.1%*. The *c* lattice constant of BInGaN (Fig. 8.3(b)) remains near the GaN value.

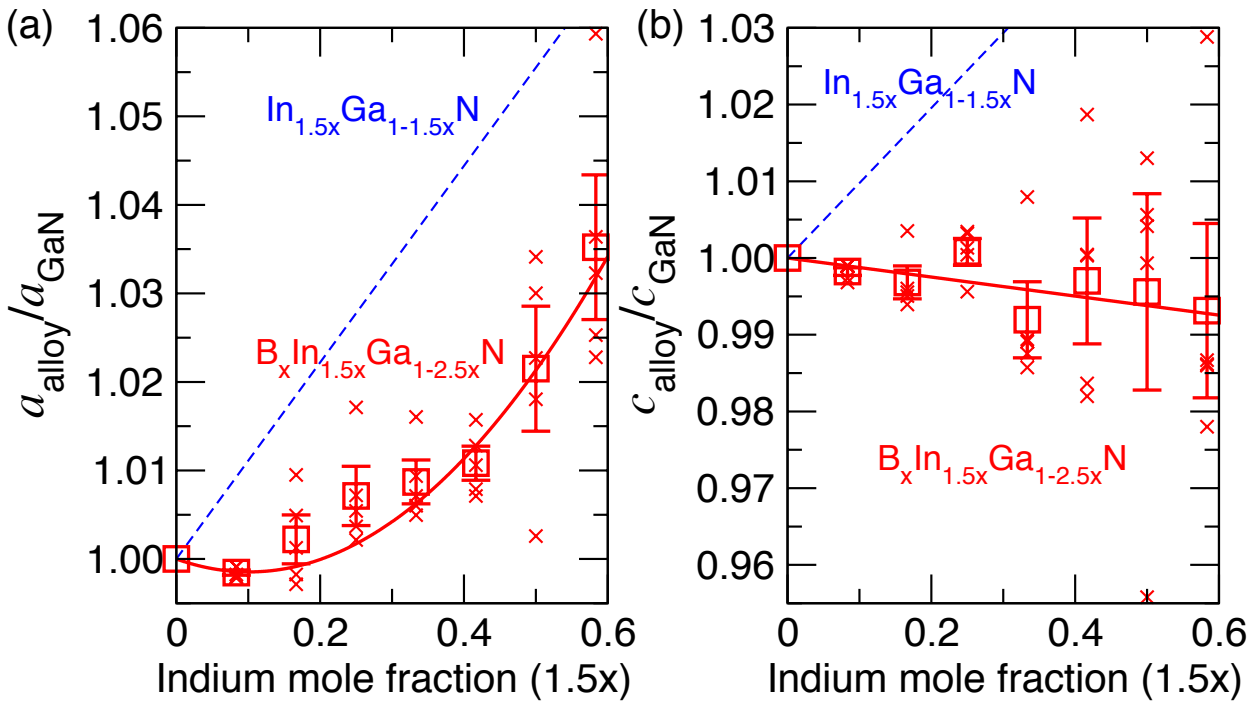

Figure 8.3. The calculated lattice constants of InGaN and BInGaN alloys relative to GaN along (a) the a direction and (b) the c direction. Both the values for each configuration (crosses) and the configurational average (squares) are displayed. The *a* lattice constant data are fit to a bowing equation and have a bowing parameter of 0.052. The error bars show the statistical uncertainty for each configurational average, calculated as half of the range divided by the square root of the number of samples. The mismatch of $B_xIn_{1.5x}Ga_{1-2.5x}N$ to GaN along the *a* axis is significantly reduced compared to an equivalent $In_{1.5x}Ga_{1-1.5x}N$ alloy, especially at lower boron and indium concentrations, while BInGaN is approximately lattice matched to GaN along the *c* direction.

Our band-gap calculations demonstrate that $B_xIn_{1.5x}Ga_{1-2.5x}N$ has a tunable direct gap that spans the entire visible range. In contrast to BGaN, which transitions from direct to indirect gap for increasing B content,[168] the gap of BInGaN remains direct throughout the entire explored composition range. Figure 4 shows the calculated gap of $B_xIn_{1.5x}Ga_{1-2.5x}N$, $B_xGa_{1-x}N$, and $In_{1.5x}Ga_{1-1.5x}N$ as a function of composition. For the 2:3 B:In ratio, the gap ranges from 3.14 to 1.50 eV for decreasing Ga content. Increasing our calculated values by 0.25 eV to match the room-temperature gap of GaN (3.39 eV)[169] brings our BInGaN gap estimate to the 3.39–1.75 eV range, spanning the entire visible spectrum. The gap of $B_xIn_{1.5x}Ga_{1-2.5x}N$ is also approximately equal to that of $In_{1.5x}Ga_{1-1.5x}N$ for the same In mole fraction. To explore this behavior, we determined the orbital character of the conduction and valence band edges. The pDOS of

$B_{0.278}In_{0.417}Ga_{0.306}N$, calculated with the optB86b-vdW functional, (Fig. 8.5; comparison to the HSE pDOS in Fig. 8.8) shows that the edge states consist primarily of N and In orbitals, while B states lie higher in the conduction band. Similar to InGaN, the valence-band edge consists primarily of localized N 2*p* states, except in BInGaN the states reside near planarized B atoms (Fig. 8.5 inset). The hole localization energy ranges from 0.1-0.4 eV as the boron content ranges from 15-40%, the maximum value occurring for $B_{0.278}In_{0.417}Ga_{0.306}N$ (Fig. 8.6). Localized states were not observed for boron mole fractions lower than 15%. The conduction-band edge is primarily formed by N 2*p*, N 2*s*, and In 5*s* states. Our calculations therefore show that partial substitution of B for Ga in InGaN has only minor effects on the gap and edge states.

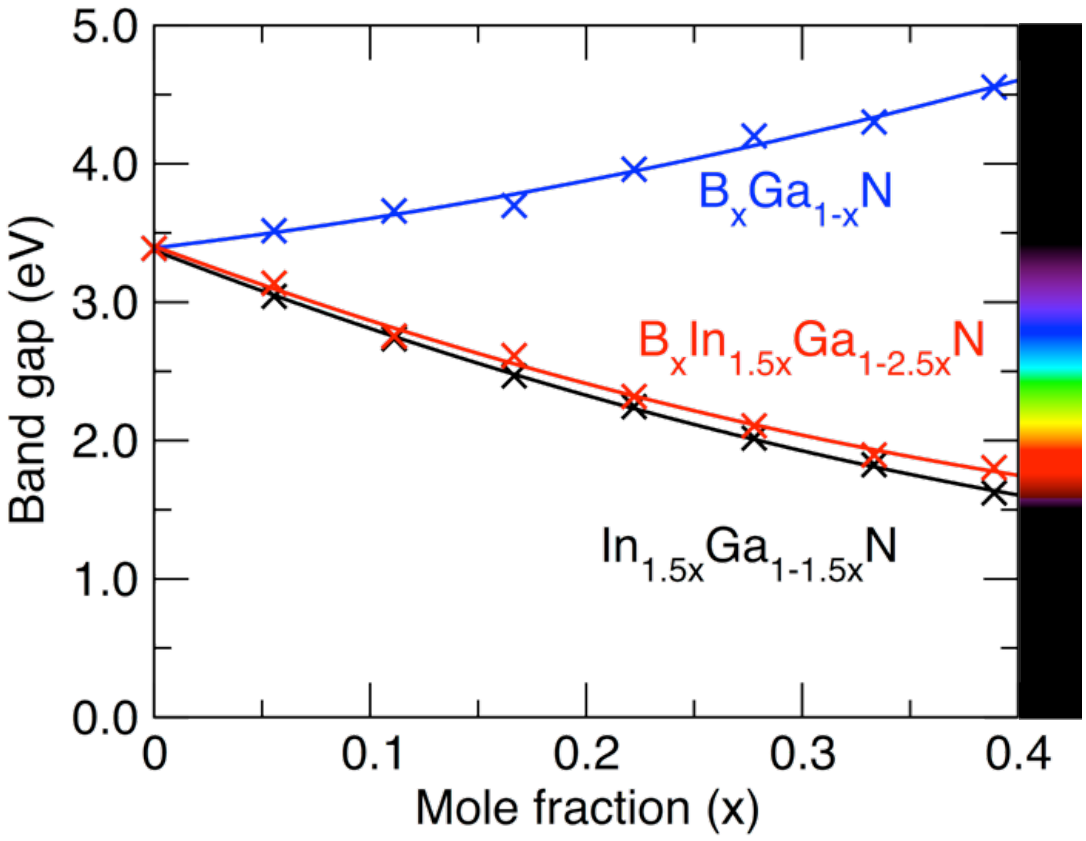

Figure 8.4. The calculated band gaps of $B_xIn_{1.5x}Ga_{1-2.5x}N$, $In_{1.5x}Ga_{1-1.5x}N$, and $B_xGa_{1-x}N$ as a function of mole fraction x. The calculated gap values have been increased by 0.25 eV to match the experimental gap of GaN at room temperature (3.39 eV).[169] The band gap of BInGaN alloys spans the entire visible range. The gap of BInGaN has approximately the same value as an InGaN alloy of the same indium mole fraction, indicating that boron incorporation has a negligible effect on the gap of InGaN. Figure 8.7 shows the variability in the DFT band gap for all simulation cells used in the structural calculations.

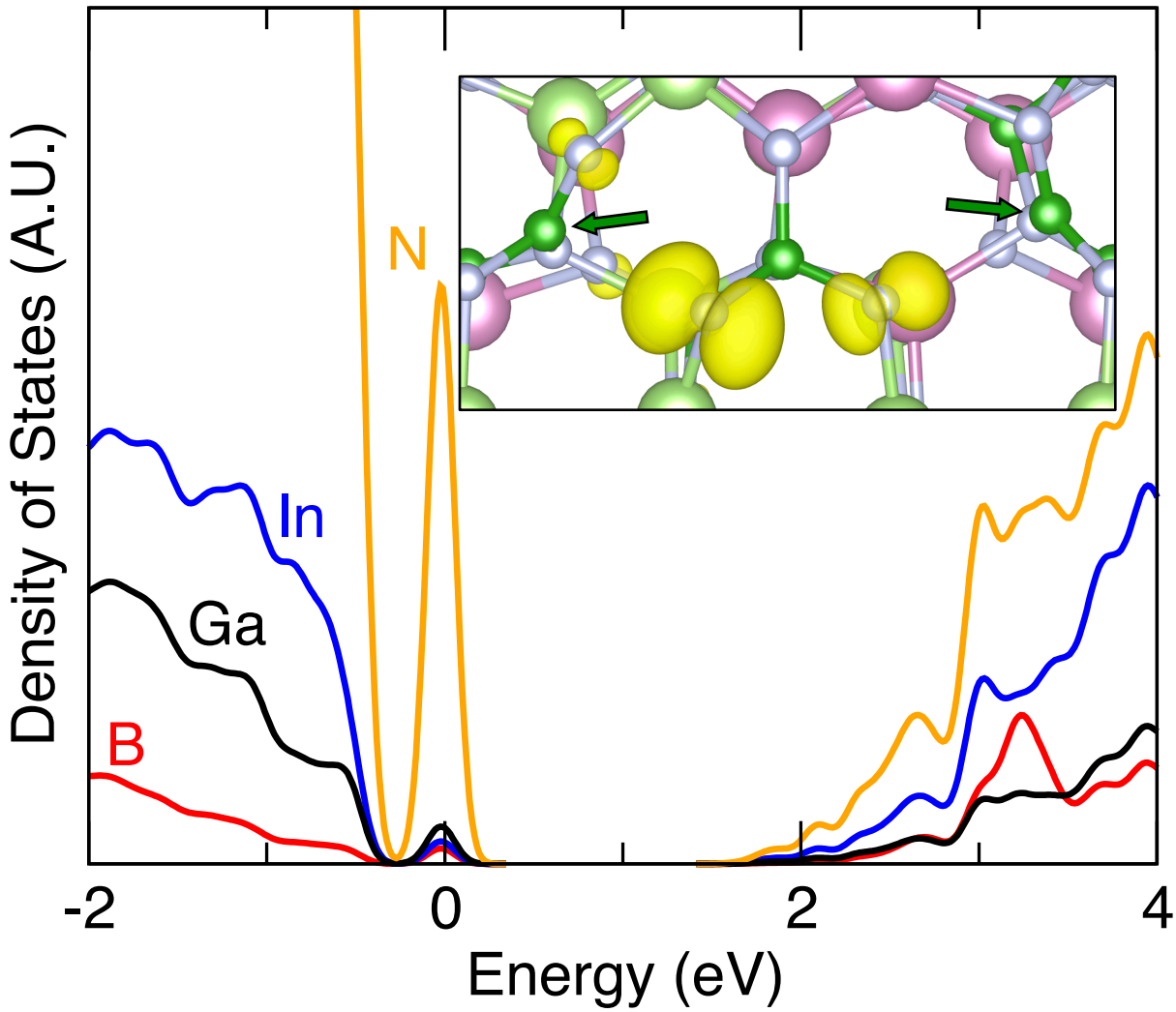

Figure 8.5. Projected Density of States (pDOS) for a $B_{10}In_{15}Ga_{11}N_{36}$ solid solution. Similar to InGaN, the conduction-band edge is primarily composed of In and N states. The valence band displays a localized band of N 2p character caused by local planarization of B-N bonds near boron atoms. The electron density of the localized state and the planarized B atoms are visualized in the inset. The pDOS calculated with HSE06 and optB86b-vdW is qualitatively similar, the only major quantitative difference being the band-gap value (Fig. 8.8)

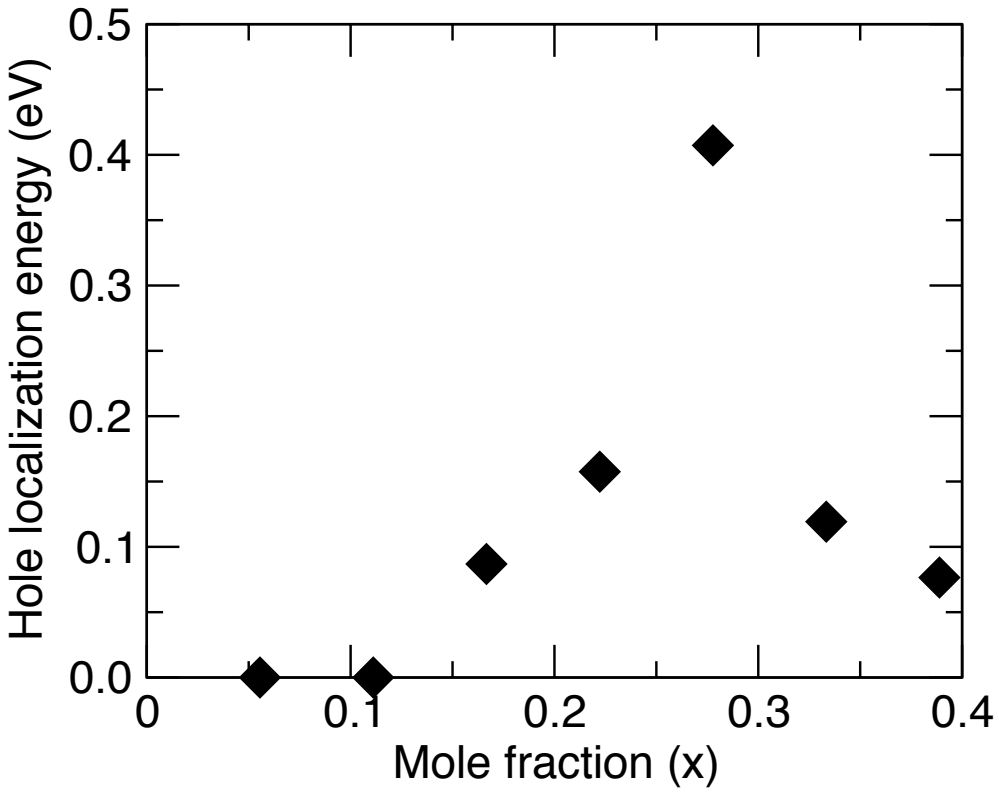

Figure 8.6. Hole localization energy for $B_xIn_{1.5x}Ga_{1-2.5x}N$ calculated using HSE06. No localized states are seen at boron mole factions less than ~0.1. The hole localization energy is maximum near the $B_{0.278}In_{0.417}Ga_{0.306}N$ composition.

The addition of boron into InGaN active layers is a promising method of overcoming the LED droop and green-gap problems. The better lattice match with GaN and the resulting reduced strain allows the growth of thicker active layers, thus decreasing the carrier concentration for a given current density and hence the fraction of carriers that recombine via Auger. While the spatial separation of carriers by the polarization fields in polar wells is amplified for thicker layers at low carrier concentrations, the polarization fields are screened by free carriers under high-power operation and flat-band conditions prevail.[140] Our estimate for the Debye screening length $L_D = \sqrt{\frac{k_B T}{4\pi n e^2}}$ is approximately 0.5 nm for typical carrier densities ($n \cong 5 \times 10^{18}$ cm^{-3}) of the internal quantum efficiency maximum.[140] Therefore, for sufficiently thick wells (e.g., thicker than 10 nm) and high carrier densities the polarization fields are completely screened by free carriers.

One challenge regarding the growth of BInGaN is the different temperatures needed for the ingredient materials. GaN is typically grown at high temperature to achieve higher crystalline quality, but InGaN and BGaN are typically grown at lower temperatures to facilitate In and B incorporation.[153,155] However, the lower enthalpy of mixing B into quaternary BInGaN than in ternary BGaN may facilitate the growth of BInGaN in a wider temperature window. E.g., Gautier, Ougazzaden, et al. successfully grew BInGaN with up to 2% boron and 14% indium using MOVPE at 730 °C.[157,158] Another potential challenge is the appearance of secondary phases during growth. Gunning et al. found that BGaN creates a twinned cubic structure at their selected growth conditions.[155] Similar cubic secondary phase inclusions may also form during BInGaN growth and deteriorate the structural quality. Hence, the thermodynamics of both hexagonal and cubic phases of BInGaN need to be further investigated both experimentally and theoretically to facilitate the development of device-quality materials.

8.4 Summary

In conclusion, we examine the effects of co-alloying boron and indium into GaN with first-principles calculations. Alloying 2B:3In into GaN creates alloys with gaps similar to InGaN of the same indium concentration, while reducing lattice mismatch and nearly eliminating it for alloys with In mole fractions less than 0.2 (i.e., band gaps larger than 2.75 eV). Our thermodynamics analysis reveals that B is more easily incorporated into InGaN than into pure GaN. Our results point to BInGaN alloys as promising materials to fabricate thicker active regions than InGaN for higher-efficiency high-power visible LEDs.

8.5 Acknowledgements

This work was supported by the Designing Materials to Revolutionize and Engineer our Future (DMREF) Program under Award No. 1534221, funded by the National Science

Foundation. This research used resources of the National Energy Research Scientific Computing (NERSC) Center, a DOE Office of Science User Facility supported under Contract No. DE-AC02-05CH11231.

8.6 Supplemental Information

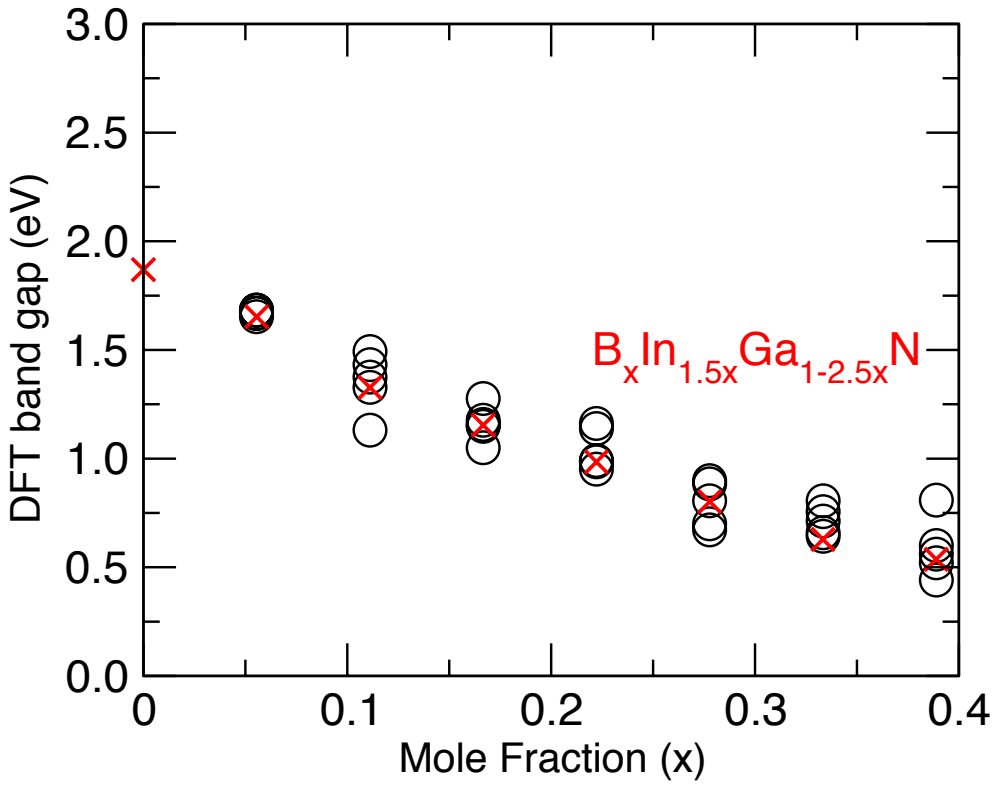

Figure 8.7. Band gap of $B_xIn_{1.5x}Ga_{1-2.5x}N$ vs. boron mole fraction calculated with the optB86b-vdW functional for all cells used in the structural-analysis calculations. The band gap for each configuration is shown using black circles, while the red crosses denote the cells that most closely match the random pair-correlation functions at each composition that were subsequently used for the HSE06 electronic-structure calculations (Figures 8.4 and 8.6).

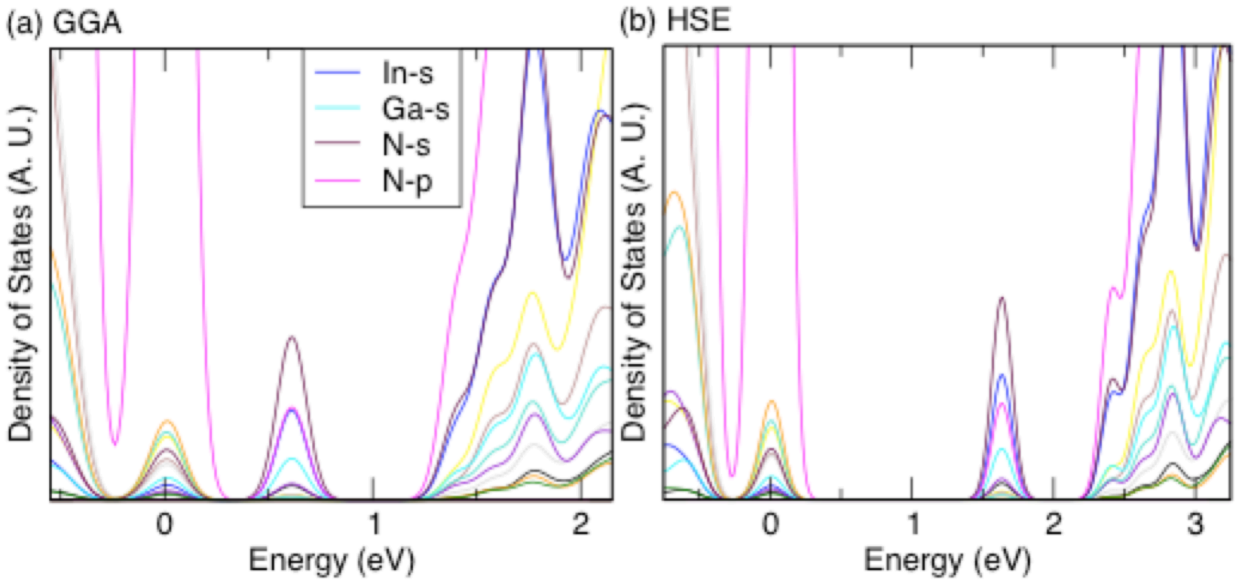

Figure 8.8. Partial Density of States (pDOS) of a $B_{10}In_{15}Ga_{11}N_{36}$ solid solution calculated (a) with the optB86b-vdW functional and (b) with the HSE06 functional, using a 2x2x2 Γ-centered Brillouin-zone sampling grid. Energies are referenced with respect to the highest occupied valence band state. Both functionals display qualitatively similar pDOS, with the only significant quantitative difference being the increased value of the band gap with HSE. The gap observed in the conduction band is an artifact caused by under-sampling of the Brillouin zone. For this reason, the optB86b-vdW functional with a rigid shift applied to correct for the band-gap underestimation was used to converge the pDOS in Figure 5 as a function of Brillouin-zone sampling (with an 8x8x8 Γ-centered grid). The hole localization energy with optB86b-vdW is 0.354 eV, while HSE with a 25% Hartree-Fock mixing parameter increases the localization energy by ~15% to 0.407 eV. Using a mixing parameter of 29.63%, which causes the calculated band gap of GaN to match experiment, has a negligible effect (~4 meV change) on the localization energy.

Chapter 9 $B_xIn_yGa_{1-x-y}N$ in the Wurtzite and Zincblende phases

This chapter is primarily adapted from a manuscript draft in which the author is 2nd author. The manuscript is by Kevin Greenman, Logan D. Williams, and Emmanouil Kioupakis. The author provided mentoring, training, workflows, editing, and data analysis.

9.1 Introduction

InGaN light-emitting diodes (LEDs) enable significant energy and cost savings over incandescent and fluorescent lighting. Even greater cost savings can be achieved by increasing their efficiency or operating at higher power while keeping their efficiency high.[139] However, the ability of InGaN LEDs to operate with high efficiency at high power is hindered by the decrease of their internal quantum efficiency at high power (*efficiency droop*). This efficiency reduction is especially prevalent at longer wavelengths (*green gap*). Previous work has demonstrated that Auger recombination makes a significant contribution to the LED efficiency droop.[140] Since the Auger recombination rate is a function of a material-intrinsic Auger coefficient[141] and the electron and hole densities in the material, lowering the carrier density by increasing the InGaN quantum-well thickness and hence the active-region volume is the most promising and already demonstrated[142] method to reduce the Auger losses in InGaN. However, there are several materials challenges with this approach. The lattice mismatch between the InGaN active region and the underlying GaN layers causes performance-degrading dislocations to form if InGaN is grown beyond a certain critical thickness (e.g., 5 nm for $In_{0.15}Ga_{0.85}N$).[170] Furthermore, the currently used multiple-quantum-well (MQW) structures also do not solve the droop problem

because for the same total active thickness, a single InGaN layer has higher efficiency than an MQW structure. This is because hole injection is poor through multiple layers in MQWs and only the first few QWs near the p-layer emit light.[143–145]

The lattice mismatch of InGaN to GaN can be addressed by co-alloying it with boron nitride to produce BInGaN alloys. These quaternary alloys maintain an approximate lattice match to GaN while allowing for a band gap that is adjustable throughout the visible range.[171] Co-alloying has previously been demonstrated as a method to independently vary the lattice constant and band gap in other material systems. Chai et al. found that the incorporation of Bi into $In_{0.53}Ga_{0.47}As$ to form $In_{0.53}Ga_{0.47}Bi_xAs_{1-x}$ increases the lattice constant and lowers the band gap for x up to 0.058.[172] Co-alloying has also been examined in $GaAs_{1-x-y}P_xBi_y$[173] and $GaAs_{1-x-y}N_xBi_y$[174,175], where the co-incorporation of P (N) and Bi yields alloys lattice-matched to GaAs and reduces the band gaps. Although BN preferentially crystallizes in the planar hexagonal structure, it is expected that for low BN content BInGaN alloys also adopt the wurtzite structure to minimize dangling bond formation and have a direct band gap determined primarily by the InGaN component. Previous work has shown that an approximate ratio of B:In ≈ 2:3 in wurtzite BInGaN produces alloys that are nearly lattice-matched to GaN.[171] This prediction agrees with a first-order approximation of the in-plane lattice constant of BInGaN by Vegard's law. Therefore, maintaining this B:In ratio while varying the Ga content enables the tuning of the band gap while still maintaining the lattice match to GaN that is necessary to increase the active region volume and achieve higher efficiencies.

These predictions are also supported by previous computational studies of BInGaN systems. Assali et al. used density functional theory (DFT) calculations with the local density approximation (LDA), generalized gradient approximation (GGA), and modified Becke-Johnson

(mBJ) exchange-correlation functionals to examine nine different compositions of ordered cubic BInGaN. They found a lattice match at $B_{0.125}In_{0.187}Ga_{0.688}N$, which has approximately the 2:3 B:In ratio. Additionally, they found that In alloying reduces the band gap while B alloying raises the direct gap slightly and has a nonlinear effect on the (larger) indirect gap.[163] Park and Ahn examined wurtzite BInGaN/GaN quantum wells using multiband effective mass theory and report a lower mismatch to GaN than InGaN and a large reduction in the internal polarization field.[162] This reduction increases carrier wave-function overlap and ultimately the predicted efficiency of light production. However, it is necessary to expand on this existing work using more accurate computational methods and accouting for compositional disorder in random alloys.

In this work, we explore the thermodynamic, structural, and electronic properties of wurtzite and zincblende $B_yIn_xGa_{1-x-y}N$ alloys as a function of composition. We show that BInGaN alloys in both phases can be lattice-matched to GaN within their respective regions of thermodynamic stability by adjusting their composition. The wurtzite phase is more stable for alloys with lower boron content and can be lattice-matched to GaN for compositions up to ~30% boron. The wurtzite and zincblende phases of the alloy both have direct band gaps that are tunable throughout the visible the range. We also found that planar hexagonal BInGaN is not stable at any composition tested. Our results demonstrate that quaternary BInGaN alloys are promising materials to increase the high-power efficiency of nitride LEDs.

9.2 Methodology

We employed the Vienna *Ab initio* Simulation Package (VASP)[42,73–75] to perform DFT calculations using the projector augmented wave (PAW) method.[71,72] We used a 600 eV plane-wave cutoff and GW-compatible pseudopotentials that included 3, 13, 13, and 5 valence

electrons for B, In, Ga, and N, respectively. For structural relaxations, we used the optB86b-vdW functional[165] and a Γ-centered Wisesa-McGill-Mueller Brillouin-zone grid with a minimum period distance of 21.48 Å.[166] Forces on atoms were relaxed to 1 meV/Å. We performed band-gap calculations with the Heyd-Scuseria-Ernzerhof (HSE06) functional.[14–16] The Alloy Theoretic Automated Toolkit (ATAT)[18] was used to model random alloys using Special Quasi-random Structures (SQSs). This was done using a 3x3x2 supercell for the wurtzite structures and 30-, 40-, and 48-atom supercells of variable shape for the zincblende and planar hexagonal structures. The arrangement of cations approximated the pair-correlation functions of random alloys up to 5.125 Å, which corresponds to the second-nearest neighbor in-plane and the nearest neighbor along the z-direction for wurtzite and the second-nearest neighbor in zincblende.

We tested several compositions at each of the 1:2, 2:3, 3:4, 4:5, and 1:1 B:In ratios. For each composition, we generated and relaxed an SQS in the wurtzite, zincblende, and hexagonal structures to determine structural parameters and thermodynamic properties. The Gibbs free energy was calculated using the analytical model for the entropy of a random solid solution, $S = -k_B \sum_{i=1}^{N} x_i \ln x_i$, where x_i is the mole fraction for each of the N alloy ingredients, and k_B is Boltzmann's constant. The hexagonal structures were not stable at any composition, so they were not included in future calculations. Since the 2:3, 3:4, and 4:5 ratios were closest to the expected lattice-matched compositions, we repeated the previous step four additional times at each composition for the wurtzite and zincblende structures (for a total of five SQSs at each composition). The electronic-structure calculations with the HSE06 functional were done for a single SQS for each composition that was selected because its band gap is close to the average PBE band gap of the five SQSs. We repeated these calculations for several alloys along the x- and y-axis of the $B_yIn_xGa_{1-x-y}N$ composition diagram (i.e., $B_yGa_{1-y}N$ and $In_xGa_{1-x}N$).

Finally, we fit models to the enthalpy of mixing, band gap, and lattice parameters as a function of composition for the wurtzite and zincblende structures. We used the regular solution model for the enthalpy of mixing:

$$\Delta H_{mix}(x,y) = xy\alpha_{\mathrm{BIn}} + x(1-x-y)\alpha_{\mathrm{InGa}} + y(1-x-y)\alpha_{\mathrm{BGa}} \quad \textbf{(9.1)}$$

the bowing model for the band gap:

$$E_g(x,y) = E_g^{\mathrm{BN}}y + E_g^{\mathrm{InN}}x + E_g^{\mathrm{GaN}}(1-x-y) + xy\beta_{\mathrm{BIn}} + x(1-x-y)\beta_{\mathrm{InGa}} + y(1-x-y)\beta_{\mathrm{BGa}} \quad \textbf{(9.2)}$$

and a similar bowing model for the lattice parameters:

$$a(x,y) = a_{\mathrm{BN}}y + a_{\mathrm{InN}}x + a_{\mathrm{GaN}}(1-x-y) + xy\delta_{\mathrm{BIn}} + x(1-x-y)\delta_{\mathrm{InGa}} + y(1-x-y)\delta_{\mathrm{BGa}} \quad \textbf{(9.3)}$$

$$c(x,y) = c_{\mathrm{BN}}y + c_{\mathrm{InN}}x + c_{\mathrm{GaN}}(1-x-y) + xy\theta_{\mathrm{BIn}} + x(1-x-y)\theta_{\mathrm{InGa}} + y(1-x-y)\theta_{\mathrm{BGa}} \quad \textbf{(9.4)}$$

9.3 Results

The thermodynamic, structural, and electronic properties of BInGaN alloys are plotted in Figs. 9.1 and 9.3-6. The colormap areas indicate the region that includes our explicit calculations at 1:2, 2:3, 3:4, 4:5, and 1:1 B:In composition ratios. The isolines illustrate how our fitted models interpolate between the explicitly calculated BInGaN results and the data for ternary BGaN and InGaN alloys located on the axes.

9.3.1 Thermodynamic Properties

Our calculated results for the enthalpy of mixing and the phase-transition temperature between the solid solution and phase segregation are shown in Fig. 9.1, while our fitted model parameters to the enthalpy of mixing are listed in Tables 9.1 and 9.2. Both for the wurtzite and for the zincblende phases, the enthalpy of mixing and the phase-transition temperature increase

as the boron mole fraction increases. Boron incorporation has a stronger effect on the enthalpy of mixing than indium. At indium mole fractions less than ~0.10 and boron mole fractions greater than ~0.03, indium addition reduces the phase-transition temperature due to increased configurational entropy.

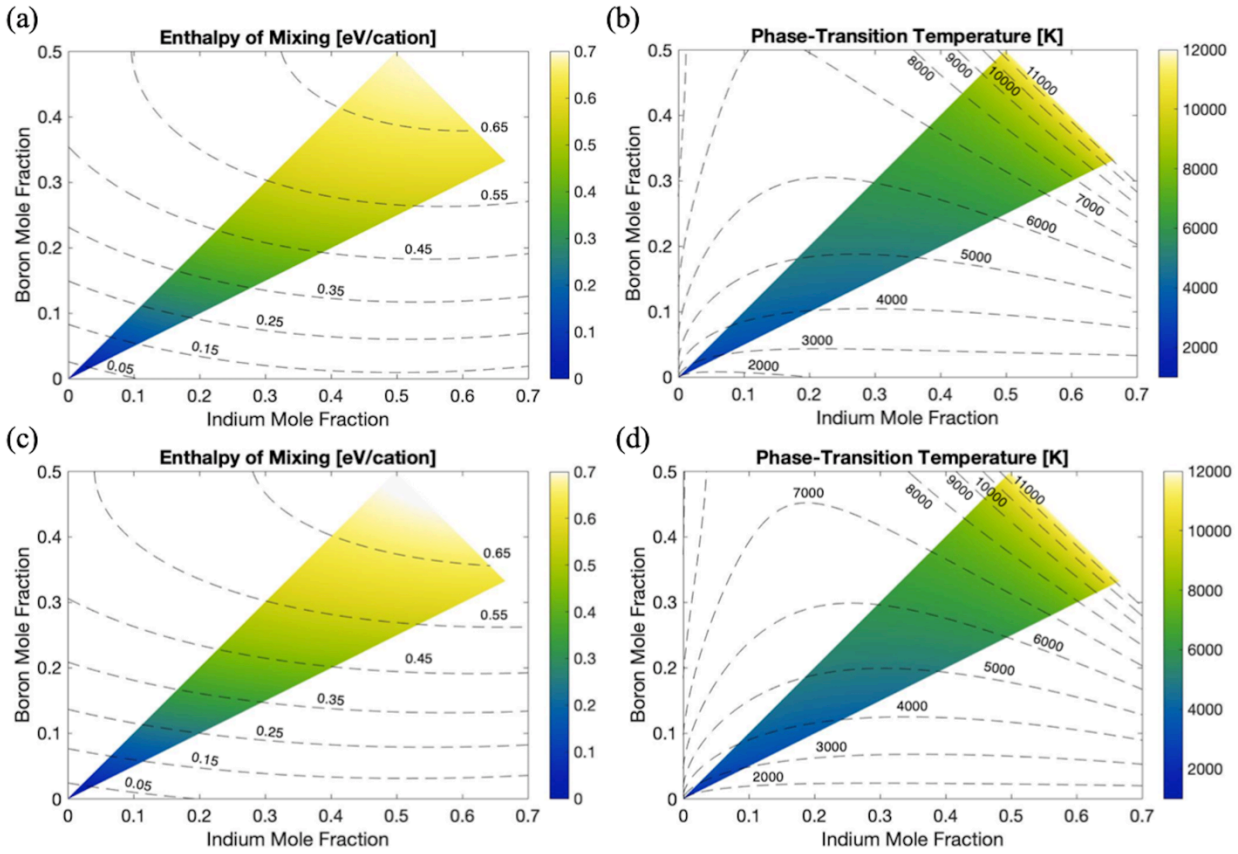

Figure 9.1. Thermodynamics of (a, b) wurtzite and (c, d) zincblende $B_yIn_xGa_{1-x-y}N$ alloys. (a, c) Calculated enthalpy of mixing per cation and (b, d) phase-transition temperature as functions of composition. The enthalpy of mixing and the phase transition temperature increase as the boron mole fraction increases.

We also compare the relative stability of the wurtzite and the zincblende phases as a function of composition since the enthalpy of mixing for both phases was calculated with respect to the same reference. Our results (Fig. 9.2) show that the wurtzite phase is more stable for quaternary BInGaN compositions closer to ternary InGaN, while the zincblende phase is more stable for those closer to ternary BGaN. For B compositions up to ~30%, the wurtzite phase of $B_yIn_xGa_{1-x-y}N$ can be stabilized with the addition of In and can even be lattice matched to GaN

by the co-incorporation of B and In at the appropriate ratio (discussed in the following section). This agrees with the expectation that the alloy adopts the wurtzite structure at low BN content to minimize dangling-bond formation. At boron compositions higher than 30%, the zincblende phase is the most stable independent of In content.

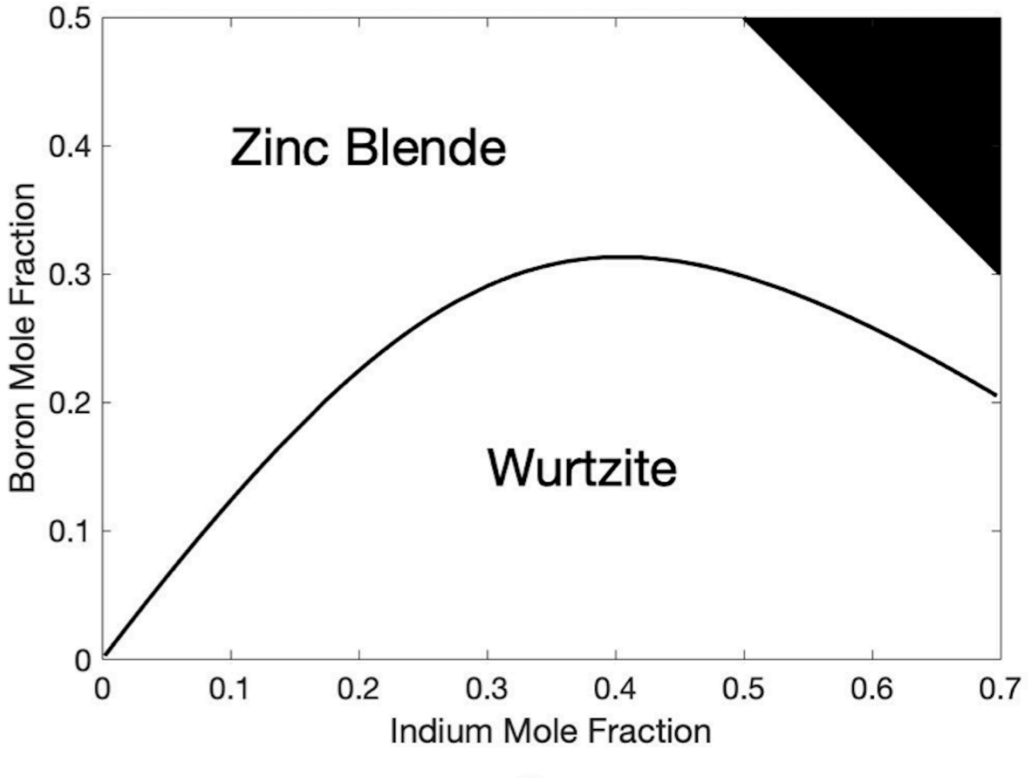

Figure 9.2. Relative thermodynamic stability of wurtzite and zincblende $B_yIn_xGa_{1-x-y}N$ alloys. The wurtzite phase is more stable at compositions closer to InGaN, and the zincblende phase is more stable at compositions closer to BGaN.

We also found that the planar hexagonal structure is less stable than both the wurtzite and zincblende structures at all compositions tested. We performed structural relaxations on planar hexagonal structures throughout the composition range. Of the structures tested, some relaxed into zincblende, some remained planar hexagonal, and others departed from the planar hexagonal structure but did not converge to another crystal structure. The structures that remained planar

hexagonal were generally higher in energy than the zincblende structure at the same composition by about 0.5 eV per cation.

9.3.2 Structural Parameters

We subsequently examined the lattice constants of the wurtzite and zincblende phases of $B_yIn_xGa_{1-x-y}N$ as a function of composition. Our results are plotted in Figs. 9.3 and 9.4, and our fitted model parameters are listed in Tables 9.1 and 9.2. For compositions up to ~5% B in the wurtzite phase, maintaining a composition ratio of approximately 2 parts B to 3 parts In provides a lattice match to GaN along the *a* direction (Fig. 9.3). The lattice-matched ratio increases at higher B compositions, reaching as high as ~3:2 for B compositions above 40%. This may be a result of the large size mismatch between B and Ga/In, since atomic size differences have been shown to contribute to deviations from Vegard's law.[176] The zincblende structure can also be lattice-matched to GaN, but the B to In ratio required for matching is much lower than that required for wurtzite (approximately 1 part B to 7 parts In at 5% B composition). The zincblende structural data is illustrated in Fig. 9.4.

By setting the left-hand side of Eqn. 3 equal to the *a* lattice parameter of wurtzite GaN, we can solve for the B composition (y) that provides a lattice match to GaN for a given In composition (x):

$$y = 2.357\left(\sqrt{x^2 - 1.455x + 1.049} + 0.984(x - 1.041)\right) \quad \textbf{(9.5)}$$

and similarly, for the c lattice parameter in wurtzite:

$$y = 4.124\times10^{-8}\left(\sqrt{-2.935\times10^{14}(x^2 - 57.986x - 252.834)} - 1.619\times10^{7}(x + 16.822)\right) \quad \textbf{(9.6)}$$

For the *a* lattice parameter in zincblende the B:In ratio lattice-matched to GaN is given by:

$$y = -3.966\left(\sqrt{x^2 - 1.342x + 0.387} + 1.050(x - 0.591)\right) \tag{9.7}$$

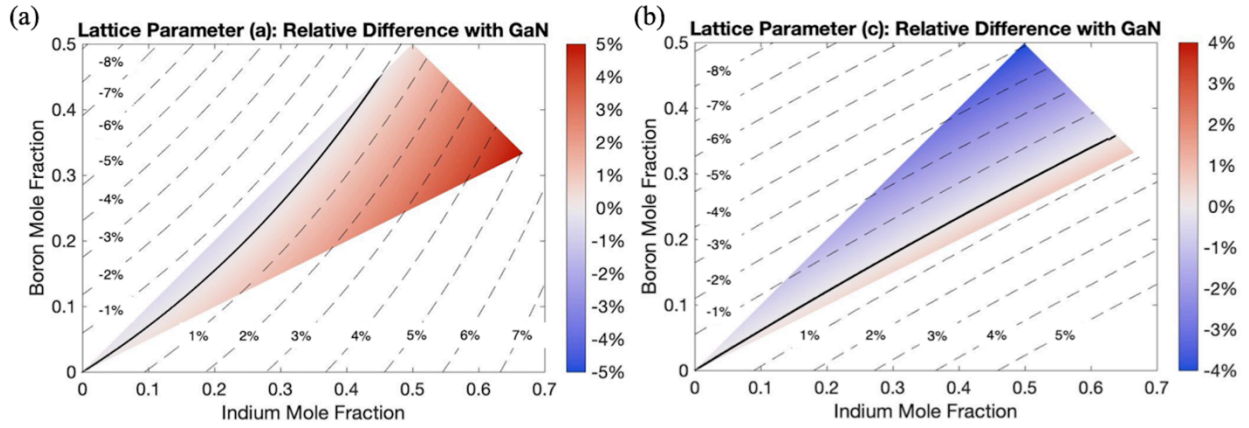

Figure 9.3. Relative difference of wurtzite $B_yIn_xGa_{1-x-y}N$ calculated lattice constants with that of GaN as a function of composition along the (a) *a* and (b) *c* directions. The solid black lines indicate an exact lattice match with GaN along each direction. The lattice-match line in (a) corresponds to Eqn. 9.5, and that in (b) corresponds to Eqn. 9.6. A ratio of approximately 2 B to 3 In provides a lattice match to GaN in the *a* direction for up to ~5% B composition.

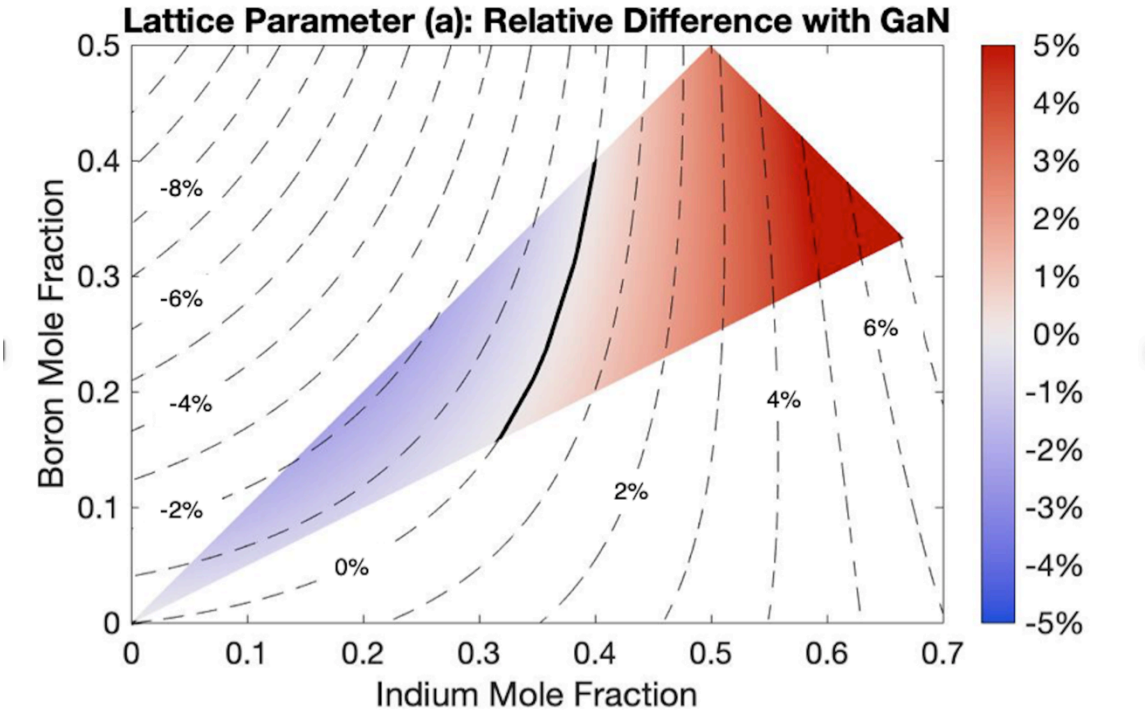

Figure 9.4. Relative difference of zincblende $B_yIn_xGa_{1-x-y}N$ calculated lattice constant with that of GaN as a function of composition. The solid black line indicates an exact lattice match with GaN and corresponds to Eqn. 9.7.

9.3.3 Band Gaps

We also calculated the band gap of $B_yIn_xGa_{1-x-y}N$ alloys and found that they span the entire visible spectrum both for the wurtzite and for the zincblende phases (Figs. 9.5 and 9.6). The fitted parameters to the gap-bowing model are listed in Tables I and II. The gap values calculated with HSE06 have been rigidly shifted by 0.25 eV (wurtzite) and 0.31 eV (zincblende) to match the experimental gaps (3.39 eV and 3.24 eV, respectively) of GaN at room temperature.[169,177,178] For both phases, the band gap monotonically decreases as the indium content increases, while the band gap displays strong bowing parameters with respect to B-In and B-Ga. The B-In and In-Ga bowing parameters (listed in Tables 9.1 and 9.2) are larger in magnitude for wurtzite, while the B-Ga bowing parameter is larger in magnitude for zincblende. In the wurtzite phase, small additions of boron to high-indium-content InGaN lower the band gap due to the large B-In bowing parameter. For zincblende, increasing boron mole fractions up to ~0.15 decreases the band gap, while increasing the boron amount beyond ~0.15 acts to increase the gap.

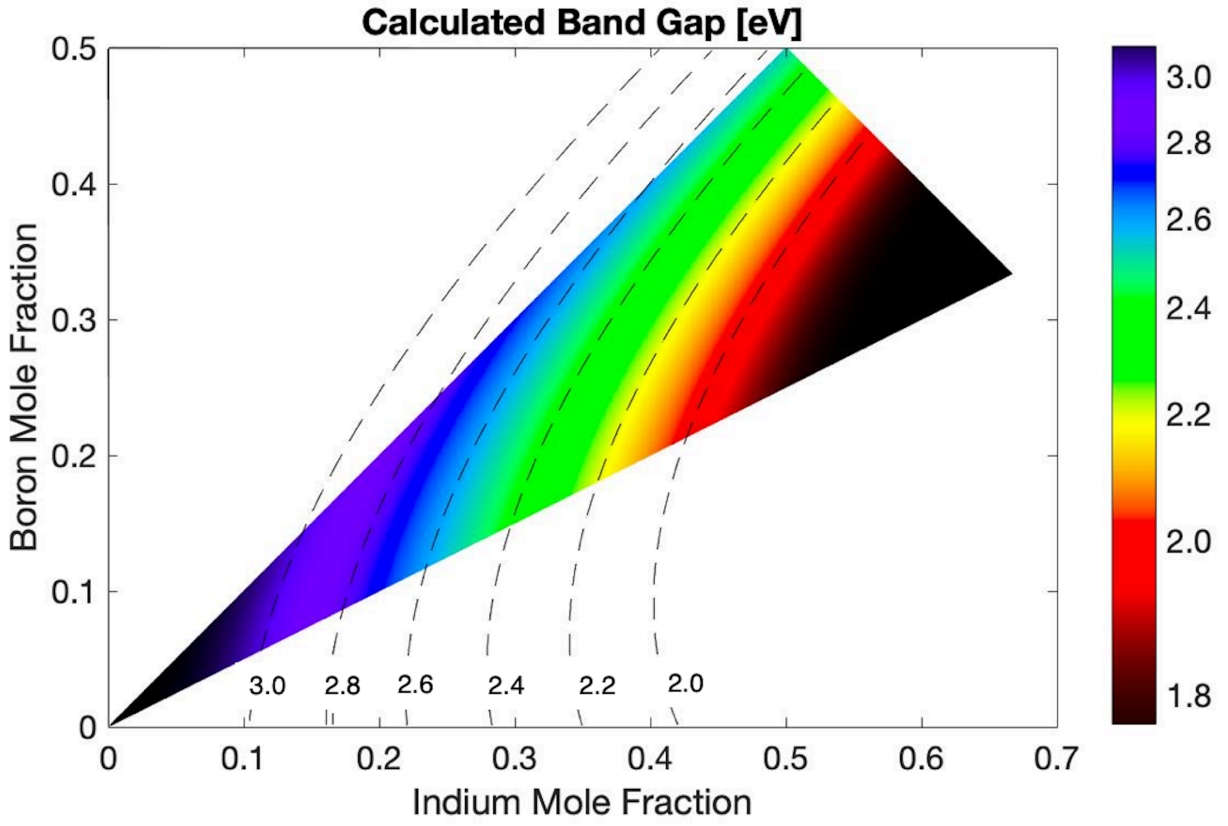

Figure 9.5. Calculated band gap of wurtzite $B_yIn_xGa_{1-x-y}N$ as a function of boron and indium mole fractions, depicted by the corresponding color on the visible light spectrum. The gap values calculated with HSE06 have been rigidly increased by 0.25 eV to match the experimental gap of wurtzite GaN at room temperature (3.39 eV).[169]

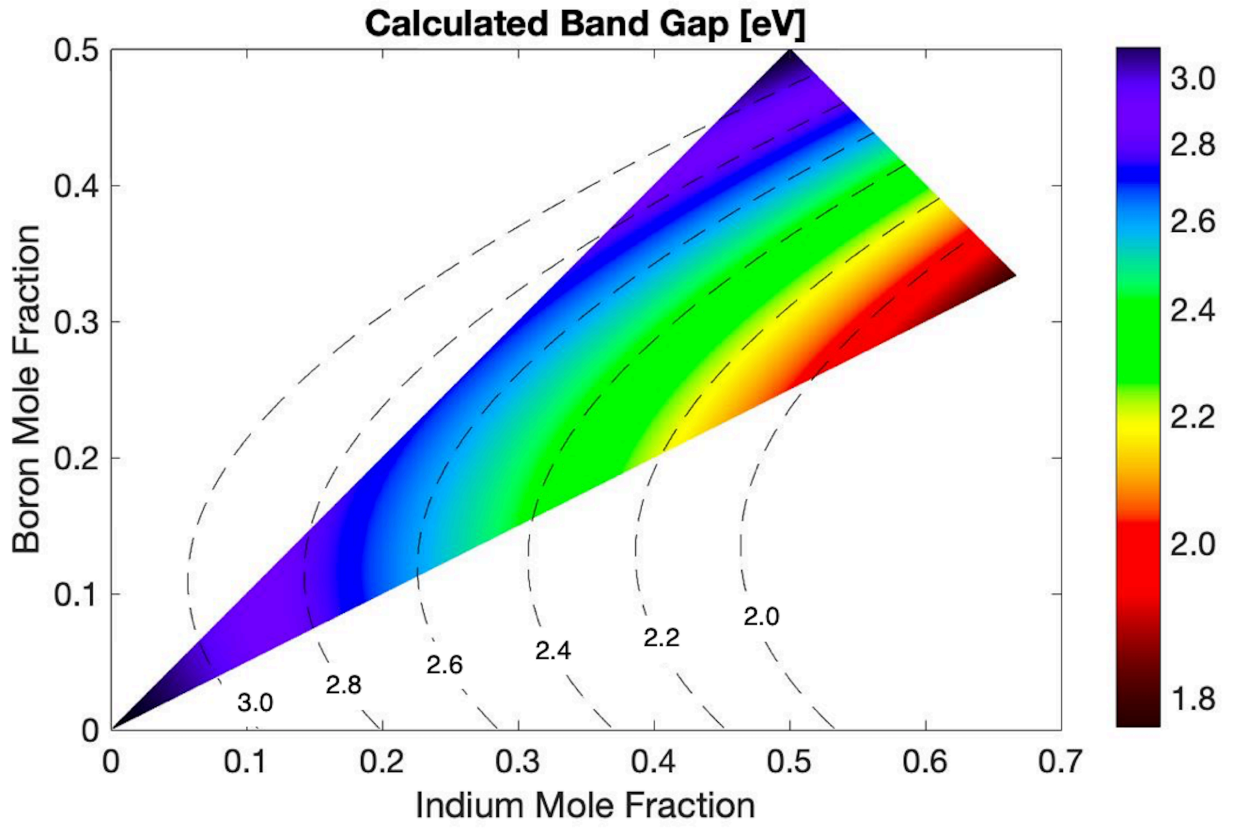

Figure 9.6. Calculated band gap of zincblende $B_yIn_xGa_{1-x-y}N$ as a function of boron and indium mole fractions, depicted by the corresponding color on the visible light spectrum. The gap values calculated with HSE06 have been rigidly increased by 0.31 eV to match the experimental gap of zincblende GaN at room temperature (3.24 eV).[177,178]

9.3.4 Lattice-Matched Compositions

The fitting parameters for each model are shown in Tables 9.1 and 9.2, and the data for wurtzite BInGaN lattice-matched to GaN along the *a* direction are summarized in Fig. 9.7. When limited to the lattice-matched compositions represented by Eqn. 9.5, the phase-transition temperature and enthalpy of mixing per cation monotonically increase as the In mole fraction increases. The enthalpy of mixing increases approximately linearly up to about 35% In. The band gap decreases up to about 38% In and subsequently increases for higher In content.

Table 9.1. Fitting parameters for the enthalpy of mixing, band gap, and lattice constant of wurtzite BInGaN alloys as a function of composition.

Property	ΔH_{mix}	E_g	a	c
Parameter	α	β	δ	θ
B-In	2.76 ± 0.04	-12.25 ± 0.23	0.60 ± 0.02	0.03 ± 0.05
In-Ga	0.52 ± 0.06	-1.38 ± 0.20	-0.02 ± 0.04	0.04 ± 0.08
B-Ga	1.97 ± 0.08	-6.15 ± 0.25	0.11 ± 0.04	0.04 ± 0.10

Table 9.2. Fitting parameters for the enthalpy of mixing, band gap, and lattice constant of zincblende BInGaN alloys as a function of composition.

Property	ΔH_{mix}	E_g	a
Parameter	α	β	δ
B-In	2.84 ± 0.05	-10.50 ± 1.47	1.30 ± 0.13
In-Ga	0.32 ± 0.04	0.35 ± 0.82	-0.37 ± 0.11
B-Ga	2.12 ± 0.06	-9.66 ± 0.93	-0.23 ± 0.14

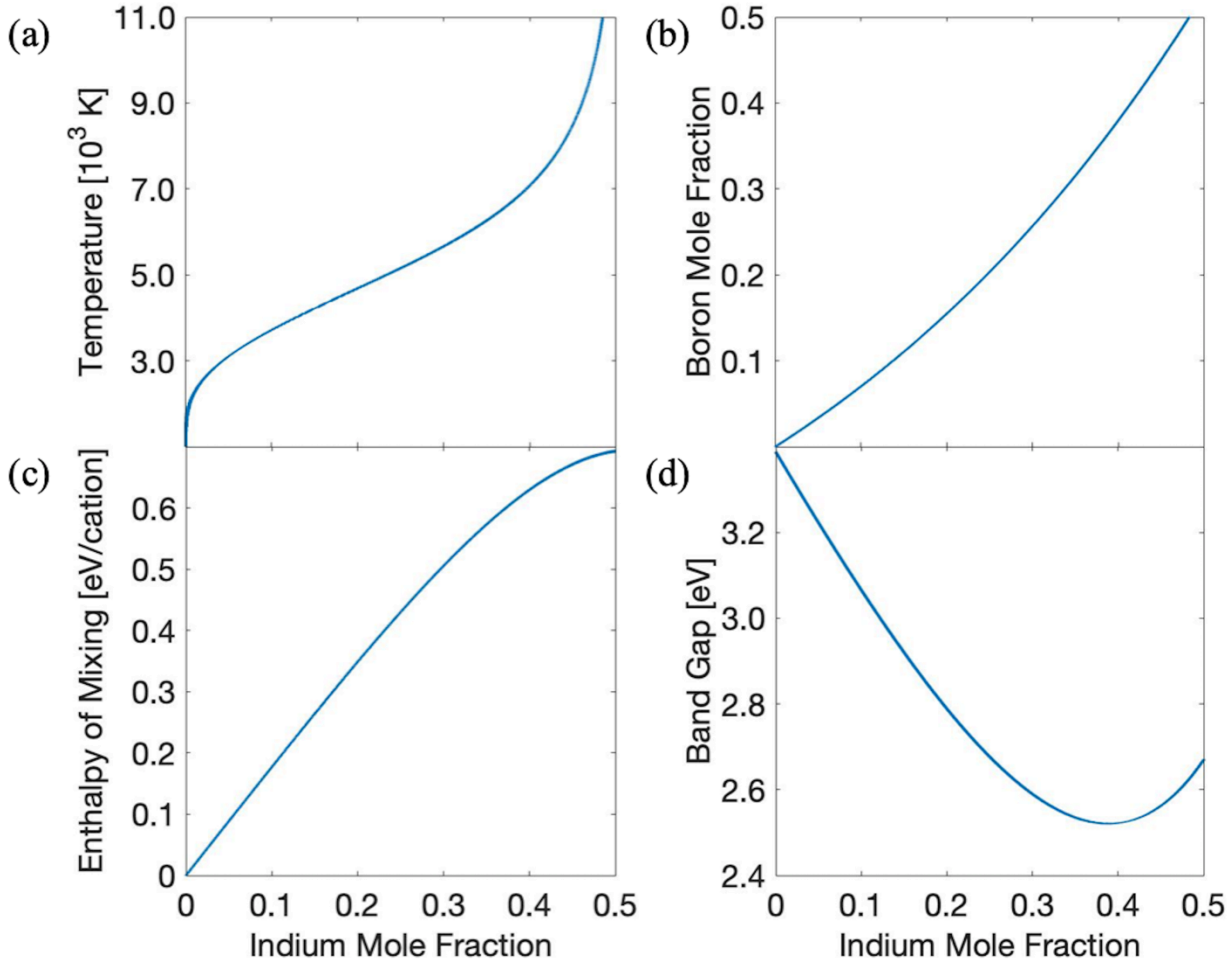

Figure 9.7. Calculated values for (a) phase-transition temperature, (b) enthalpy of mixing per cation, (c) boron mole fraction, and (d) band gap for wurtzite $B_{y(x)}In_xGa_{1-x-y(x)}N$ compositions exactly lattice matched to GaN along the *a* direction. As in Figure 6, the HSE06 calculated gap values have been rigidly increased by 0.25 eV to match the experimental gap of GaN at room temperature (3.39 eV).[169] The lattice-matched curve in (b) is represented by Eqn. 9.5.

9.3.5 Discussion

Our work using hybrid functionals agrees with that of Assali et al. using mBJ potentials to demonstrate In alloying reduces the band gap for zincblende $B_yIn_xGa_{1-x-y}N$.[163] However, our results show that increasing the boron content up to ~0.15 decreases the band gap and continuing to increase it beyond ~0.15 acts to increase the gap, while their work found a monotonic increase in the direct band gap with increasing boron addition.

Although our work has developed a more thorough understanding of the properties of BInGaN alloys, the validation of our predictions by growth experiments is challenging. Only the growth of low-boron-content quaternary BInGaN alloys has been achieved currently by Gautier et al.[157,158] and possibly McLaurin.[161] Gautier et al. reported smaller gaps and lattice constants than GaN for up to 2% B and up to 14% In composition for BInGaN grown on GaN/sapphire and ZnO-buffered Si substrates with metal-organic vapor phase epitaxy (MOVPE).[157,158] However, higher B content alloys may be possible. We can predict an upper limit on B content (using existing growth approaches) based on the demonstrated or predicted composition limits of $B_yGa_{1-y}N$. It is estimated that 1.5 times as much B can be incorporated into InGaN compared to GaN.[171] Cramer et al. observed up to 3% B incorporation into high-crystal-quality BGaN using plasma assisted molecular beam epitaxy (MBE).[154] This would lead to ~4.5% B incorporation in BInGaN. Calculations by Lymperakis predict that up to 25% B incorporation should be possible using MBE under N-rich conditions.[179] This growth technique presents its own challenges (e.g., lower crystal quality when grown under these conditions[179] and the higher cost of MBE compared to alternative techniques), but indicates that there may be alternate growth conditions that allow for far higher boron incorporation than has currently been achieved in bulk group-III nitride growths to date.

9.4 Conclusion

In summary, we applied hybrid DFT calculations to explore the properties of quaternary BInGaN alloys. Our results are in agreement with previous work that predicts a lattice match of BInGaN to GaN along the *a* direction with an approximately 2:3 ratio of B:In content. We have compared the thermodynamic stability of the wurtzite, zincblende, and planar hexagonal phases of BInGaN and determined the regions of relative stability. Our analysis shows that the wurtzite

phase is more stable and can be lattice matched to GaN for BInGaN compositions containing up to ~30% boron. As a result, co-alloying InGaN with BN produce wurtzite BInGaN alloys that maintain an approximate lattice match to GaN while allowing for a band gap that is adjustable throughout the visible range. This lattice match decreases strain, which in turn allows for the growth of thicker active layers without performance-degrading dislocations. The thicker active layer decreases the carrier concentration at a given carrier density and ultimately mitigates Auger recombination. Therefore, wurtzite BInGaN alloys offer a solution to the efficiency-droop and green-gap problems of InGaN LEDs and are promising material for higher efficiency high-power visible LEDs.

9.5 Acknowledgements

This work was supported by the Designing Materials to Revolutionize and Engineer our Future (DMREF) Program under Award No. 1534221, funded by the National Science Foundation. It used resources of the National Energy Research Scientific Computing Center, a DOE Office of Science User Facility supported by the Office of Science of the U.S. Department of Energy.

Chapter 10 Properties of BAlGaN Alloys Lattice-Matched to AlN

This chapter is primarily adapted from a manuscript draft in which the author is the primary author. The manuscript is by Logan Williams and Emmanouil Kioupakis.

10.1 Introduction

The efficient generation of UV light is crucial to many technological applications. UV light in the wavelengths of 230 – 350 nm is capable of sensing and measuring many dyes, ink, and markers, as well as nitrogen urea and blood gas levels, and can be used for protein analysis and DNA sequencing. 300 – 360 nm light is useful for UV curing, which enables solvent-free, more environmentally responsible printing. Most importantly, 260 – 280 nm light can be used for disinfection and sterilization.[180,181]

AlGaN based LEDs are the most promising UV generation technology currently being developed. AlGaN alloys can span a wide emission spectrum from 6.2 eV (AlN) to 3.4 eV (GaN). They provide high-efficiency emission of light compared to many other classes of materials, can be doped both n- and p- type (though p- type doping is currently marginal), have robust mechanical properties, and are free from harmful elements such as lead, arsenic, and mercury.[181] The primary competitor technology in the field of UV sterilization is the mercury-based UV lamp,[182] but the Minamata Convention on Mercury[183] has over 100 nations pledged to phase out mercury-based technologies.

Despite the many attractive properties of AlGaN-based UV LEDs, their efficiency is still hampered by many material issues. P-type doping is difficult in AlGaN, and p-AlGaN has a low

conductivity. p-GaN is often used in place of p-AlGaN for this reason, but p-GaN absorbs UV light, making light extraction from the LED difficult.[181] Making temperature stable and UV reflective contacts to the n- and p- layers with low ohmic resistances is also a challenge.[180] Light polarization becomes an issue for high Al-content LEDs, as the polarization of emitted light switches from TE polarized light (emitted along the *c* direction) to TM polarized light (emitted in-plane) above 68% Al for 3 nm $Al_xGa_{1-x}N$ quantum wells and light extraction becomes very difficult.[184,185] Finally, Threading Dislocation Densities (TDD) of greater than $1x10^9$ cm^2 are detrimental to device efficiency and lifetime,[186,187] while the standard, most cost-effective substrate sapphire produces TDDs of $2x10^9 – 1x10^{10}$ without more complicated growth processes such as patterned overgrowth or pulsed growth techniques.[187] AlN substrates exist and have far lower native TDDs, but lattice mismatch between the AlN substrate and subsequent layers (up to 2.4% for GaN) can be large enough to nucleate new threading dislocations.

Co-alloying of materials is an established technique that can be used to vary the band gap and the lattice constants of a material independently of each other. For example, GaAsPBi[146] and GaAsNBi[147] yields alloys lattice-matched to GaAs with a reduced band gap. The authors' previous work has shown this technique can be applied to produce BInGaN alloys that lattice match GaN with reduced band gaps.[171] Vegard's Law can be used as a first order estimate of the lattice constants of an alloy. Based on the lattice constants of GaN (3.190Å), AlN (3.110Å), and w-BN (2.536Å),[150] an alloy of approximately $(B_{0.122}Ga_{0.878})_xAl_{1-x}N$ will be lattice matched to AlN.

Seoung-Hwan Park and Doyeol Ahn have performed theoretical studies on BAlGaN alloys for UV LEDs using multi-band effective mass theory.[188–192] They reported a significant increase in TE-polarized spontaneous emission due to a decrease in lattice mismatch between the

quantum well and the AlN substrate and decrease in internal field of the well for low Al content (20%).[188,189] They also reported a decrease in TE-polarized emission with boron addition at high Al content due to a shifting of valence band characteristic from heavy hole to crystal field split-off band.[188] However, their work utilizes erroneous values for the spontaneous polarization constants. They use −2.174 C/m^2 for BN from Dreyer's 2014 paper[193], which contains a sign error and is defined referenced to the hexagonal structure. They also appear to be using spontaneous polarization constants for the other materials that are defined referenced to the zinc blende structure, instead of the comparable, hexagonal-referenced values from Dreyer's 2016 paper.[194] The only experimental exploration of the BAlGaN alloy series that the author knows of was performed in 2000-2002 by Takano et al.[195–197] and included alloys with up to 13% boron.

10.2 Methodology

In this work we explore the thermodynamic, optical, and structural properties of statistically random quaternary BAlGaN alloys using hybrid-functional DFT. A boron to gallium co-alloying ratio of ~1:9 is sufficient to nearly lattice match the alloy to AlN in the *a* direction. Co-alloying with boron and gallium slightly lowers the enthalpy of mixing while greatly increasing configurational entropy. Boron should be easily incorporated at the same concentrations that it can be in AlN (up to 10-15%). Additionally, replacement of aluminum with boron has negligible effect on the band gap, allowing these alloys to be used in place of AlGaN alloys with an equal fraction of Ga.

We performed DFT calculations based on the projector augmented wave (PAW) method,[71,72] as implemented in the Vienna *Ab initio* Simulation Package (VASP).[42,73–75] The GW-compatible pseudopotentials including 3, 3, 13, and 5 valence electrons were employed for B, Al, Ga, and N, respectively, with a 600 eV plane-wave cutoff. Structural relaxations were

performed using the optB86b-vdW functional[165] and a Γ-centered Wisesa-McGill-Mueller Brillouin-zone grid with a minimum period distance of 21.16 Å.[166] Forces on atoms were relaxed to within 1 meV/Å. Band gap calculations were performed with the functional of Heyd-Scuseria-Ernzerhof (HSE06).[14,15] Random alloys were modeled using Special Quasi-random Structures (SQSs) generated with the Alloy Theoretic Automated Toolkit[18] as 3x3x2 and 3x3x3 wurtzite supercells. Cations were arranged to approximate the pair-correlation functions of random alloys up to 5.125 Å. Five SQSs were generated at each composition for the BAlGaN alloys, and one SQS was generated for each composition for the BAlN, BGaN, and AlGaN alloys used as comparisons for the thermodynamic and optical properties. Piezoelectric coefficients and spontaneous polarization constants were calculated using PBE with the vdW relaxed structures after careful testing to confirm that results were negligibly effected by the use of the less computationally expensive functional.

10.3 Results and Discussion

10.3.1 Thermodynamics

Our thermodynamic analysis shows that the alloys studied should be easy to form. The transition temperature between the solid-solution and the miscibility gap regimes was calculated as a function of composition, $T(x) = \Delta H(x)/S$, where the enthalpy of mixing, ΔH, is the total energy difference between the alloy and the linear combination of the binary compounds that match the composition, and the entropy is evaluated using the regular solution model, $S = -k_B*\Sigma^N_{i=1} x_i*\ln(x_i)$, where x_i is the mole fraction for each of the N alloy ingredients, and k_B is Boltzmann's constant. The transition temperatures (Fig. 10.1) for $B_xAl_{1-x}N$ and $B_xGa_{1-x}N$ are well above typical growth temperatures for the materials, which is expected since nitrides are typically grown with epitaxial techniques such as MOCVD or molecular beam epitaxy that occur

far from thermodynamic equilibrium. These temperatures can not be directly correlated to solubility limits, as boron incorporation is limited to ~3% in GaN[154] and ~15% in AlN[198] while their transition temperatures follow very similar curves. However, they are useful comparative plots to compare alloys of a material. $B_xAl_{1-9x}Ga_{8x}N$ and $B_xAl_{1-10x}Ga_{9x}N$ both have far lower transition temperatures than equal boron content $B_xAl_{1-x}N$ and $B_xGa_{1-x}N$ alloys. This is attributable to the much larger configurational entropy in the quaternary alloys, while the enthalpy of mixing is roughly equivalent. The enthalpy of mixing of the quaternary alloys is very slightly lower than the combined enthalpy of mixing of boron into AlN (or GaN) and enthalpy of mixing of $Al_yGa_{1-y}N$ that the quaternary corresponds to. (Fig. 10.2) The reduced enthalpy of mixing and the increased entropy indicate that the studied range of alloys should be easy to grow with current growth techniques, in agreement with the previous experimental work.[197]

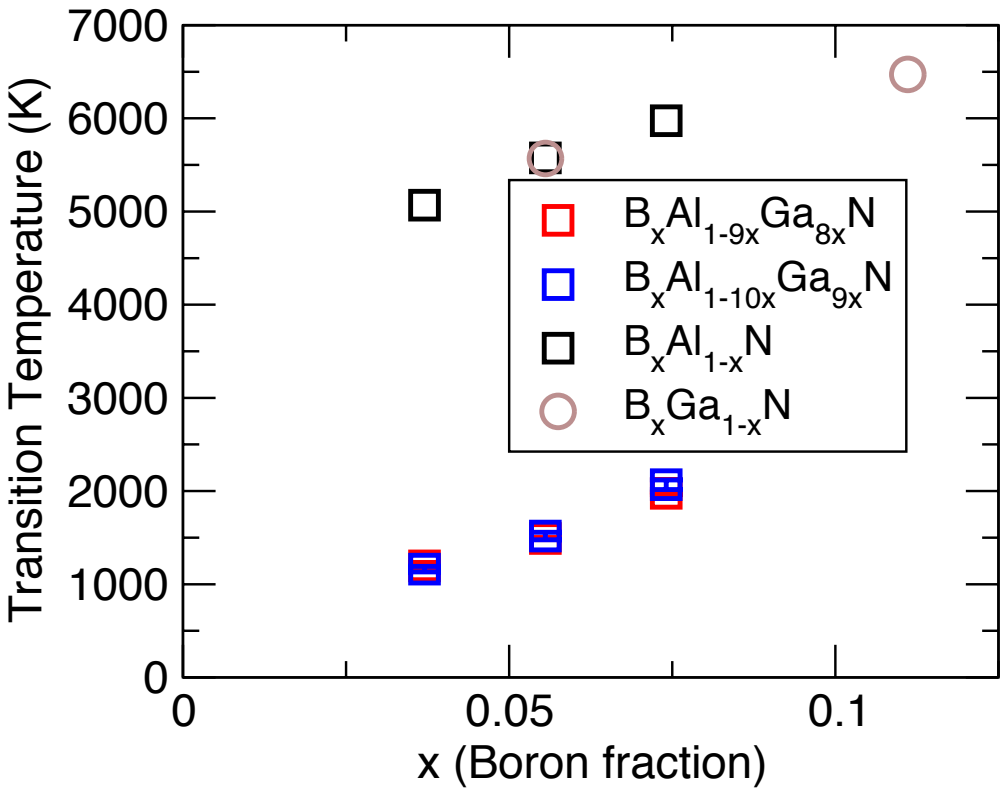

Figure 10.1. Transition temperature for thermodynamic stability between the alloy and the linear combination of group III nitride binaries as a function of boron fraction x for $B_xAl_{1-9x}Ga_{8x}N$, $B_xAl_{1-10x}Ga_{9x}N$, $B_xAl_{1-x}N$, and $B_xGa_{1-x}N$.

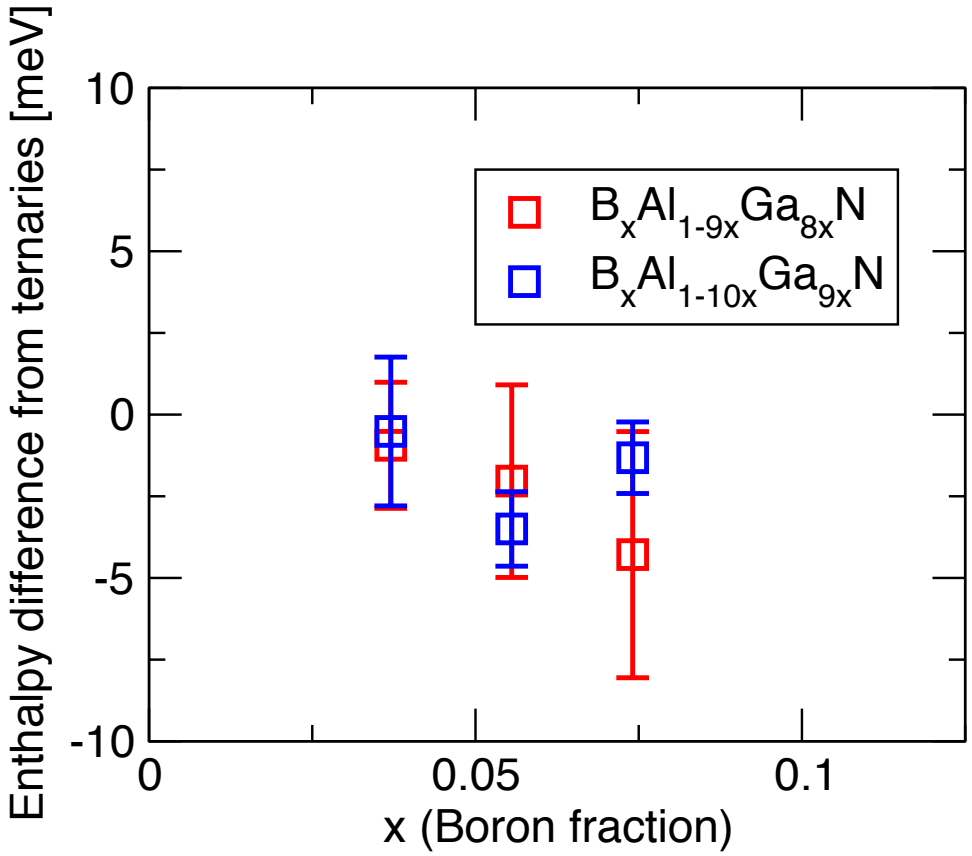

Figure 10.2. The enthalpy difference between ($B_xAl_{1-9x}Ga_{8x}N$, $B_xAl_{1-10x}Ga_{9x}N$) and the sum of the enthalpy for the equivalent $B_xAl_{1-x}N$ and $Al_{1-y}Ga_yN$ alloys.

10.3.2 Band Gap

Our calculations show that the partial substitution of aluminum with boron in $Ga_xAl_{1-x}N$ alloys does not significantly change the band gap for these low boron concentrations. Figure 10.3 shows the band gap vs. gallium fraction for $Al_{1-x}Ga_xN$, $B_{0.1x}Al_{1-1.1x}Ga_xN$, and $B_{0.11x}Al_{1-1.11x}Ga_xN$ alloys.

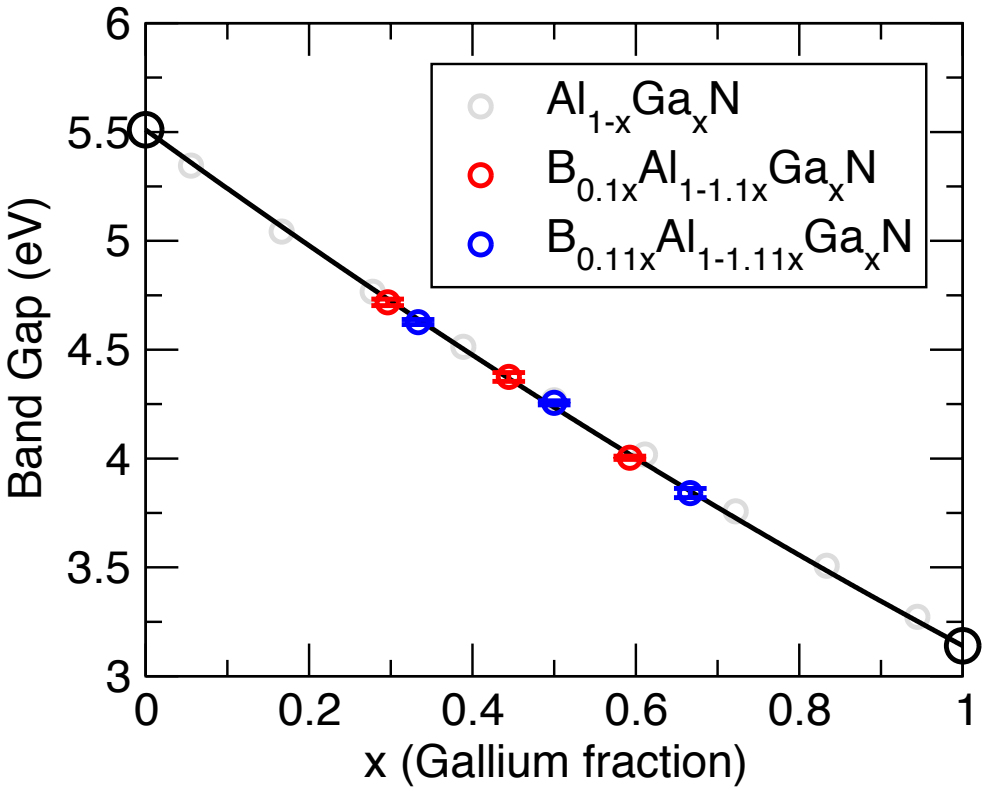

Figure 10.3. Band gap as calculated with HSE06 for $Al_{1-x}Ga_xN$, $B_{0.1x}Al_{1-1.1x}Ga_xN$, and $B_{0.11x}Al_{1-1.11x}Ga_xN$ as a function of gallium fraction x.

10.3.3 Lattice Parameters

Our structural calculations show that addition of boron allows for a significant reduction of lattice mismatch with AlN substrates compared to equivalent AlGaN alloys. $B_{0.11x}Al_{1-1.11x}Ga_xN$ is nearly lattice-matched to AlN in the *a* direction. Structural relaxations with the same vdW functional give *a* lattice constants of 3.193, 3.118, and 2.552 for GaN, AlN, and wurtzite BN. Vegard's law with these values would predict an optimal ratio of $B_{0.117x}Al_{1-1.117x}Ga_xN$. The *c* lattice constant is closer to that of the equivalent AlGaN alloy than AlN. This behavior is the opposite of the trend seen in boron doping of InGaN alloys, in which the *c* lattice direction responded more strongly than the *a* lattice direction to boron incorporation.[171] The exact cause of this behavior is unknown, but the authors speculate anisotropic lattice distortions based upon boron local bonding environments.

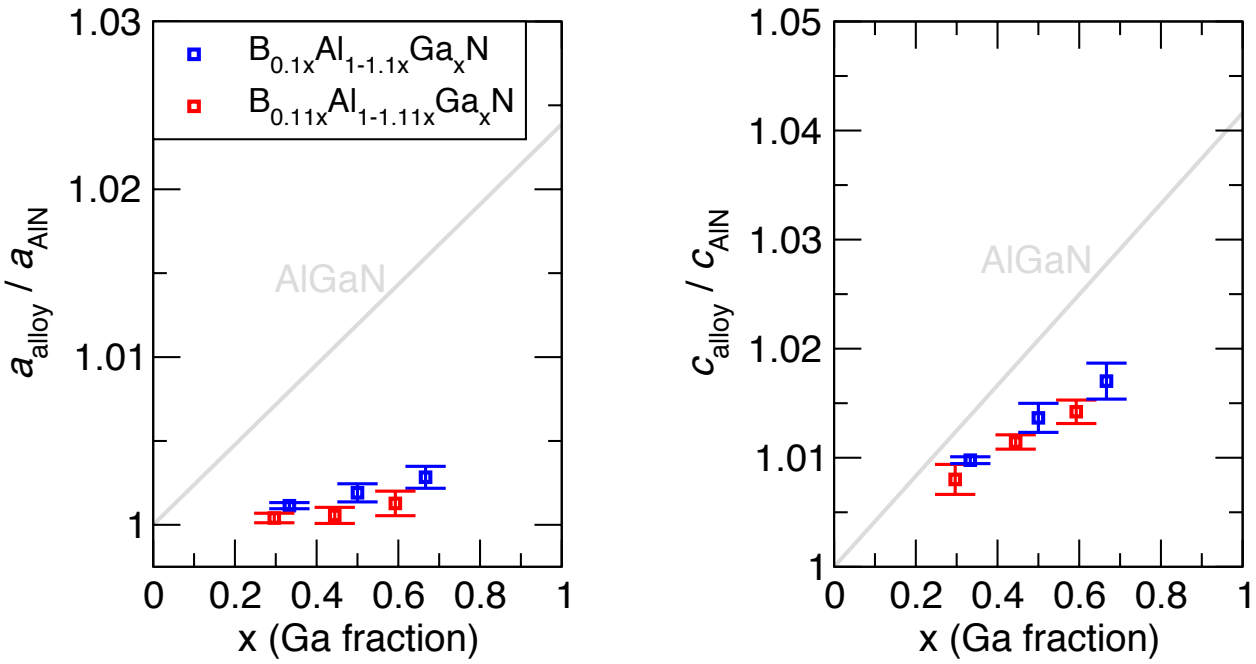

Figure 10.4. Ratio of the alloy lattice constant to AlN's lattice constant for the in-plane *a* (left) and out-of-plane *c* (right) directions for $B_{0.1x}Al_{1-1.1x}Ga_xN$ (blue) and $B_{0.11x}Al_{1-1.11x}Ga_xN$ (red) as a function of gallium fraction x. Grey line shows the values for $Al_xGa_{1-x}N$ alloys for comparison. The *a* lattice parameter is reduced more by the substitution of aluminum for boron than the *c* lattice parameter is.

10.3.4 Light polarization and u Parameter

There exists a strong trend between the structural u parameter (z direction fractional displacement of the 2nd atom type from the first) in wurtzite group III nitrides and the character of their band edge. The 'ideal' wurtzite structure has a u parameter of 0.375, but all of the group III nitrides vary from this value. Table 10.1 shows the u parameter and difference between the heavy hole (HH) and crystal field split-off (CH) band energies for wurtzite BN, GaN, and InN. This effect is structural in nature, which can be seen by enforcing different u parameters in the calculations.

Table 10.1. u parameter and the energy difference between the heavy hole (HH) and crystal field split-off (CH) band energies at the Γ point for the group III nitrides.

material	u parameter	E(HH-CH) [eV]
AlN	0.3815	-0.225
GaN	0.3764	0.043
BN	0.3745	0.25

Knowing this trend, it can be expected that addition of boron to AlGaN alloys will extend the band gap range of alloys that emit TE polarized light. In alloys, the u parameter does not follow Vegard's law, but is well behaved in a bowing model for AlGaN, as shown in figure 10.5.

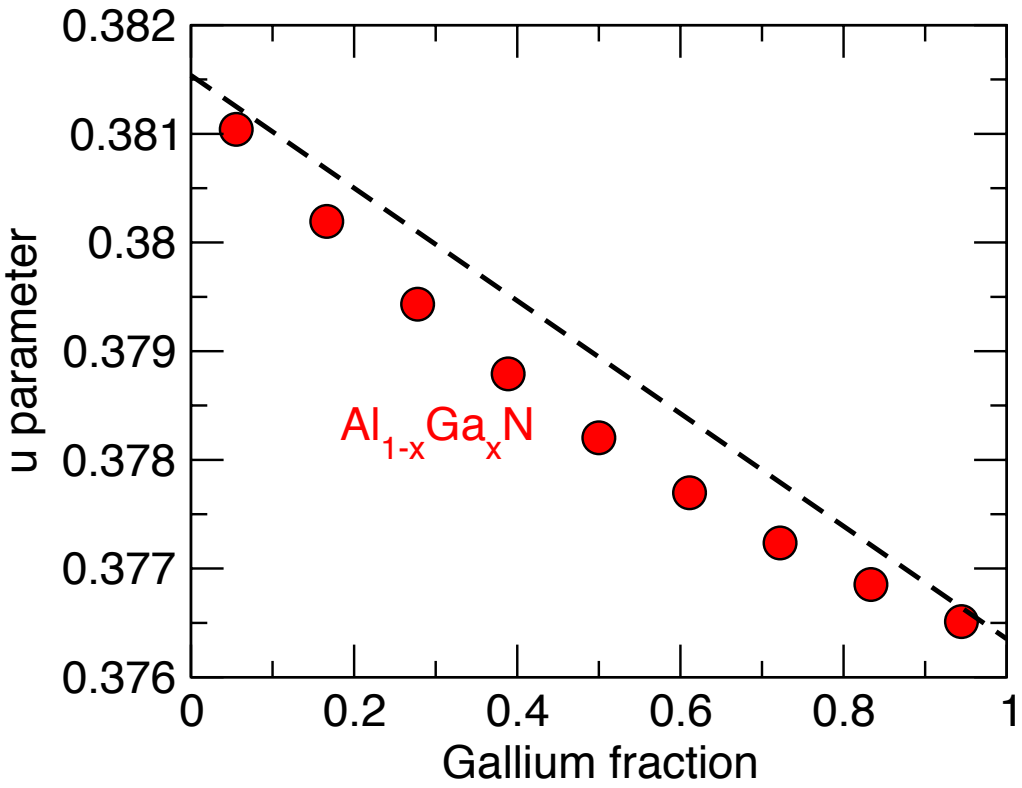

Figure 10.5. Structural u parameter as a function of the gallium fraction (x) for $Al_{1-x}Ga_xN$ alloys. The u parameter displays a bowing relationship with bowing parameter of b = 0.00299794.

Bowing in $B_xAl_{1-x}N$ for low boron content is roughly equal to 0, as shown in figure 10.6.

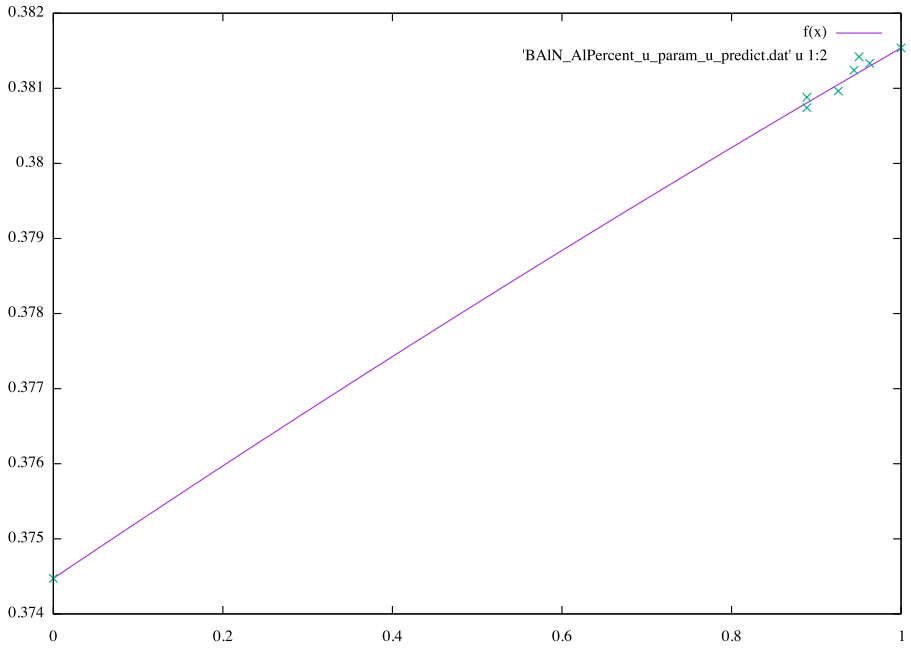

Figure 10.6. u parameter vs aluminum content in $B_xAl_{1-x}N$. For low boron content, the u parameter roughly follows Vegard's law.

The u parameter of the $B_xGa_{1-x}N$ system (Figure 10.7) shows a great deal of noise beyond a few percent boron, where the alloys are not experimentally stable.

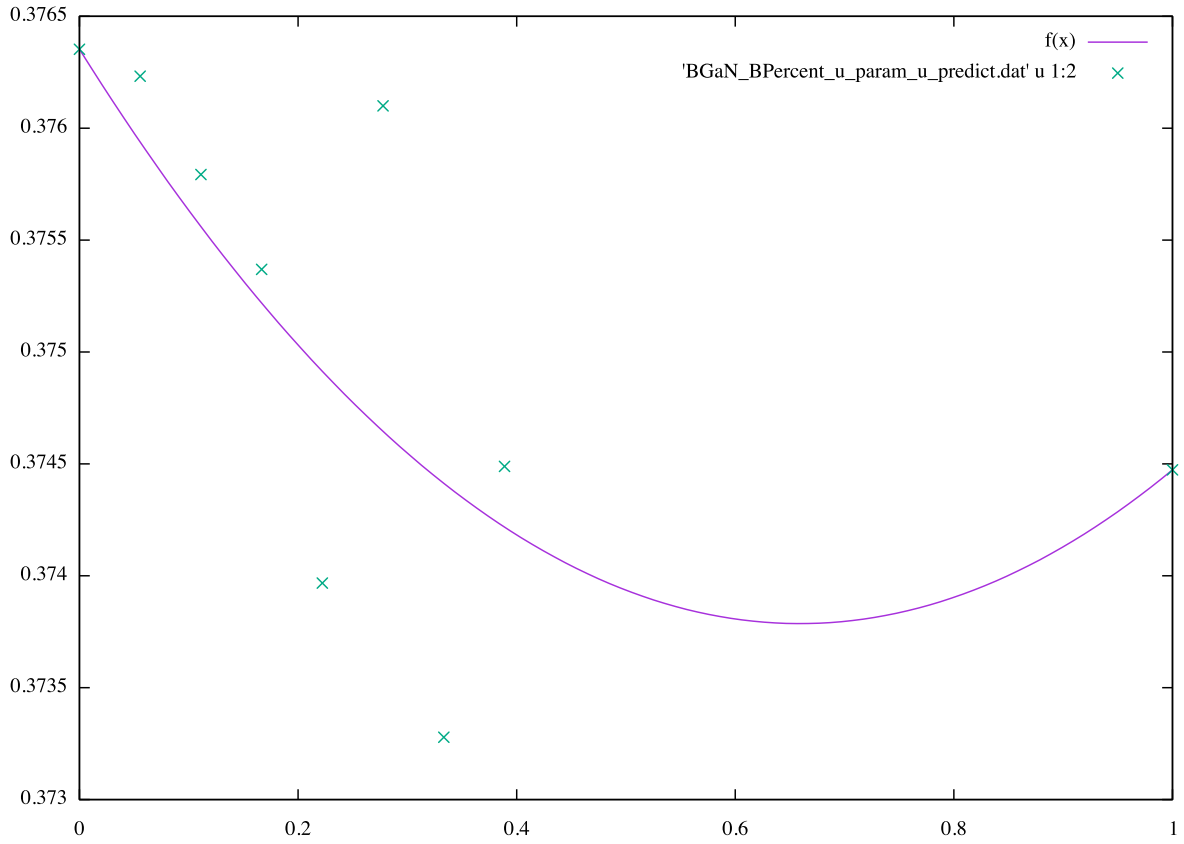

Figure 10.7. u parameter vs. the boron content (x) in $B_xGa_{1-x}N$ alloys. The data is very noisy at larger boron content, where the alloys are known to be experimentally unstable. The fit in this plot corresponds to b = 0.00590904.

The data in the previous three plots can be combined with the calculations from the $B_xGa_yAl_{1-x-y}N$ series and fit to a multi-component bowing model. If modeled using only 2 component bowing terms, the bowing parameters are $b_{B\text{-}Ga} = 0.00627796 \pm 0.001132$, $b_{Ga\text{-}Al} = 0.00264192 \pm 0.0005647$, and $b_{B\text{-}Al} = -0.0028915 \pm 0.002604$. If including a 3 component bowing term C, then the bowing parameters are $b_{B\text{-}Ga} = 0.00658883 \pm 0.001144$, $b_{Ga\text{-}Al} = 0.00358691 \pm 0.0008863$, $b_{B\text{-}Al} = -0.00059496 \pm 0.003074$, and $C_{B\text{-}Al\text{-}Ga} = -0.0180253 \pm 0.01311$. As shown in Figure 10.8, replacement of some aluminum by boron in these alloys series reduces the u parameter without changing the band gap, potentially allowing for TE emission at smaller emission wavelengths. However, the effects of strain are not included in this analysis and are

necessary for quantitative prediction of light emission polarization of LED quantum well systems.

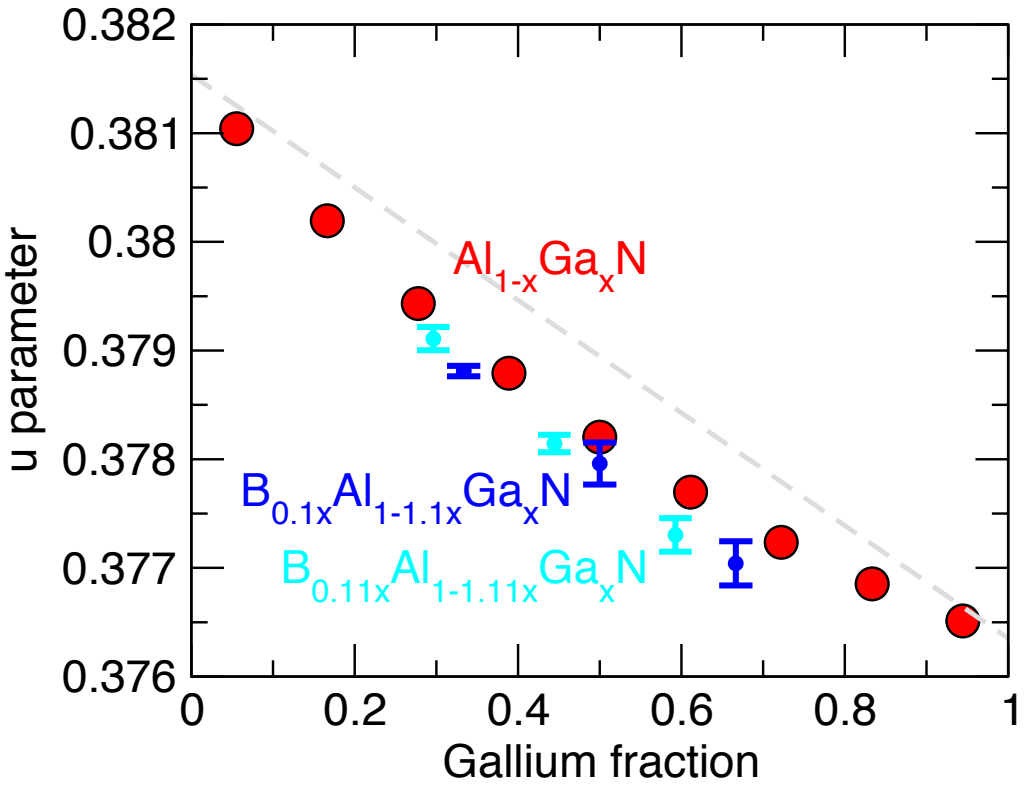

Figure 10.8. Structural u parameter as a function of the gallium fraction (x) for $Al_{1-x}Ga_xN$, $B_{0.11x}Al_{1-1.11x}Ga_xN$, and $B_{0.1x}Al_{1-1.1x}Ga_xN$ alloys. Boron addition reduces the u parameter compared to equal Ga content $Al_{1-x}Ga_xN$ alloys, which means that boron alloys with the same band gap will have lower u parameters.

10.3.5 Piezoelectric Coefficients and Spontaneous Polarization Constants

The piezoelectric coefficients and spontaneous polarization values for the BAlGaN alloy series have also been calculated. The values for AlN, GaN, and BN as calculated using the methods listed in this paper are shown in Table 10.2. There is strong agreement between this work and previous works on the spontaneous polarization constant, but discrepancies exist for the piezoelectric coefficients for GaN and BN. This work reports smaller values for GaN and larger values for BN than the previous work by Dreyer.[193,194] Dreyer's work used the HSE functional, and is likely more accurate than this paper. However, calculation with the HSE functional is prohibitively expensive for the larger alloy systems studied here.

Table 10.2. Spontaneous polarization (P_S), and piezoelectric coefficients for AlN, GaN, and BN calculated in this work using PBE with vdW relaxed structures and the hexagonal reference structure. Compared to previous literature values by Cyrus Dreyer's 2014 paper on BN[193], with sign error on P_S corrected, and Dreyer's 2016 paper on GaN and AlN.[194] Close agreement is achieved for the spontaneous polarization values, and rough agreement for the piezoelectric coefficients. Values predicted are smaller for GaN and larger for BN than those predicted by Dreyer. Note: the shown piezoelectric constants are the "proper" constants.

	This work (all in C/m^2)			Literature (all in C/m^2)		
Material	P_S	ε_{33}	ε_{31}	P_S	ε_{33}	ε_{31}
AlN	1.3367	1.494	-0.592	1.312	1.569	-0.676
GaN	1.3307	0.616	-0.364	1.351	1.02	-0.551
BN	2.1125	-1.231	0.491	2.174	-1.068	0.282

Table 10.3 shows the calculated spontaneous polarization constants and piezoelectric constants for BAlGaN alloys.

Table 10.3. Spontaneous polarization (P_S), and piezoelectric coefficients for BAlGaN alloys.

Material	P_S	ε_{33}	ε_{31}
$B_{0.056}Al_{0.5}Ga_{0.44}N$	1.347 ± .006	0.971 ± 0.030	-0.457 ± 0.007
$B_{0.056}Al_{0.44}Ga_{0.5}N$	1.332 ± .010	0.925 ± 0.006	-0.436 ± 0.007

Chapter 11 Machine Learning using Local Descriptors for Scintillator Prediction

The work from this chapter has been performed in collaboration with Ghanshyam Pilania of Los Alamos National Labs.

11.1 Introduction

Scintillators are a class of materials that emit light in the visible range after being struck by high energy, ionizing radiation. By combining a scintillator with a photodetector, the energy and intensity of radiation can be measured. An array of these scintillation counters can be used for radiation imaging. Scintillators thus have important applications in medical imaging, scientific research, and nuclear material detection.[199–201]

Physically, scintillators absorb radiation energy through the creation of electron-hole pairs, which then recombine to emit photons. Dopants are typically used as fast recombination centers, called luminescent centers, within a host material that is efficient at capturing ionizing radiation.

Ce^{3+} is commonly doped into materials to act as a luminescent center for scintillation due to its relatively fast 5d-4f transition.[202–204] Scintillation can be divided up into four main processes: energy conversion, thermalization, localization, and light emission. Energy conversion is the caption of ionizing radiation and the creation of "hot" electrons and holes within the host material. In thermalization, the "hot" electrons and holes relax to the band edges by giving energy to the crystal through inelastic processes. Localization is the subsequent transfer of those carriers to the luminescent centers. Thus, in order for scintillation to occur in a

Ce-activated scintillator, the Ce's 4f state (the ground state with the electronic configuration [Xe]$4f^n\,5d^0$) needs to lie within the band gap, slightly above the valence band, and the Ce's $5d_1$ state (the lowest excited state with configuration [Xe]$4f^{n-1}\,5d^1$) needs to lie slightly below the conduction band.[205–207] An initial, high-throughput, screening of potential host materials for Ce-activated scintillators can be performed using this requirement if the 4f and 5d energy levels of Ce in the crystal can be predicted. However, the energy level of Ce's $5d_1$ state is highly dependent upon the local bonding environment.

Previous work[208] performed by Ghanshyam Pilania et al. utilized machine learning on experimental databases created by Dorenbos[205,206] to predict the material parameters U, the 4f electron binding energy between Eu^{2+} and Eu^{3+}, and D, the crystal field depression, along with physical models to relate these properties to the 4f and $5d_1$ energy levels of Ce within a host. Figure 11.1 shows the relation between D and the 4f and 5d energy levels in a material.[208] Their work used only properties of the full host crystal and found that these were sufficient to describe 4f levels with reasonable accuracy (~0.14 eV RMSE) but were much less accurate for the prediction of $5d_1$ energy levels (~0.39 eV RMSE).

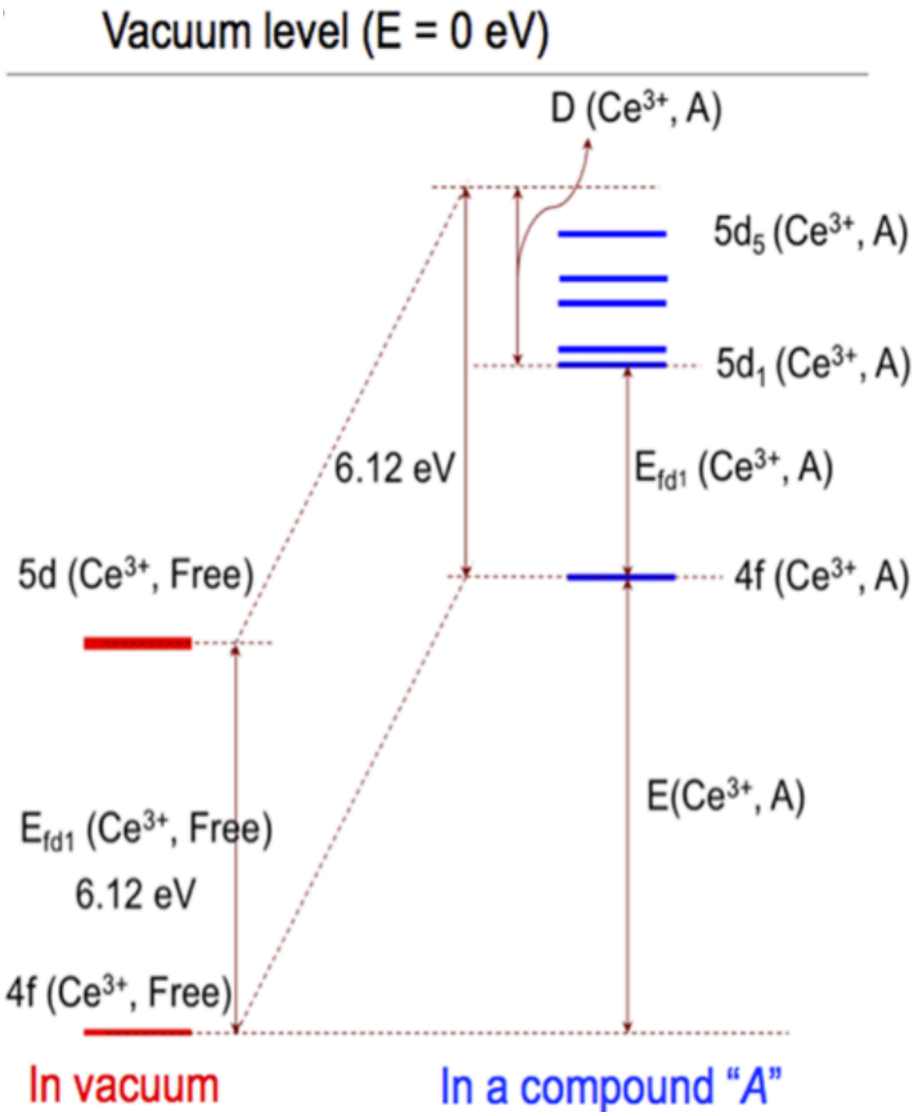

Figure 11.1. Schematic depiction of the change in 4f-shell and 5d-shell electron binding energies in Ce^{3+} when going from vacuum to a host environment "A". There is a significant lowering of the lowest energy 5d state relative to the 4f state, as well as a splitting of the 5d energy levels due to local bonding environment. Reprinted from the original paper.[208]

In order to improve upon the machine learning model from Pilania's 2018 work[208], a natural progression is to incorporate local bonding environment descriptors in addition to the bulk crystal properties used previously. This way the local environment dependence of the crystal field splitting can also be captured in the machine learning model. Using local environment descriptors also requires prediction of the Ce^{3+} doping site beforehand, making this a two-step optimization process.

11.2 Methodology

We used the experimental database created by Dorenbos[206] for training and testing of our model. To optimize the machine learning model prediction, we altered both the parameters for the Ce^{3+} doping site selection process and the local environment descriptors used as features in the machine learning step.

To select a doping site, we evaluated a penalty function over all crystallographically distinct sites in the crystal structure. For computational tractability for high-throughput calculations, it was assumed that Ce^{3+} would dope as a substitution and not interstitially or as a complex defect cluster. The following set of equations was used:

$P = |\Delta(\text{ionic radius})|*\alpha + |\Delta(\text{charge state})|*\beta$ when Ce^{3+} is larger, and

$P = |\Delta(\text{ionic radius})| + |\Delta(\text{charge state})|*\beta$ when Ce^{3+} is smaller

The Δ's measure property differences between Ce^{3+} and the site's native occupant. α is a penalty coefficient for a site being too small for Ce^{3+} instead of too large, and β is a penalty coefficient for a charge state difference between Ce^{3+} and the site's normal occupant. In the case of ties between sites, the site with the largest Voronoi volume was chosen.

For machine learning, we used Kernel Ridge Regression (KRR) with 8-fold cross validation to build our prediction model for the crystal field depression, D. To get more robust prediction from the small dataset, 100 models were trained for each parameter combination with different test/train splits and the average ± the standard deviation root mean squared error of the test and training sets were reported.[206]

The Matminer[209] code was used for all local environment descriptors except for the crystal field splitting spread, which was calculated using the point charge model implemented in the Mantid[210] code.

11.3 Results and Discussion

Testing using the AGNI and Gaussian Symmetry functions (described below) found optimal values of α=3.0 and β=0.2 Å for the doping site selection process. Using these parameters, the site with the smallest penalty for each host material was used in all following results.

Figure 11.2 shows the root mean squared error (RMSE) of machine learning models trained on either only the best two performing bulk crystal descriptors (the best result from Pilania's 2018 work[208]), PBE band gap and average electronegativity,[208] or those two plus a local environment descriptor. The best performing descriptors are AGNI Fingerprint and Gaussian Symmetry Functions, which both combine radial and angular information. The Voronoi fingerprint, Gaussian Angular Fourier Series (AFS), and OP site fingerprint all over-fit the training data using default settings. The crystal field splitting spread, Gaussian Radial Distribution Function (RDF), Coordination Numbers, and Local Difference in Electronegativity all provide little or no improvement in model predictive power.

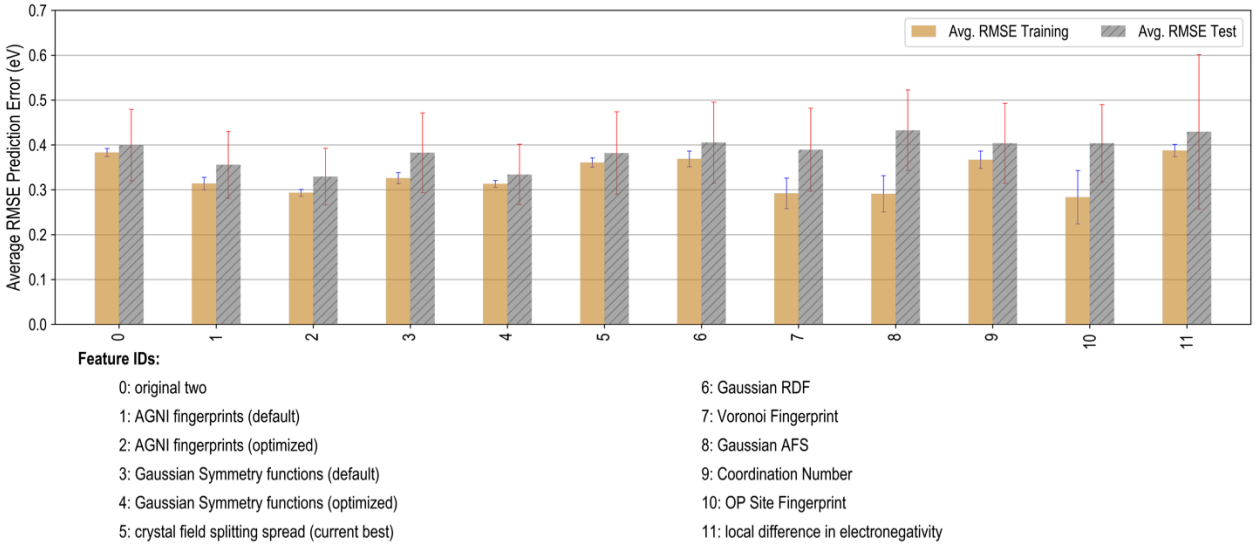

Figure 11.2. Average RMSE of crystal field depression, D, for the training (gold bar) and test (striped grey bar) datasets using either the best two bulk crystal descriptors (PBE band gap and average electronegativity) or a local environment descriptor in addition to the two bulk descriptors. The best two performing descriptors are Gaussian Symmetry functions and AGNI fingerprints.

The AGNI Fingerprint and Gaussian Symmetry Function descriptors are both optimized when restricted to within 3.75 Å of the doping site. This is due to crystal field depression being dominated by nearest neighbor bonding interactions.

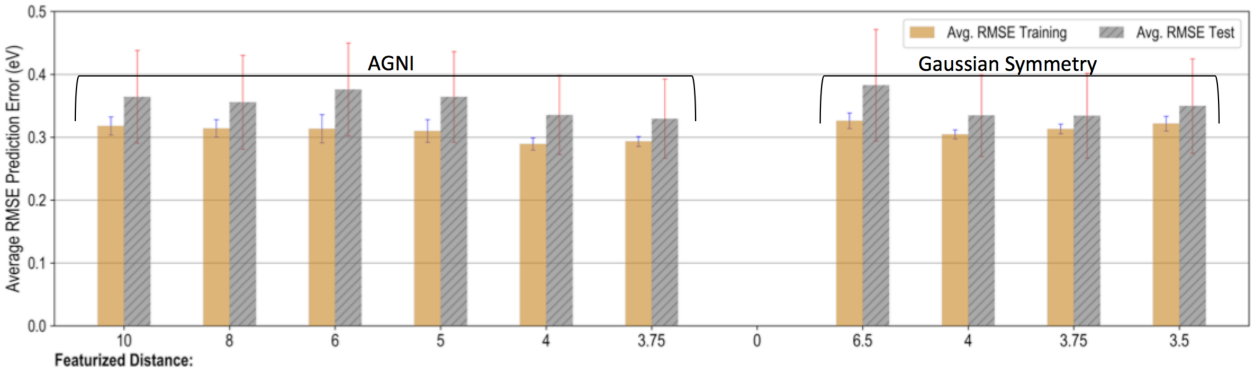

Figure 11.3. Average RMSE of crystal field depression, D, for the training (gold bar) and test (striped grey bar) datasets using the AGNI Fingerprints and Gaussian Symmetry functions restricted to different maximum distances from the doping site center. Both perform optimally at 3.75Å.

Testing of the AGNI Fingerprint and Gaussian Symmetry Functions radial descriptors separately reveals that they provide all of the useful information for the machine learning algorithm. Both descriptors lack rotational invariance for predicting across diverse crystal structures. Due to this and the wide variety of crystal space groups and orientations in the dataset, the angular descriptors cannot provide meaningful data to the model. This challenge could potentially be overcome by careful data duplication and rotation in the training set.

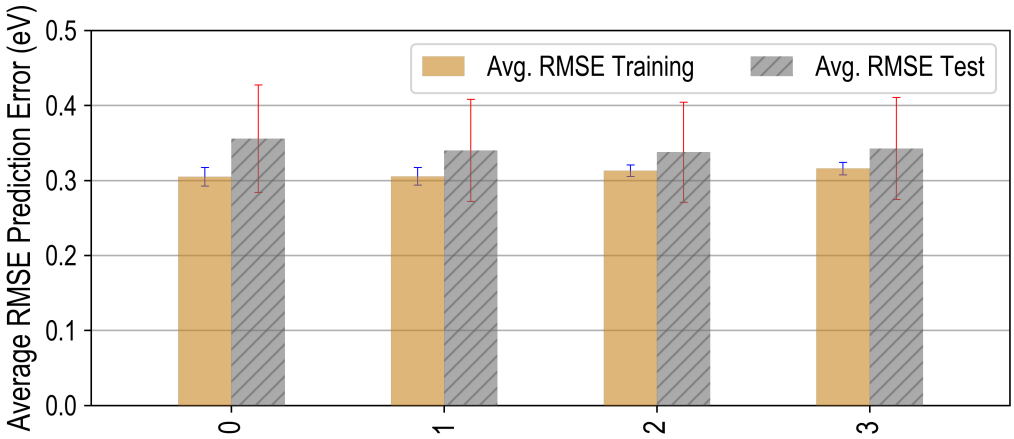

Feature IDs:

0: AGNI fingerprints d=3.75 Angstroms

1: AGNI fingerprints d=3.75 Angstroms and no directional data

2: Gaussian Symmetry functions d=3.75 Angstroms

3: Gaussian Symmetry functions d=3.75 Angstroms and no directional data

Figure 11.4. Average RMSE of crystal field depression, D, for the training (gold bar) and test (striped grey bar) datasets using the AGNI Fingerprints and Gaussian Symmetry functions with and without angular components included.

Rotationally invariant descriptors such as the Voronoi fingerprint or the crystal field splitting spread might also be able to be optimized and used to overcome the challenges of incorporating angular information for crystal systems with different space groups and orientations. The Voronoi fingerprint is currently over-fit, but performs very well on the training set and is rotationally invariant. The crystal field splitting spread is also rotationally invariant but currently offers little improvement even in training accuracy. There are two likely causes for this. The first is that there is a difference between the crystal field splitting spread, $5d_{5,A} - 5d_{1,A}$, and the crystal field depression, $((5d_{vacuum} - 4f_{vacuum}) + 4f_A) - 5d_{1,A}$), that may or may not be systematic to other properties included in the model features. The second is that the substitution of Ce^{3+} onto a dopant site will cause a local deformation of the surrounding atomic structure, as well as possibly the surrounding charge states in the case of ionic charge mismatch. These effects are not currently taken into account when using the point charge model to calculate the predicted crystal field splitting spread. Two possible ways to deal with this are: removing cases that had

high penalty functions from the doping site selection and only training on the cases with little structural / ionic distortion expected, or using force fields or rough (under-converged) DFT relaxations to get approximately correct atomic positions for the point charge model. The second requires much more calculation, but would also potentially allow for more accurate charges in the point charge model than the current formal oxidation states used in the model.

11.4 Conclusions and Future Work

Local radial information encoded in the AGNI and Gaussian Symmetry function descriptors can improve the prediction of Ce^{3+} crystal field depression in a host material from ~0.39 eV RMSE with only host band gap and average electronegativity of elements to ~0.34 eV RMSE.

Non-radial structural information is poorly compared across diverse crystal structures by the default Matminer implementations. Future improvements to the model are expected to come from data duplication and rotation for the AGNI Fingerprint and Gaussian Symmetry function descriptors, through inclusion of rotationally invariant descriptors such as the Voronoi Fingerprint, or through improvements to the crystal field splitting model beyond the unrelaxed point charge model currently used.

11.5 Acknowledgements

This work was made possible by the open source projects Scikit-Learn, Pandas, Matminer[209], Pymatgen, Materials Project, and Mantid[210].

Bibliography

1. Hohenberg, P. & Kohn, W. Inhomogenous Electron Gas. *Phys. Rev.* **136,** 66–71 (1964).
2. Kohn, W. & Sham, L. J. Self-consistent equations including exchange and correlation effects. *Phys. Rev.* **140,** A1133 (1965).
3. Hybertsen, M. S. & Louie, S. G. Electron correlation in semiconductors and insulators: Band gaps and quasiparticle energies. *Phys. Rev. B* **34,** 5390 (1986).
4. Slater, J. C. A simplification of the Hartree-Fock method. *Phys. Rev.* **81,** 385 (1951).
5. Ceperley, D. M. & Alder, B. J. Ground state of the electron gas by a stochastic method. *Phys. Rev. Lett.* **45,** 566 (1980).
6. Perdew, J. P. & Zunger, A. Self-interaction correction to density-functional approximations for many-electron systems. *Phys. Rev. B* **23,** 5048–5079 (1981).
7. Perdew, J., Burke, K. & Ernzerhof, M. Generalized gradient approximation made simple. *Phys. Rev. Lett.* **77,** 3865–3868 (1996).
8. Perdew, J. P. & Levy, M. Physical content of the exact Kohn-Sham orbital energies: band gaps and derivative discontinuities. *Phys. Rev. Lett.* **51,** 1884 (1983).
9. Sham, L. J. & Schlüter, M. Density-functional theory of the energy gap. *Phys. Rev. Lett.* **51,** 1888 (1983).
10. Fock, V. Näherungsmethode zur Lösung des quantenmechanischen Mehrkörperproblems. *Zeitschrift für Phys.* **61,** 126–148 (1930).
11. Perdew, J. P., Ernzerhof, M. & Burke, K. Rationale for mixing exact exchange with density functional approximations. *J. Chem. Phys.* **105,** 9982–9985 (1996).
12. Ernzerhof, M. & Scuseria, G. E. Assessment of the Perdew–Burke–Ernzerhof exchange-correlation functional. *J. Chem. Phys.* **110,** 5029–5036 (1999).
13. Adamo, C. & Barone, V. Toward reliable density functional methods without adjustable parameters: The PBE0 model. *J. Chem. Phys.* **110,** 6158–6170 (1999).
14. Heyd, J., Scuseria, G. E. & Ernzerhof, M. Hybrid functionals based on a screened Coulomb potential. *J. Chem. Phys.* **118,** 8207–8215 (2003).
15. Heyd, J., Scuseria, G. E. & Ernzerhof, M. Erratum: Hybrid functionals based on a screened Coulomb potential (Journal of Chemical Physics (2003) 118 (8207)). *J. Chem. Phys.* **124,** 2005–2006 (2006).
16. Krukau, A. V., Vydrov, O. A., Izmaylov, A. F. & Scuseria, G. E. Influence of the exchange screening parameter on the performance of screened hybrid functionals. *J. Chem. Phys.* **125,** 224106 (2006).
17. Zunger, A., Wei, S.-H., Ferreira, L. G. & Bernard, J. E. Special quasirandom structures. *Phys. Rev. Lett.* **65,** 353 (1990).
18. van de Walle, A. *et al.* Efficient stochastic generation of special quasirandom structures. *Calphad* **42,** 13–18 (2013).
19. Jiang, C. & Uberuaga, B. P. Efficient Ab initio Modeling of Random Multicomponent Alloys. *Phys. Rev. Lett.* **116,** 105501 (2016).
20. Goodenough, J. B. & Kim, Y. Challenges for Rechargeable Li Batteries †. *Chem. Mater.*

22, 587–603 (2010).
21. Armand, M. & Tarascon, J.-M. Building better batteries. *Nature* **451,** 652–657 (2008).
22. Bruce, P. G., Freunberger, S. A., Hardwick, L. J. & Tarascon, J.-M. Li–O2 and Li–S batteries with high energy storage. *Nat. Mater.* **11,** 19–29 (2012).
23. Teng, S., Tan, J. & Tiwari, A. Recent developments in garnet based solid state electrolytes for thin film batteries. *Curr. Opin. Solid State Mater. Sci.* **18,** 29–38 (2014).
24. Dudney, N. J., West, W. C. & Nanda, J. Handbook of Solid-state Batteries and Supercapacitors. (2014).
25. Takada, K. Progress and prospective of solid-state lithium batteries. *Acta Mater.* **61,** 759–770 (2013).
26. Murugan, R., Thangadurai, V. & Weppner, W. Fast Lithium Ion Conduction in Garnet-Type Li7La3Zr2O12. *Angew. Chemie Int. Ed.* **46,** 7778–7781 (2007).
27. Tan, J. & Tiwari, A. Synthesis of Cubic Phase Li7La3Zr2O12 Electrolyte for Solid-State Lithium-Ion Batteries. *Electrochem. Solid-State Lett.* **15,** A37 (2012).
28. Xu, Y.-N. & Ching, W. Y. Electronic structure of yttrium aluminum garnet (Y3Al5O12). *Phys. Rev. B* **59,** 10530–10535 (1999).
29. Nemori, H. *et al.* Stability of garnet-type solid electrolyte LixLa3A2-yByO12 (A=Nb or Ta, B=Sc or Zr). *Solid State Ionics* **282,** 7–12 (2015).
30. Kim, Y. *et al.* Electrochemical Stability of Li6.5La3Zr1.5M0.5O12 (M = Nb or Ta) against Metallic Lithium. *Front. Energy Res.* **4,** 1–7 (2016).
31. Xu, K. Electrolytes and Interphases in Li-Ion Batteries and Beyond. *Chem. Rev.* **114,** 11503–11618 (2014).
32. Cheng, L. *et al.* Accelerating Electrolyte Discovery for Energy Storage with High-Throughput Screening. *J. Phys. Chem. Lett.* **6,** 283–291 (2015).
33. Korth, M. Large-scale virtual high-throughput screening for the identification of new battery electrolyte solvents: evaluation of electronic structure theory methods. *Phys. Chem. Chem. Phys.* **16,** 7919–7926 (2014).
34. Kumar, N. & Siegel, D. J. Interface-Induced Renormalization of Electrolyte Energy Levels in Magnesium Batteries. *J. Phys. Chem. Lett.* **7,** 874–881 (2016).
35. Bard, A. J. & Faulkner, L. R. Fundamentals and applications. *Electrochem. Methods* **2,** 482 (2001).
36. Miara, L. J., Richards, W. D., Wang, Y. E. & Ceder, G. First-principles studies on cation dopants and electrolyte|cathode interphases for lithium garnets. *Chem. Mater.* **27,** 4040–4047 (2015).
37. Zhu, Y., He, X. & Mo, Y. Origin of Outstanding Stability in the Lithium Solid Electrolyte Materials: Insights from Thermodynamic Analyses Based on First-Principles Calculations. *ACS Appl. Mater. Interfaces* **7,** 23685–23693 (2015).
38. Thompson, T. *et al.* Tetragonal vs. cubic phase stability in Al – free Ta doped Li 7 La 3 Zr 2 O 12 (LLZO). *J. Mater. Chem. A* **2,** 13431 (2014).
39. A. R., H. Simple Method to Determine Electronic and Ionic Components of the Conductivity in Mixed Conductors: A Review. *Ionics (Kiel).* **8,** 300–313 (2002).
40. Yu, S. *et al.* Elastic Properties of the Solid Electrolyte Li 7 La 3 Zr 2 O 12 (LLZO). *Chem. Mater.* **28,** 197–206 (2016).
41. Davis, E. A. & Mott, N. F. Conduction in non-crystalline systems V. Conductivity, optical absorption and photoconductivity in amorphous semiconductors. *Philos. Mag.* **22,** 0903–0922 (1970).

42. Kresse, G. & Furthmüller, J. Efficient iterative schemes for ab initio total-energy calculations using a plane-wave basis set. *Phys. Rev. B* **54,** 11169–11186 (1996).
43. Shishkin, M. & Kresse, G. Implementation and performance of the frequency-dependent GW method within the PAW framework. *Phys. Rev. B* **74,** 035101 (2006).
44. Emly, A., Kioupakis, E. & Van der Ven, A. Phase Stability and Transport Mechanisms in Antiperovskite Li 3 OCl and Li 3 OBr Superionic Conductors. *Chem. Mater.* **25,** 4663–4670 (2013).
45. Xie, H., Alonso, J. A., Li, Y., Fernández-Díaz, M. T. & Goodenough, J. B. Lithium Distribution in Aluminum-Free Cubic Li 7 La 3 Zr 2 O 12. *Chem. Mater.* **23,** 3587–3589 (2011).
46. Fuchs, F., Furthmüller, J., Bechstedt, F., Shishkin, M. & Kresse, G. Quasiparticle band structure based on a generalized Kohn-Sham scheme. *Phys. Rev. B* **76,** 115109 (2007).
47. Ohta, S., Kobayashi, T. & Asaoka, T. High lithium ionic conductivity in the garnet-type oxide Li7−X La3(Zr2−X, NbX)O12 (X=0–2). *J. Power Sources* **196,** 3342–3345 (2011).
48. Rangasamy, E., Wolfenstine, J. & Sakamoto, J. The role of Al and Li concentration on the formation of cubic garnet solid electrolyte of nominal composition Li7La3Zr2O12. *Solid State Ionics* **206,** 28–32 (2012).
49. Huang, M. *et al.* Effect of sintering temperature on structure and ionic conductivity of Li7−xLa3Zr2O12−0.5x (x=0.5~0.7) ceramics. *Solid State Ionics* **204–205,** 41–45 (2011).
50. Thompson, T. *et al.* A Tale of Two Sites: On Defining the Carrier Concentration in Garnet-Based Ionic Conductors for Advanced Li Batteries. *Adv. Energy Mater.* **5,** 1500096 (2015).
51. Han, F., Zhu, Y., He, X., Mo, Y. & Wang, C. Electrochemical Stability of Li 10 GeP 2 S 12 and Li 7 La 3 Zr 2 O 12 Solid Electrolytes. *Adv. Energy Mater.* **6,** 1501590 (2016).
52. Wolf, S. A. *et al.* Spintronics: A Spin-Based Electronics Vision for the Future. *Science (80-.).* **294,** 1488 LP-1495 (2001).
53. Jamet, M. *et al.* High-Curie-temperature ferromagnetism in self-organized Ge1−xMnx nanocolumns. *Nat. Mater.* **5,** 653–659 (2006).
54. MacDonald, A. H., Schiffer, P. & Samarth, N. Ferromagnetic semiconductors: moving beyond (Ga,Mn)As. *Nat. Mater.* **4,** 195–202 (2005).
55. Zutic, I., Fabian, J. & Erwin, S. C. Bipolar spintronics: Fundamentals and applications. *IBM J. Res. Dev.* **50,** 121–139 (2006).
56. Žutić, I., Fabian, J. & Das Sarma, S. Spintronics: Fundamentals and applications. *Rev. Mod. Phys.* **76,** 323–410 (2004).
57. Dobrowolska, M. *et al.* Controlling the Curie temperature in (Ga,Mn)As through location of the Fermi level within the impurity band. *Nat. Mater.* **11,** 444 (2012).
58. Richardella, A. *et al.* Visualizing Critical Correlations Near the Metal-Insulator Transition in Ga1-xMnxAs. *Science (80-.).* **327,** 665–669 (2010).
59. Sawicki, M. *et al.* Experimental probing of the interplay between ferromagnetism and localization in (Ga, Mn)As. *Nat. Phys.* **6,** 22 (2009).
60. Dietl, T., Ohno, H., Matsukura, F., Cibert, J. & Ferrand, D. Zener Model Description of Ferromagnetism in Zinc-Blende Magnetic Semiconductors. *Science (80-.).* **287,** 1019 LP-1022 (2000).
61. Dietl, T. Ferromagnetic semiconductors. *Semicond. Sci. Technol.* **17,** 377–392 (2002).
62. Dietl, T. A ten-year perspective on dilute magnetic semiconductors and oxides. *Nat. Mater.* **9,** 965 (2010).

63. Edmonds, K. W. *et al.* Mn Interstitial Diffusion in (Ga, Mn)As. *Phys. Rev. Lett.* **92,** 037201 (2004).
64. Blinowski, J. & Kacman, P. Spin interactions of interstitial Mn ions in ferromagnetic GaMnAs. *Phys. Rev. B* **67,** 121204 (2003).
65. Yu, K. M. *et al.* Effect of the location of Mn sites in ferromagnetic Ga1-xMnxAs on its Curie Temperature. *Phys. Rev. B* **65,** 201303 (2002).
66. Jungwirth, T. *et al.* Prospects for high temperature ferromagnetism in (Ga,Mn)As semiconductors. *Phys. Rev. B* **72,** 165204 (2005).
67. Wang, M. *et al.* Achieving high Curie temperature in (Ga,Mn)As. *Appl. Phys. Lett.* **93,** 132103 (2008).
68. Ranmohotti, K. G. S. *et al.* Coexistence of High- T_c Ferromagnetism and *n* -Type Electrical Conductivity in $FeBi_2Se_4$. *J. Am. Chem. Soc.* **137,** 691–698 (2015).
69. Djieutedjeu, H. *et al.* Structural-Distortion-Driven Cooperative Magnetic and Semiconductor-to-Insulator Transitions in Ferromagnetic FeSb2Se4. *Angew. Chemie Int. Ed.* **49,** 9977–9981 (2010).
70. Djieutedjeu, H., Olvera, A., Page, A., Uher, C. & Poudeu, P. F. P. High- T_c Ferromagnetism and Electron Transport in p-Type $Fe_{1-x}Sn_xSb_2Se_4$ Semiconductors. *Inorg. Chem.* **4,** 151020155116004 (2015).
71. Blöchl, P. E. Projector augmented-wave method. *Phys. Rev. B* **50,** 17953–17979 (1994).
72. Kresse, G. & Joubert, D. From ultrasoft pseudopotentials to the projector augmented-wave method. *Phys. Rev. B* **59,** 1758–1775 (1999).
73. Kresse, G. & Hafner, J. Ab initio molecular dynamics for liquid metals. *Phys. Rev. B* **47,** 558–561 (1993).
74. Kresse, G. & Hafner, J. Ab initio molecular-dynamics simulation of the liquid-metal–amorphous-semiconductor transition in germanium. *Phys. Rev. B* **49,** 14251–14269 (1994).
75. Kresse, G. & Furthmüller, J. Efficiency of ab-initio total energy calculations for metals and semiconductors using a plane-wave basis set. *Comput. Mater. Sci.* **6,** 15–50 (1996).
76. Lee, M. M., Teuscher, J., Miyasaka, T., Murakami, T. N. & Snaith, H. J. Efficient Hybrid Solar Cells Based on Meso-Superstructured Organometal Halide Perovskites. *Science (80-.).* **338,** 643–647 (2012).
77. Joshi, R. A., Taur, V. S. & Sharma, R. Effect of annealing on conversion efficiency of nanostructured CdS/CuInSe2 heterojunction thin film solar cell prepared by chemical ion exchange route at room temperature. *Mater. Res. Bull.* **47,** 2206–2211 (2012).
78. Jackson, P. *et al.* New world record efficiency for Cu(In,Ga)Se2 thin-film solar cells beyond 20%. *Prog. Photovoltaics Res. Appl.* **19,** 894–897 (2011).
79. Nakada, T. & Mizutani, M. 18% Efficiency Cd-Free Cu(In, Ga)Se2 Thin-Film Solar Cells Fabricated Using Chemical Bath Deposition (CBD)-ZnS Buffer Layers. *Jpn. J. Appl. Phys.* **41,** L165–L167 (2002).
80. Shin, D., Saparov, B. & Mitzi, D. B. Defect Engineering in Multinary Earth-Abundant Chalcogenide Photovoltaic Materials. *Adv. Energy Mater.* **7,** 1602366 (2017).
81. Hao, F., Stoumpos, C. C., Cao, D. H., Chang, R. P. H. & Kanatzidis, M. G. Lead-free solid-state organic–inorganic halide perovskite solar cells. *Nat. Photonics* **8,** 489–494 (2014).
82. Stranks, S. D. & Snaith, H. J. Metal-halide perovskites for photovoltaic and light-emitting devices. *Nat. Nanotechnol.* **10,** 391–402 (2015).

83. Battaglia, C., Cuevas, A. & De Wolf, S. High-efficiency crystalline silicon solar cells: status and perspectives. *Energy Environ. Sci.* **9,** 1552–1576 (2016).
84. Masuko, K. *et al.* Achievement of More Than 25% Conversion Efficiency With Crystalline Silicon Heterojunction Solar Cell. *IEEE J. Photovoltaics* **4,** 1433–1435 (2014).
85. Kayes, B. M. *et al.* 27.6% Conversion efficiency, a new record for single-junction solar cells under 1 sun illumination. in *2011 37th IEEE Photovoltaic Specialists Conference* 000004–000008 (IEEE, 2011). doi:10.1109/PVSC.2011.6185831
86. Liu, M., Johnston, M. B. & Snaith, H. J. Efficient planar heterojunction perovskite solar cells by vapour deposition. *Nature* **501,** 395–398 (2013).
87. Ball, J. M., Lee, M. M., Hey, A. & Snaith, H. J. Low-temperature processed meso-superstructured to thin-film perovskite solar cells. *Energy Environ. Sci.* **6,** 1739 (2013).
88. Zhou, H. *et al.* Interface engineering of highly efficient perovskite solar cells. *Science (80-.).* **345,** 542–546 (2014).
89. Todorov, T. K., Reuter, K. B. & Mitzi, D. B. High-Efficiency Solar Cell with Earth-Abundant Liquid-Processed Absorber. *Adv. Mater.* **22,** E156–E159 (2010).
90. Ito, K. & Nakazawa, T. Electrical and Optical Properties of Stannite-Type Quaternary Semiconductor Thin Films. *Jpn. J. Appl. Phys.* **27,** 2094–2097 (1988).
91. Lee, Y. S. *et al.* Cu 2 ZnSnSe 4 Thin-Film Solar Cells by Thermal Co-evaporation with 11.6% Efficiency and Improved Minority Carrier Diffusion Length. *Adv. Energy Mater.* **5,** 1401372 (2015).
92. Wang, W. *et al.* Device Characteristics of CZTSSe Thin-Film Solar Cells with 12.6% Efficiency. *Adv. Energy Mater.* **4,** 1301465 (2014).
93. Katagiri, H. *et al.* Development of CZTS-based thin film solar cells. *Thin Solid Films* **517,** 2455–2460 (2009).
94. Chen, S., Walsh, A., Gong, X.-G. & Wei, S.-H. Classification of Lattice Defects in the Kesterite Cu 2 ZnSnS 4 and Cu 2 ZnSnSe 4 Earth-Abundant Solar Cell Absorbers. *Adv. Mater.* **25,** 1522–1539 (2013).
95. Mostofi, A. A. *et al.* wannier90: A tool for obtaining maximally-localised Wannier functions. *Comput. Phys. Commun.* **178,** 685–699 (2008).
96. Albrecht, S., Reining, L., Del Sole, R. & Onida, G. Ab Initio Calculation of Excitonic Effects in the Optical Spectra of Semiconductors. *Phys. Rev. Lett.* **80,** 4510–4513 (1998).
97. Rohlfing, M. & Louie, S. G. Electron-Hole Excitations in Semiconductors and Insulators. *Phys. Rev. Lett.* **81,** 2312–2315 (1998).
98. Zhang, C. *et al.* An Ultrathin, Smooth, and Low-Loss Al-Doped Ag Film and Its Application as a Transparent Electrode in Organic Photovoltaics. *Adv. Mater.* **26,** 5696–5701 (2014).
99. Hilfiker, J. N. *et al.* Survey of methods to characterize thin absorbing films with Spectroscopic Ellipsometry. *Thin Solid Films* **516,** 7979–7989 (2008).
100. Tauc, J., Grigorovici, R. & Vancu, A. Optical Properties and Electronic Structure of Amorphous Germanium. *Phys. status solidi* **15,** 627–637 (1966).
101. Shockley, W. & Queisser, H. J. Detailed Balance Limit of Efficiency of p-n Junction Solar Cells. *J. Appl. Phys.* **32,** 510–519 (1961).
102. Rühle, S. Tabulated values of the Shockley–Queisser limit for single junction solar cells. *Sol. Energy* **130,** 139–147 (2016).
103. Shi, G. & Kioupakis, E. Electronic and Optical Properties of Nanoporous Silicon for Solar-Cell Applications. *ACS Photonics* **2,** 208–215 (2015).

104. Pauling, L. & Hultgren, R. The Crystal Structure of Sulvanite , Cu3VS4. *Zeitschrift für Krist.* **84,** 204–212 (1933).
105. Dubrovskii, G. B. Optical properties of CdTe. *Sov. PHYSICS-SOLID STATE* **3,** 943–946 (1961).
106. Akinlami, J. O. & Ashamu, A. O. Optical properties of GaAs. *J. Semicond.* **34,** 032002 (2013).
107. Minoura, S. *et al.* Dielectric function of Cu(In, Ga)Se2-based polycrystalline materials. *J. Appl. Phys.* **113,** 0–14 (2013).
108. SEOL, J., LEE, S., LEE, J., NAM, H. & KIM, K. Electrical and optical properties of CuZnSnS thin films prepared by rf magnetron sputtering process. *Sol. Energy Mater. Sol. Cells* **75,** 155–162 (2003).
109. Ziang, X. *et al.* Refractive index and extinction coefficient of CH_3NH_3PbI_3 studied by spectroscopic ellipsometry. *Opt. Mater. Express* **5,** 29 (2014).
110. Yu, L. & Zunger, A. Identification of Potential Photovoltaic Absorbers Based on First-Principles Spectroscopic Screening of Materials. *Phys. Rev. Lett.* **108,** 068701 (2012).
111. Bercx, M., Sarmadian, N., Saniz, R., Partoens, B. & Lamoen, D. First-principles analysis of the spectroscopic limited maximum efficiency of photovoltaic absorber layers for CuAu-like chalcogenides and silicon. *Phys. Chem. Chem. Phys.* **18,** 20542–20549 (2016).
112. Sun, Y.-Y., Agiorgousis, M. L., Zhang, P. & Zhang, S. Chalcogenide Perovskites for Photovoltaics. *Nano Lett.* **15,** 581–585 (2015).
113. Tranchitella, L. J., Chen, B.-H., Fettinger, J. C. & Eichhorn, B. W. Structural Evolutions in the Sr1–xBax ZrSe3 Series. *J. Solid State Chem.* **130,** 20 (1997).
114. Aslanov, L. A. Selenides of the type ABSe3. *Russ. J. Inorg. Chem* **9,** 1090 (1969).
115. Aslanov, L. A. ABSe3-Type Selenides (in Russian). *Zhur. Neorg. Khim.* **9,** 2022 (1964).
116. Kubelka, P. Ein Beitrag zur Optik der Farbanstriche (Contribution to the optic of paint). *Zeitschrift fur Tech. Phys.* **12,** 593–601 (1931).
117. Tsai, M.-H. & Yeh, J.-W. High-Entropy Alloys: A Critical Review. *Mater. Res. Lett.* **2,** 107–123 (2014).
118. Miracle, D. B. High-Entropy Alloys: A Current Evaluation of Founding Ideas and Core Effects and Exploring "Nonlinear Alloys". *JOM* **69,** 2130–2136 (2017).
119. Praveen, S. & Kim, H. S. High-Entropy Alloys: Potential Candidates for High-Temperature Applications – An Overview. *Adv. Eng. Mater.* **20,** 1700645 (2018).
120. Gludovatz, B. *et al.* A fracture-resistant high-entropy alloy for cryogenic applications. *Science (80-.).* **345,** 1153 LP-1158 (2014).
121. Zhang, F. *et al.* Polymorphism in a high-entropy alloy. *Nat. Commun.* **8,** 15687 (2017).
122. Gild, J. *et al.* High-entropy fluorite oxides. *J. Eur. Ceram. Soc.* **38,** 3578–3584 (2018).
123. Gild, J. *et al.* High-Entropy Metal Diborides: A New Class of High-Entropy Materials and a New Type of Ultrahigh Temperature Ceramics. *Sci. Rep.* **6,** 37946 (2016).
124. Rost, C. M. *et al.* Entropy-stabilized oxides. *Nat. Commun.* **6,** 8485 (2015).
125. Goodenough, J. B. Metallic oxides. *Prog. Solid State Chem.* **5,** 145–399 (1971).
126. Imada, M., Fujimori, A. & Tokura, Y. Metal-insulator transitions. *Rev. Mod. Phys.* **70,** 1039–1263 (1998).
127. Martin, L. W., Chu, Y.-H. & Ramesh, R. Advances in the growth and characterization of magnetic, ferroelectric, and multiferroic oxide thin films. *Mater. Sci. Eng. R Reports* **68,** 89–133 (2010).
128. Ramirez, A. P., Hayashi, A., Cava, R. J., Siddharthan, R. & Shastry, B. S. Zero-point

entropy in ‘spin ice’. *Nature* **399,** 333–335 (1999).
129. Braun, J. L. *et al.* Charge-Induced Disorder Controls the Thermal Conductivity of Entropy-Stabilized Oxides. *Adv. Mater.* **30,** 1805004 (2018).
130. Rost, C. M., Rak, Z., Brenner, D. W. & Maria, J.-P. Local structure of the Mg x Ni x Co x Cu x Zn x O(x =0.2) entropy-stabilized oxide: An EXAFS study. *J. Am. Ceram. Soc.* **100,** 2732–2738 (2017).
131. Rák, Z., Maria, J.-P. & Brenner, D. W. Evidence for Jahn-Teller compression in the (Mg, Co, Ni, Cu, Zn)O entropy-stabilized oxide: A DFT study. *Mater. Lett.* **217,** 300–303 (2018).
132. AU - Sivakumar, S., AU - Zwier, E., AU - Meisenheimer, P. B. & AU - Heron, J. T. Bulk and Thin Film Synthesis of Compositionally Variant Entropy-stabilized Oxides. *JoVE* e57746 (2018). doi:doi:10.3791/57746
133. Meisenheimer, P. B., Kratofil, T. J. & Heron, J. T. Giant Enhancement of Exchange Coupling in Entropy-Stabilized Oxide Heterostructures. *Sci. Rep.* **7,** 13344 (2017).
134. Bérardan, D., Franger, S., Meena, A. K. & Dragoe, N. Room temperature lithium superionic conductivity in high entropy oxides. *J. Mater. Chem. A* **4,** 9536–9541 (2016).
135. Bérardan, D., Franger, S., Dragoe, D., Meena, A. K. & Dragoe, N. Colossal dielectric constant in high entropy oxides. *Phys. status solidi – Rapid Res. Lett.* **10,** 328–333 (2016).
136. Shoemaker, D. P. & Seshadri, R. Total-scattering descriptions of local and cooperative distortions in the oxide spinel Mg1-xCuxCr2O4 with dilute Jahn-Teller ions. *Phys. Rev. B* **82,** 214107 (2010).
137. Berardan, D., Meena, A. K. K., Franger, S., Herrero, C. & Dragoe, N. Controlled Jahn-Teller distortion in (MgCoNiCuZn)O-based high entropy oxides. *J. Alloys Compd.* **704,** 693–700 (2017).
138. Keen, D. A. & Goodwin, A. L. The crystallography of correlated disorder. *Nature* **521,** 303 (2015).
139. Weisbuch, C. *et al.* The efficiency challenge of nitride light-emitting diodes for lighting. *Phys. status solidi* **212,** 899–913 (2015).
140. Shen, Y. C. *et al.* Auger recombination in InGaN measured by photoluminescence. *Appl. Phys. Lett.* **91,** 141101 (2007).
141. Kioupakis, E., Steiauf, D., Rinke, P., Delaney, K. T. & Van de Walle, C. G. First-principles calculations of indirect Auger recombination in nitride semiconductors. *Phys. Rev. B* **92,** 035207 (2015).
142. Gardner, N. F. *et al.* Blue-emitting InGaN–GaN double-heterostructure light-emitting diodes reaching maximum quantum efficiency above 200A⁄cm2. *Appl. Phys. Lett.* **91,** 243506 (2007).
143. Okur, S. *et al.* Internal quantum efficiency and carrier dynamics in semipolar (20-21) InGaN/GaN light-emitting diodes. *Opt. Express* **25,** 2178 (2017).
144. David, A. *et al.* Carrier distribution in (0001)InGaN⁄GaN multiple quantum well light-emitting diodes. *Appl. Phys. Lett.* **92,** 053502 (2008).
145. Laubsch, A., Sabathil, M., Baur, J., Peter, M. & Hahn, B. High-Power and High-Efficiency InGaN-Based Light Emitters. *IEEE Trans. Electron Devices* **57,** 79–87 (2010).
146. Forghani, K. *et al.* GaAs1−y−zPyBiz, an alternative reduced band gap alloy system lattice-matched to GaAs. *Appl. Phys. Lett.* **105,** 111101 (2014).
147. Janotti, A., Wei, S.-H. & Zhang, S. B. Theoretical study of the effects of isovalent coalloying of Bi and N in GaAs. *Phys. Rev. B* **65,** 115203 (2002).

148. Petkov, V., Gateshki, M., Choi, J., Gillan, E. G. & Ren, Y. Structure of nanocrystalline GaN from X-ray diffraction, Rietveld and atomic pair distribution function analyses. *J. Mater. Chem.* **15,** 4654 (2005).
149. Paszkowicz, W., Černý, R. & Krukowski, S. Rietveld refinement for indium nitride in the 105–295 K range. *Powder Diffr.* **18,** 114–121 (2003).
150. Xu, Y. & Ching, W. Y. Electronic, optical, and structural properties of some wurtzite crystals. *Phys. Rev. B* **48,** 4335–4351 (1993).
151. Ougazzaden, A. *et al.* BGaN materials on GaN/sapphire substrate by MOVPE using N2 carrier gas. *J. Cryst. Growth* **298,** 316–319 (2007).
152. Ougazzaden, A. *et al.* Bandgap bowing in BGaN thin films. *Appl. Phys. Lett.* **93,** 083118 (2008).
153. Kadys, A. *et al.* Optical and structural properties of BGaN layers grown on different substrates. *J. Phys. D. Appl. Phys.* **48,** 465307 (2015).
154. Cramer, R. C. *et al.* Growth of coherent BGaN films using BBr 3 gas as a boron source in plasma assisted molecular beam epitaxy. *J. Vac. Sci. Technol. A Vacuum, Surfaces, Film.* **35,** 041509 (2017).
155. Gunning, B. P., Moseley, M. W., Koleske, D. D., Allerman, A. A. & Lee, S. R. Phase degradation in B x Ga 1−x N films grown at low temperature by metalorganic vapor phase epitaxy. *J. Cryst. Growth* **464,** 190–196 (2017).
156. Chen, L.-C. & Tien, C.-H. Growth and Characterization of Nanocolumnar-Structure Boron Indium Nitride Alloys Deposited on Sapphire Substrates by Solution Chemical Vapor Deposition. *Jpn. J. Appl. Phys.* **48,** 101001 (2009).
157. Gautier, S. *et al.* Metal-organic vapour phase epitaxy of BInGaN quaternary alloys and characterization of boron content. *J. Cryst. Growth* **312,** 641–644 (2010).
158. Gautier, S. *et al.* Application of dilute boron B(Al,In,Ga)N alloys for UV light sources. in *Proceedings of SPIE - The International Society for Optical Engineering* (eds. Teherani, F. H., Look, D. C. & Rogers, D. J.) **7940,** 79400X (2011).
159. Moses, P. G. & Van de Walle, C. G. Band bowing and band alignment in InGaN alloys. *Appl. Phys. Lett.* **96,** 021908 (2010).
160. Orsal, G. *et al.* Effect of boron incorporation on growth behavior of BGaN/GaN by MOVPE. *J. Cryst. Growth* **310,** 5058–5062 (2008).
161. M. McLaurin. BInGaN LED US Patent. *US Patent 8,106,403 B2* (2012).
162. Park, S.-H. & Ahn, D. Theoretical studies on light emission characteristics of high-efficiency BInGaN/GaN quantum well structures with blue spectral range. *Superlattices Microstruct.* **96,** 150–154 (2016).
163. Assali, A. *et al.* Optoelectronic properties of cubic BxInyGa1−x−yN alloys matched to GaN for designing quantum well Lasers: First-principles study within mBJ exchange potential. *Mater. Sci. Semicond. Process.* **36,** 192–203 (2015).
164. Rinke, P. *et al.* Consistent set of band parameters for the group-III nitrides AlN, GaN, and InN. *Phys. Rev. B* **77,** 075202 (2008).
165. Klimeš, J., Bowler, D. R. & Michaelides, A. Van der Waals density functionals applied to solids. *Phys. Rev. B* **83,** 195131 (2011).
166. Wisesa, P., McGill, K. A. & Mueller, T. Efficient generation of generalized Monkhorst-Pack grids through the use of informatics. *Phys. Rev. B* **93,** 155109 (2016).
167. Said, A., Debbichi, M. & Said, M. Theoretical study of electronic and optical properties of BN, GaN and B x Ga 1−x N in zinc blende and wurtzite structures. *Opt. - Int. J. Light*

Electron Opt. **127,** 9212–9221 (2016).
168. Jiang, J., Gai, Y. & Tang, G. Band gap bowing and crossing of B x Ga 1− x N alloy investigated by hybrid functional method. *J. Semicond.* **37,** 023004 (2016).
169. Bougrov, M., Levinshtein, M. E., Rumyantsev, S. & Zubrilov, A. in *Properties of Advanced Semiconductor Materials: GaN, AIN, InN, BN, SiC, SiGe* (eds. Levinshtein, M. E., Rumyantsev, S. L. & Shur, M. S.) 1–30 (Wiley, 2001).
170. Holec, D., Costa, P. M. F. J., Kappers, M. J. & Humphreys, C. J. Critical thickness calculations for InGaN/GaN. *J. Cryst. Growth* **303,** 314–317 (2007).
171. Williams, L. & Kioupakis, E. BInGaN alloys nearly lattice-matched to GaN for high-power high-efficiency visible LEDs. *Appl. Phys. Lett.* **111,** 211107 (2017).
172. Chai, G. M. T. *et al.* Experimental and modelling study of InGaBiAs/InP alloys with up to 5.8% Bi, and with Δ so > E g. *Semicond. Sci. Technol.* **30,** 094015 (2015).
173. Forghani, K. *et al.* No Title. *Appl. Phys. Lett.* **105,** 111101 (2014).
174. Janotti, A., Wei, S.-H. & Zhang, S. B. No Title. *Phys. Rev. B* **65,** 115203 (2002).
175. Occena, J. *et al.* Bi-enhanced N incorporation in GaAsNBi alloys. *Appl. Phys. Lett.* **110,** 242102 (2017).
176. Denton, A. R. & Ashcroft, N. W. Vegard's law. *Phys. Rev. A* **43,** 3161–3164 (1991).
177. Ramírez-Flores, G., Navarro-Contreras, H., Lastras-Martínez, A., Powell, R. C. & Greene, J. E. Temperature-dependent optical band gap of the metastable zinc-blende structure β-GaN. *Phys. Rev. B* **50,** 8433–8438 (1994).
178. Logothetidis, S., Petalas, J., Cardona, M. & Moustakas, T. D. Optical properties and temperature dependence of the interband transitions of cubic and hexagonal GaN. *Phys. Rev. B* **50,** 18017–18029 (1994).
179. Lymperakis, L. Ab-initio study of boron incorporation and compositional limits at GaN and AlN (0001) surfaces. *AIP Adv.* **8,** 065301 (2018).
180. Shatalov, M., Jain, R., Saxena, T., Dobrinsky, A. & Shur, M. in *Semiconductors and Semimetals* **96,** 45–83 (Elsevier Inc., 2017).
181. Hirayama, H., Maeda, N., Fujikawa, S., Toyoda, S. & Kamata, N. Recent progress and future prospects of AlGaN-based high-efficiency deep-ultraviolet light-emitting diodes. *Jpn. J. Appl. Phys.* **53,** 100209 (2014).
182. Nagasawa, Y. & Hirano, A. A Review of AlGaN-Based Deep-Ultraviolet Light-Emitting Diodes on Sapphire. *Appl. Sci.* **8,** 1264 (2018).
183. Minamata Convention on Mercury. at <http://www.mercuryconvention.org/Convention/Text>
184. Zhang, J., Zhao, H. & Tansu, N. Effect of crystal-field split-off hole and heavy-hole bands crossover on gain characteristics of high Al-content AlGaN quantum well lasers. *Appl. Phys. Lett.* **97,** 111105 (2010).
185. Liu, C. *et al.* 234 nm and 246 nm AlN-Delta-GaN quantum well deep ultraviolet light-emitting diodes. *Appl. Phys. Lett.* **112,** 011101 (2018).
186. Jain, R. *et al.* Migration enhanced lateral epitaxial overgrowth of AlN and AlGaN for high reliability deep ultraviolet light emitting diodes. *Appl. Phys. Lett.* **93,** (2008).
187. Crawford, M. H. in *Semiconductors and Semimetals* **96,** 3–44 (Elsevier Inc., 2017).
188. Park, S.-H. High-efficiency BAlGaN/AlN quantum well structures for optoelectronic applications in ultraviolet spectral region. *Opt. Express* **23,** 3623 (2015).
189. Park, S.-H. & Ahn, D. Effect of boron incorporation on light emission characteristics of UV BAlGaN/AlN quantum well structures. *Appl. Phys. Express* **9,** 021001 (2016).

190. Park, S.-H. & Ahn, D. Lattice-matched double dip-shaped BAlGaN/AlN quantum well structures for ultraviolet light emission devices. *Superlattices Microstruct.* **117,** 413–417 (2018).
191. Park, S.-H. & Ahn, D. Substrate dependence of TM-polarized light emission characteristics of BAlGaN/AlN quantum wells. *Opt. Commun.* **417,** 76–78 (2018).
192. Park, S.-H. & Ahn, D. Theoretical study of optical properties of non-polar BAlGaN/AlN quantum wells lattice-matched to AlN. *Solid State Commun.* **290,** 67–69 (2019).
193. Dreyer, C. E., Lyons, J. L., Janotti, A. & Van de Walle, C. G. Band alignments and polarization properties of BN polymorphs. *Appl. Phys. Express* **7,** 031001 (2014).
194. Dreyer, C. E., Janotti, A., Van de Walle, C. G. & Vanderbilt, D. Correct Implementation of Polarization Constants in Wurtzite Materials and Impact on III-Nitrides. *Phys. Rev. X* **6,** 021038 (2016).
195. Takano, T. *et al.* Room-Temperature Photoluminescence from BAlGaN-Based Double or Single Heterostructures for UV Laser Diode. *Phys. status solidi* **180,** 231–234 (2000).
196. Takano, T. *et al.* Improved Optical Quality of BAlGaN/AlN MQW Structure Grown on 6H-SiC Substrate by Controlling Residual Strain Using Multi-Buffer Layer. *MRS Proc.* **639,** G12.9 (2000).
197. Takano, T., Kurimoto, M., Yamamoto, J. & Kawanishi, H. Epitaxial growth of high quality BAlGaN quaternary lattice matched to AlN on 6H–SiC substrate by LP-MOVPE for deep-UV emission. *J. Cryst. Growth* **237–239,** 972–977 (2002).
198. Li, X. *et al.* 100-nm thick single-phase wurtzite BAlN films with boron contents over 10%. *Phys. status solidi* **254,** 1600699 (2017).
199. Rodnyi, P. A. *Physical Processes in Inorganic Scintillators*. (1997).
200. Lecoq, P., Gektin, A. & Korzhik, M. *Inorganic Scintillators for Detector Systems: Physical Principles and Crystal Engineering*. (2016).
201. Weber, M. J. No Title. *J. Lumin.* **100,** 35 (2002).
202. van Eijk, C. W., Andriessen, J., Dorenbos, P. & Visser, R. No Title. *Nucl. Instrum. Methods Phys. Res., Sect. A* **348,** 546 (1994).
203. Weber, M. J. No Title. *Nucl. Instrum. Methods Phys. Res., Sect. A* **527,** 9 (2004).
204. van Loef, E. V. D., Dorenbos, P., van Eijk, C. W. E., Krämer, K. & Güdel, H.-U. No Title. *Appl. Phys. Lett.* **79,** 1573 (2001).
205. Dorenbos, P. Ce3+ 5d-centroid shift and vacuum referred 4f-electron binding energies of all lanthanide impurities in 150 different compounds. *J. Lumin.* **135,** 93–104 (2013).
206. Dorenbos, P. The 5d level positions of the trivalent lanthanides in inorganic compounds. *J. Lumin.* **91,** 155–176 (2000).
207. Dorenbos, P. Energy of the first 4f7→ 4f65d transition of Eu2+ in inorganic compounds. *J. Lumin.* **104,** 239–260 (2003).
208. Pilania, G., McClellan, K. J., Stanek, C. R. & Uberuaga, B. P. Physics-informed machine learning for inorganic scintillator discovery. *J. Chem. Phys.* **148,** 241729 (2018).
209. Ward, L. *et al.* Matminer: An open source toolkit for materials data mining. *Comput. Mater. Sci.* **152,** 60–69 (2018).
210. Arnold, O. *et al.* Mantid—Data analysis and visualization package for neutron scattering and μ SR experiments. *Nucl. Instruments Methods Phys. Res. Sect. A Accel. Spectrometers, Detect. Assoc. Equip.* **764,** 156–166 (2014).